Ollscoil na hÉireann, Corcaigh

National University of Ireland, Cork

Coláiste na hOllscoile Corcaigh
University College Cork, Ireland

The Nature of Fast Radio Bursts

Thesis presented by

Killian Long

for the degree of Doctor of Philosophy

University College Cork

Department of Physics

Head of Department: Prof. Paul Callanan

Supervisory Team: Prof. Asaf Pe'er
Prof. Paul Callanan
Dr. Michael Tremmel

March 2026

Contents

Abstract

The origin of fast radio bursts (FRBs) is a major open question in the field of astrophysics. We propose that FRBs are produced by synchrotron maser emission (SME) that occurs as a result of non-resonant interactions between Alfvén waves and relativistic plasma. We examine the results of such an interaction, demonstrating that the particles gain significant amounts of kinetic energy through pitch-angle scattering. We show that the interaction forms the necessary population inversions for SME across a wide range of magnetisations and temperatures and examine how the properties of the plasma change as a result of the interaction. We calculate the resulting growth rates and peak frequencies of SME in such a scenario, and show that the mechanism can produce FRBs in the relativistic wind of a magnetar. We determine the lower limits on the wind Lorentz factors ($\gamma_w \gtrsim 310$) necessary to explain observed FRBs. Emission is possible at temperatures of $\theta = k_B T/mc^2 \lesssim 0.02$. We further examine the periods and magnetic fields of the central magnetar and demonstrate that the optimal values of these properties align with the observed magnetar population, provided that the magnetosphere is disturbed by the flaring activity. These results allow the properties of the environment such as temperature and magnetisation to be probed from the observed FRB frequency and luminosity.

Declaration

This is to certify that the work I am submitting is my own and has not been submitted for another degree, either at University College Cork or elsewhere. All external references and sources are clearly acknowledged and identified within the contents. I have read and understood the regulations of University College Cork concerning plagiarism and intellectual property.

Killian Long

Acknowledgements

Firstly, I would like to thank my supervisor Asaf Pe'er for all his guidance and advice over the course of my Masters and PhD. My thanks also go to Paul Callanan and Michael Tremmel for agreeing to act as an additional supervisor and advisor over the last year, and to Denise Gabuzda for her advice early in my PhD. I would also like to thank Danny, Michael, and David Rea for their help as I started out, as well as all the administrative staff in the Physics Department. Thanks as well to everyone at our weekly group meetings for all the interesting discussions.

Thanks to all my friends from physics, especially Russell, Caolan, Dillane, Rory, Dave, and Alex, for all their company throughout this long journey. Those countless trips to the Glucksman to argue about absolutely anything kept me going.

I couldn't have asked for more from my Mum, Dad, and sister Emily, whose love and support have been constant my whole life. My grandparents were also always a great source of encouragement to me. Thanks as well to Tom and all my extended family, who no longer will have to keep asking if I am finally done yet.

Emma, my partner, has been the most amazing cheerleader (and person) anyone could ever ask for and has kept me going with her endless support. I couldn't have done this without you. I would also like to thank Avril, Norman, Julie, and of course Emma's Nana, Papa, and the rest of her family for all their help and encouragement.

Lastly, I would like to thank the Irish Research Council for support through grant number GOIPG/2017/1146, and the European Research Council for funding obtained through ERC Consolidator Grant 773062 (O.M.J.). I also wish to acknowledge the Irish Centre for High-End Computing (ICHEC) for the provision of computational facilities and support.

List of Publications

The following publications arose in whole or in part from the research presented in this thesis:

Chapters 3 & 4

- **Long, K.** & Pe'er, A., "Formation of population inversions in relativistic plasmas through nonresonant interactions with Alfvén waves," *Physical Review D*, 107, L121301, 2023.
- **Long, K.** & Pe'er, A., "A parametric study of population inversions in relativistic plasmas through non-resonant interactions with Alfvén waves and their applications to fast radio bursts," *Monthly Notices of the Royal Astronomical Society*, 538, 1029, 2025.

Chapter 5

- **Long, K.** & Pe'er, A., "Fast Radio Bursts from non-resonant Alfvén waves and synchrotron maser emission in the magnetar wind," *Monthly Notices of the Royal Astronomical Society*, 544, 2160, 2025.

List of Figures

List of Tables

Chapter 1

Introduction

Fast radio bursts (FRBs) are extremely bright radio transients of millisecond duration, whose origin remains one of the major open questions in astrophysics. They exhibit a fascinating variety of properties. While most FRBs have only been detected once, some sources repeat, and only one FRB has been observed at shorter wavelengths. Across the population as a whole, FRBs display a wide range of spectral, temporal, and polarimetric features. These diverse properties have led to a large number of competing models that seek to explain their origin. In this chapter, we review the observational properties of FRBs along with theoretical models of their progenitors and emission mechanisms. We then outline the physics behind one of these models, the synchrotron maser, and describe how the necessary population inversion may be formed through non-resonant interactions with Alfvén waves, which is the primary focus of this thesis.

1.1 Fast radio bursts

The first FRB, known as the 'Lorimer Burst' after its discoverer, was reported in 2007 (Lorimer et al., 2007). Detected by the Parkes radio telescope in Australia, the burst had a maximum flux density of $S_\nu \gtrsim 30$ Jy at a frequency of $\nu \sim 1.4$ GHz, and a duration of ~ 5 ms. Since this first burst, 844[1] additional FRB sources have been found by a variety of radio telescopes to date (e.g. CHIME/FRB Collaboration et al., 2021; Xu et al., 2023)[2].

The first notable characteristic of the Lorimer Burst was its high dispersion measure, DM ~ 375 pc cm^{-3}. The DM of a burst is a measure of the electron column density between the source and observer, and can be directly measured from the characteristic frequency-dependent delay due to the signal propagating through cold plasma. The relationship between the DM and the electron density n_e is defined as

$$\mathrm{DM} = \int_0^D \frac{n_e(l)}{1+z(l)} dl, \tag{1.1}$$

where z is the redshift, l is the comoving distance from the observer, and D is the comoving distance to the source. The large DM of the Lorimer Burst suggested an extragalactic origin, as it far exceeded the expected contribution from Milky Way electrons of $\mathrm{DM}_{MW} \sim 25$ pc cm^{-3} (Cordes & Lazio, 2002; Yao et al., 2017). Subsequent FRBs have exhibited a wide range of dispersion measures extending to values as high as DM ~ 3338 pc cm^{-3} (Crawford et al., 2022), strengthening the argument for their extragalactic nature. The total DM contains contributions from electrons in the source region, the host galaxy, the Milky Way (and its halo), and the intergalactic medium (IGM). Using typical values for all components, except for the IGM contribution, allows the approximate distance to extragalactic FRBs to be calculated through the Macquart relation (e.g. Macquart et al., 2020; Cordes et al., 2022; Zhang, 2023)

$$z \sim \frac{\mathrm{DM}_{IGM}}{855}, \tag{1.2}$$

where DM_{IGM} is the dispersion measure due to electrons in the IGM in units of pc cm^{-3}.

[1] Correct as of 01/09/2025.

[2] FRB databases can be found at the Transient Name Survey (`www.wis-tns.org`) and Blinkverse (`blinkverse.zero2x.org`).

1.1.1 Brightness temperature

The fact that most FRBs are extragalactic implies that they have very high energies for radio transients. Combined with the short timescales of FRBs, this implies extremely high brightness temperatures T_b, where T_b is the temperature of a hypothetical blackbody necessary to produce the FRB signal. This is defined such that (e.g. Rybicki & Lightman, 1979)

$$I_\nu = \frac{2k_B T_b \nu^2}{c^2} \tag{1.3}$$

where I_ν is the specific intensity, ν is the frequency, c is the speed of light in vacuum, and k_B is the Boltzmann constant. The intensity and flux are linked by $S_\nu = I_\nu \Delta\Omega$, where $\Delta\Omega \sim \pi a^2/D^2$ is the solid angle of the source (e.g. Lyubarsky, 2021). Here, a is the source size and D is the distance to the source. Using the duration δt of the burst as an upper bound on the source size therefore results in the relation

$$T_b \sim \frac{S_\nu D^2}{2\pi k_B \delta t^2 \nu^2}\ \mathrm{K}. \tag{1.4}$$

Using typical FRB values of $S_\nu = 1$ Jy $= 10^{-23}$ erg s^{-1} cm^{-2} Hz^{-1}, $\delta t = 1$ ms, $D = 10^{28}$ cm and $\nu = 1$ GHz results in an extremely high brightness temperature of $T_b \sim 10^{36}$ K, up to 10 orders of magnitude higher than the brightest bursts from pulsars (e.g. Katz, 2016a; Zhang, 2023). We note that if the source is moving relativistically towards the observer with a Lorentz factor of Γ, the brightness temperature will be reduced by a factor of Γ (Lyubarsky, 2021). These temperatures are far in excess of those achievable by incoherent radiation mechanisms. For example, incoherent synchrotron radiation is limited to $T_b \lesssim 10^{12}$ K. Above this temperature, inverse Compton scattering causes electrons to lose their energy (e.g. Kellermann & Pauliny-Toth, 1969). Therefore, a coherent emission mechanism where waves are emitted in phase is required to produce FRBs.

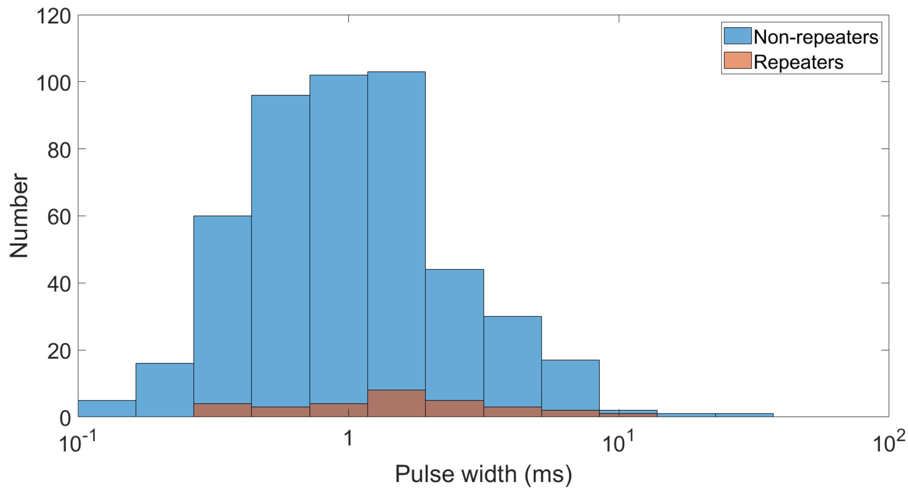

Figure 1.1: Histogram of the pulse widths from the first CHIME/FRB catalog. Bursts from non-repeaters are shown in blue, while bursts from repeaters are shown in orange. The peak of the distribution occurs at just over 1 ms, and the distribution extends for over an order of magnitude to both shorter and longer widths.

1.1.2 Temporal properties

FRBs have typical durations of a few milliseconds (e.g. CHIME/FRB Collaboration et al., 2021). Sub-burst structures as short as ~ 60 ns have been observed from the repeating FRB 20200120E (Nimmo et al., 2022), while on the other end of the temporal scale, FRB 20191221A had a duration of ~ 3 s, though with structure on much shorter timescales (CHIME/FRB Collaboration et al., 2022). A histogram of the burst durations from CHIME/FRB Catalog 1 (containing a total of 536 FRBs) (CHIME/FRB Collaboration et al., 2021) is shown in Fig. 1.1, with the durations of non-repeaters shown in blue and those of repeaters shown in orange[3].

The temporal properties of FRBs are diverse. Although many consist of just one burst (e.g. Lorimer et al., 2007), many show temporal structure on sub-burst scales (Champion et al., 2016; CHIME/FRB Collaboration et al., 2022). Examples include the 'sad trombone' effect, where the frequency of

[3]The pulse widths shown are those given by the `fitburst` algorithm.

the burst decreases with time (Hessels et al., 2019). This frequency drift is in addition to the cold plasma dispersion effect described above in relation to the dispersion measure. The reverse effect, in which later sub-bursts have higher frequencies, has also been observed, although it is much rarer (Zhou et al., 2022). Bursts also show temporal asymmetry, with the rising phase tending to be faster than the decaying phase (e.g. Thornton et al., 2013).

A fraction of the FRB population has been observed to repeat, with 57 repeaters identified out of a total count of 843 FRBs at the time of writing (e.g. CHIME/FRB Collaboration et al., 2021; Xu et al., 2023). Some of these repeaters are very active; for example, thousands of bursts have been detected from the first repeater FRB 20121102A at rates of up to ~ 122 hr^{-1} (Li et al., 2021b). It is possible that all FRBs repeat, and that follow-up bursts from apparent non-repeaters simply have not been detected yet (Kirsten et al., 2024). However, this would require much lower rates of repetition from many FRBs to explain the lack of further detections (Caleb et al., 2019). Some studies show differences in the properties of repeating and non-repeating bursts, with repeaters having longer burst durations and narrower spectra (Pleunis et al., 2021b; Petroff et al., 2022), suggesting that there may indeed be more than one FRB population.

Of the FRBs that do repeat, only a handful show any evidence of periodicity. FRB 20180916B and FRB 20121102A have apparent long-term periods of $\sim$ 16 d (CHIME/FRB Collaboration et al., 2020a) and $\sim$ 160 d (Rajwade et al., 2020) respectively. We note that these periods are not the times between bursts, but rather between windows of heightened activity. FRB 20191221A on the other hand shows apparent periodic activity on much smaller sub-burst timescales of ~ 0.218 s (CHIME/FRB Collaboration et al., 2022).

1.1.3 Spectral properties

FRBs have been detected at frequencies ranging from 110 MHz (Pleunis et al., 2021a; Pastor-Marazuela et al., 2021) to 8 GHz (Gajjar et al., 2018). Increased scattering effects at lower frequencies make detection more challenging (Pleunis et al., 2021a), although the brightness of some bursts suggests that detections at even lower frequencies may be possible (Petroff et al., 2022). At higher frequencies, the time delay introduced by the cold plasma dispersion is reduced, as $\Delta t \propto \nu^{-2}$ (e.g Lorimer et al., 2007). This makes signals harder to distinguish from radio frequency interference (RFI) as they lack the clear dispersion sweep observed at lower frequencies. However, as in the low frequency case, it is likely that detections are still possible (Petroff et al., 2022). The spectra of the bursts are quite diverse, with one-off bursts tending to be more broadband (e.g. filling the full CHIME band of $400 - 800$ MHz for instance), while repeating bursts tend to be narrower (Pleunis et al., 2021b), with some as narrow as ~ 65 MHz (Kumar et al., 2021). The spectral shape of individual FRBs varies, with many broader bursts fitted well by power-law spectra (e.g. Macquart et al., 2019), while narrower bursts from repeaters are fitted better by Gaussians (e.g. CHIME/FRB Collaboration et al., 2019).

1.1.4 Polarisation

FRBs tend to have high degrees of linear polarisation, with typical values of over $\sim 30\%$ (e.g. Zhang, 2023), while degrees of close to 100% are common (e.g. Michilli et al., 2018). Although many bursts show negligible circular polarisation (Nimmo et al., 2021), strong levels have been detected in both non-repeating (Masui et al., 2015) and repeating FRBs (Kumar et al., 2022). The polarisation angles of bursts display varied behaviour, remaining constant in some cases (e.g. Day et al., 2020), while others vary significantly. Such polarisation angle swings can be found in both repeaters (Luo et al., 2020b) and non-repeaters (Cho et al., 2020).

Polarisation measurements also allow the properties of the FRB environment to be probed through Faraday rotation, which is the frequency-dependent change in polarisation angle when a linearly polarised wave passes through a magnetised plasma. The effect is quantified through the Rotation Measure:

$$\mathrm{RM} = \frac{e^3}{2\pi m_e^2 c^4} \int_0^D \frac{B_{\parallel} n_e}{1+z^2} dl = -0.81 \int_0^D \frac{B_{\parallel,-6} n_e}{1+z^2} dl_{pc} \text{ rad m}^{-2}. \quad (1.5)$$

Here e is the electron charge, m_e is the electron mass, $B_{\parallel}$ is the magnetic field strength along the line of sight, l_{pc} is the comoving distance in units of parsecs, and we have used the convention $Q = 10^x Q_x$ in cgs units. Some FRBs have very large RM values of $\sim 10^5$ rad m^{-2} (Michilli et al., 2018), while others have values consistent with 0 (Petroff et al., 2017). Even among those bursts with high RM values, significant variations in behaviour have been observed. Many FRBs show significant RM changes on short timescales (e.g. Xu et al., 2022), including sign reversal (e.g. Anna-Thomas et al., 2023), suggesting a turbulent magnetic environment around the emission region.

1.1.5 Energy, luminosity and rates

The typical energy of an FRB is $E_{iso} \sim 10^{39}$ erg (e.g James et al., 2022), and the distribution of energies spans a wide range from $E_{iso} \sim 10^{34}$ erg (CHIME/FRB Collaboration et al., 2020b; Bochenek et al., 2020) to $E_{iso} \sim 10^{42}$ erg (Ryder et al., 2023). Here, E_{iso} has been calculated assuming that the source emits isotropically. In reality, this is likely not the case, as almost all theoretical models require relativistic emission regions. As such, the true energy required is $\sim E_{iso}/f_b$, where f_b is the beaming factor. The distances to FRBs, needed to calculate E_{iso}, can be estimated using both the Macquart relation and host galaxy observations. Fig. 1.2 shows the relative rate of FRBs, $P(E)$, with isotropic energies of $E > E_{iso}$ for various studies (Luo et al., 2020a; James et al., 2022; Hashimoto et al., 2022; Shin et al., 2023). In most works, these rates are modelled using a Schechter function of the form

$$P(E)dE \propto \frac{1}{E_{max}} \left(\frac{E}{E_{max}}\right)^{\gamma} \exp\left(\frac{-E}{E_{max}}\right) dE, \quad (1.6)$$

except for in James et al. (2022), where a power-law of the form

$$P(E_{min} < E < E_{max}) \propto \frac{\left(\frac{E}{E_{min}}\right)^{\gamma} - \left(\frac{E_{max}}{E_{min}}\right)^{\gamma}}{1 - \left(\frac{E_{max}}{E_{min}}\right)^{\gamma}}, \tag{1.7}$$

is used. In all cases E_{max} is the high energy cut-off value, E_{min} is the minimum FRB energy and γ is the power-law exponent. The studies using the Schechter function only include FRBs with $E_{iso} > 10^{39}$ erg. In general, the rate for bursts with $E_{iso} < 10^{39}$ erg is difficult to constrain due to the lack of low-energy observations. On the other hand, James et al. (2022) use $E_{min} = 10^{30}$ erg, as they note there is no evidence for a minimum FRB energy. The results of the various studies are presented in Fig. 1.2 and the values of E_{max} and γ are shown in Table 1.1. In most cases, the upper energy cut-off is at $E_{iso} \sim 10^{41-42}$ erg, with the rate of FRBs at higher energies dropping sharply. Therefore, any model needs to be able to produce an isotropic equivalent energy of $E_{iso} \lesssim 10^{41-42}$ erg. The FRB energy function is not well constrained at lower energies, but FRBs with energies as low as $E_{iso} \sim 10^{35}$ erg have been detected (CHIME/FRB Collaboration et al., 2020b).

Study	E_{max}	γ	Survey
Shin et al. (2023)	$41.38^{+0.51}_{-0.51}$	$-1.3^{+0.7}_{-0.4}$	CHIME
Hashimoto et al. (2022) (A)	$39.9^{+0.2}_{-0.2}$	$-1.1^{+0.6}_{-0.4}$	CHIME
Hashimoto et al. (2022) (B)	$41.2^{+0.7}_{-0.3}$	-1.4 (fixed)	CHIME
James et al. (2022)	$41.70^{+0.53}_{-0.06}$	$-2.09^{+0.14}_{-0.1}$	ASKAP/Parkes
Luo et al. (2020a)	$41.16^{+0.51}_{-0.19}$	$-1.79^{+0.16}_{-0.18}$	Various

Table 1.1: Summary of the FRB energy functions for various studies. Here E_{max} is the high energy cut-off value and γ is the differential power-law index. The two results from Hashimoto et al. (2022) are due to the separation of their sample into separate redshift bins. Sample A corresponds to non-repeating FRBs with redshifts of $0.05 < z \leq 0.41$, and sample B contains non-repeating FRBs with redshifts of $0.38 < z \leq 3.60$. The values from James et al. (2022) were obtained using Eq. (1.7) while all the others used Eq. (1.6).

The rate of FRBs with energy greater than 10^{39} erg is approximately 8×10^4 Gpc^{-3} yr^{-1} at both 600 MHz (Shin et al., 2023) and 1.4 GHz (James

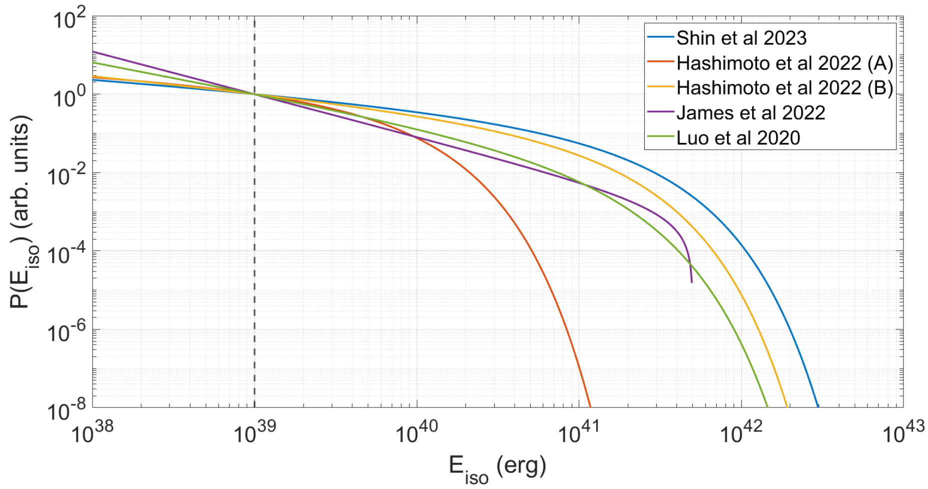

Figure 1.2: The relative rate of FRBs above a given isotropic energy, $P(E)$, based on different studies. The details of each are given in Table 1.1. The values are normalised to have equal $P(10^{39})$, as all of the studies except James et al. (2022) only include FRBs with $E_{iso} > 10^{39}$, shown by the vertical dashed black line.

et al., 2022), though the rate at lower frequencies may be substantially higher as highly scattered FRBs were excluded. As mentioned previously, the rate for bursts with $E_{iso} < 10^{39}$ erg is difficult to constrain due to the lack of observations of lower energy bursts. This rate is higher than typical rates of cataclysmic events. Type Ia and core-collapse supernovae have local rates of $\mathcal{O}(10^4)$ Gpc^{-3} yr^{-1}, while superluminous supernovae have a lower rate of $\mathcal{O}(10^2)$ Gpc^{-3} yr^{-1} (Oguri, 2019; Shin et al., 2023). Both long and short gamma-ray bursts also have lower rates of $\mathcal{O}(\lesssim 10^2)$ Gpc^{-3} yr^{-1} (Oguri, 2019; Shin et al., 2023). The inferred rate of binary compact object mergers (e.g., binary black hole, binary neutron star, and neutron star–black hole) are all lower still at $\mathcal{O}(10^2)$ Gpc^{-3} yr^{-1} (Abbott et al., 2023a). This rate comparison implies that a significant fraction of the FRB population, if not all, must be explained by non-cataclysmic models.

1.1.6 Hosts and counterparts

A growing fraction of FRBs have associated host galaxies, with 117 detected to date (e.g. Xu et al., 2023). The first FRB to be localised was the repeater FRB 20121102A, which lies in a low-metallicity dwarf galaxy (Tendulkar et al., 2017). However, further discoveries showed that this is not a typical FRB host. Indeed, many FRBs have been localised to massive spiral (e.g. Marcote et al., 2020) and elliptical (e.g. Bannister et al., 2019) galaxies. The locations of the FRBs within a galaxy also show significant variation, with bursts found in regions of both high (e.g. Bassa et al., 2017; Fong et al., 2021) and low (e.g. Tendulkar et al., 2021) star formation. The host galaxies of the majority of FRBs are consistent with the hosts of core-collapse supernovae (the formation channel of magnetars) (Bochenek et al., 2021), while the galaxy properties are inconsistent with typical long gamma-ray burst and superluminous supernovae hosts (Mannings et al., 2021). Interestingly, the repeating FRB 20200120E was observed to originate from a globular cluster near M81, an environment which is not expected to host stars such as magnetars (Kirsten et al., 2022).

A small number of FRBs also have counterparts. Three repeaters, FRB 20121102A, FRB 20190520B and FRB 20201124A, all have persistent radio sources (PRS) in close proximity (Tendulkar et al., 2017; Niu et al., 2022; Bruni et al., 2024). These may be associated with pulsar/magnetar wind nebulae or supernova remnants. The only burst to be linked directly to a progenitor is FRB 20200428, which is associated with the Galactic magnetar SGR 1935+2154 (CHIME/FRB Collaboration et al., 2020b; Bochenek et al., 2020; Mereghetti et al., 2020). This FRB occurred at the same time as a hard X-ray burst detected by several observatories (Integral (Mereghetti et al., 2020), Insight-HXMT (Li et al., 2021a), AGILE (Tavani et al., 2021), and Konus-Wind (Ridnaia et al., 2021)). To date, this remains the only multi-wavelength observation of an FRB, with no optical, X-ray, γ-ray or indeed gravitational wave (GW) counterpart detected for any other source (e.g. Scholz et al., 2017; Hiramatsu et al., 2023; Abbott et al., 2023b).

It is clear that the properties of FRBs vary significantly in many ways, and that FRBs may not even all originate from the same population of sources. However, any model that seeks to explain the origin of the bursts must account for some universal properties. These include the typical emission frequency in the GHz band, the extremely high brightness temperatures, the millisecond duration and the high polarisation of the majority of FRBs. For those models which seek to explain repeating FRBs, the progenitor must also not be destroyed in the emission process. In the following section we review some of the most common and promising progenitors and models that have been proposed.

1.2 Fast radio burst models

1.2.1 Progenitors

Since the discovery of the first FRBs, a large number of theoretical models have been proposed to explain them (see Platts et al. (2019)[4] for a catalog of proposed models). The short durations of the bursts imply a source region size of $c\delta t \sim 3 \times 10^7 \delta t_{-3}$ cm. Most models therefore invoke central compact objects, such as neutron stars or black holes, which can provide both the short timescales and large energy reservoirs necessary to power FRBs. The most popular progenitor model places a magnetar as the central object (e.g. Lyubarsky, 2014; Katz, 2016b; Metzger et al., 2017; Beloborodov, 2020; Long & Pe'er, 2025b). Magnetars are highly magnetised neutron stars with surface magnetic fields of $B_* \sim 10^{14-15}$ G which can power FRBs (including repeating bursts) with their large store of magnetic energy. One FRB definitively originates from a magnetar, with FRB 20200428 associated with the Galactic Soft Gamma Repeater SGR 1935+2154 (CHIME/FRB Collaboration et al., 2020b; Bochenek et al., 2020). Other neutron star models that can possibly explain repeated bursts include giant pulses from young pulsars (Cordes &

[4]The catalog can be found at `https://frbtheorycat.org`.

Wasserman, 2016; Connor et al., 2016); interactions with asteroids/comets (e.g. Mottez & Zarka, 2014; Geng & Huang, 2015; Bagchi, 2017); the 'cosmic comb' model where an outflow from another object such as a supernova interacts with an isolated neutron star (Zhang, 2017; Ioka & Zhang, 2020; Wada et al., 2021); interacting neutron stars (Gourgouliatos & Lynden-Bell, 2019; Zhang, 2020b); and white-dwarf neutron star binaries (Gu et al., 2016, 2020).

Cataclysmic neutron star models include the collapse of supramassive neutron stars (known as 'blitzars') (Falcke & Rezzolla, 2014; Zhang, 2014; Most et al., 2018); weakly magnetised neutron stars (Long & Pe'er, 2018), neutron star mergers (e.g. Totani, 2013; Wang et al., 2016; Sridhar et al., 2021); and neutron star-black hole mergers (e.g. Zhang, 2019). These progenitors can only account for non-repeating FRBs, since they are one-off events. While neutron stars are the most commonly discussed progenitors in the literature, many other sources have also been proposed. Most prominent are stellar-mass black holes (Katz, 2017; Li et al., 2018); white dwarf mergers (Kashiyama et al., 2013); black hole mergers (Zhang, 2016; Liu et al., 2016; Deng et al., 2018); as well as more exotic models incorporating quark (Ouyed et al., 2020) and axion (Iwazaki, 2015) stars.

1.2.2 Emission mechanisms

The details of the emission mechanism add another layer of complexity to FRB models. Focusing on the magnetar progenitor model in particular, proposed emission mechanisms can be broadly divided into those in which the FRB is emitted close to the neutron star in the magnetosphere, or those emitted farther out in the wind of the star. Most magnetospheric models invoke emission by 'bunches' of relativistic electrons through curvature radiation (e.g. Kumar et al., 2017; Yang & Zhang, 2018; Lu & Kumar, 2018), inverse Compton scattering (Zhang, 2022) or free electron lasers (Lyutikov, 2021). Other magnetospheric models include emission from reconnecting current sheets (Lyubarsky, 2020) and from non-uniform pair production (Wadiasingh & Timokhin, 2019).

The majority of wind models use a variation of the synchrotron/cyclotron maser to explain FRBs, though the details of the application can vary widely. In many models, the maser emission occurs at relativistic shocks (e.g. Lyubarsky, 2014; Beloborodov, 2017; Sironi et al., 2021). This shock may be located in the relativistic magnetar wind (e.g. Beloborodov, 2017, 2020), in the wind behind previous magnetar flares (e.g. Metzger et al., 2019; Margalit et al., 2020) or at the termination shock (Lyubarsky, 2014). The shock maser model has also been applied to FRB progenitors other than magnetars (e.g. Waxman, 2017; Long & Pe'er, 2018). In this work, we focus on maser emission caused by the non-resonant interactions of Alfvén waves with the relativistic wind of a magnetar, and show that this is a viable mechanism for producing FRBs (Long & Pe'er, 2023, 2025a,b).

1.3 Maser emission

The stimulated emission resulting from the resonance between energetic particles in a plasma and an electromagnetic wave is known as cyclotron or synchrotron maser emission (SME), depending on the energies of the particles involved (e.g. Twiss, 1958; Melrose, 2017). For simplicity, we will use the term SME throughout this work. Variations of this mechanism have been used to explain a range of astrophysical phenomena in both the solar system and further afield. These include auroral kilometric radiation (AKR) from the Earth's aurora (e.g. Wu & Lee, 1979; Wu, 1985); decametric radiation (DAM) from Jupiter (e.g. Hirshfield, 1963; Melrose, 1976); stellar emission (e.g. Fleishman & Mel'nikov, 1998); emission from blazar jets (Begelman et al., 2005); and FRBs (e.g. Lyubarsky, 2014; Metzger et al., 2019; Long & Pe'er, 2023).

Maser emission requires a population inversion, where there is an excess of particles at high energies. We note that this is different from the population inversion discussed in, for example, laser physics. In those cases, the population inversion is formed by the excitation of atoms (or molecules) to higher energy levels. In contrast, in the context of SME, the population inversion consists of an excess population of particles (typically electrons) in a plasma at high energies. The formation of such populations is discussed in more detail in Sec. 1.3.2 below. In this thesis, we consider an initially thermal distribution of electrons in the wind of a magnetar. The needed population inversion is formed when these electrons interact non-resonantly with Alfvén waves that originate from the magnetar due to a starquake (e.g Blaes et al., 1989; Thompson & Duncan, 1996). The waves impart energy to the electrons, and the resulting distribution may result in SME. In Sec. 1.3.1 we review the background physics behind SME, in Sec. 1.3.2 we describe the different physical scenarios in which it may occur, and in Sec. 1.3.3 we discuss the mechanism of non-resonant interactions with Alfvén waves.

1.3.1 Background physics

In this section we briefly introduce the basic physics behind maser emission. Resonant absorption or stimulated emission occurs when the resonance condition

$$\gamma\omega - l\Omega - k_{\|}p_{\|} = 0, \tag{1.8}$$

is satisfied (e.g. Wu, 1985). Here, ω is the angular frequency of the wave, k is the wavenumber, l is the harmonic number and $p = \gamma m v$ is the relativistic momentum. The particle velocity is denoted by v, the particle mass by m and $\gamma = \left(1 - |\mathbf{v}|^2/c^2\right)^{-1/2}$ is the particle Lorentz factor. The cyclotron frequency is given by $\Omega = \frac{qB}{mc}$, where q is the particle charge and $\mathbf{B}$ is the magnetic field. The subscripts $\|$ and $\perp$ refer to directions parallel and perpendicular to the background magnetic field $\mathbf{B}$. Electrons gyrating slightly slower than the wave frequency gain energy from the wave, while faster electrons lose energy. The process results in the particles all obtaining the same phase angle due to this 'gyrophase bunching', and the 'bunch' of electrons can thus result in stimulated coherent emission (e.g. Treumann, 2006).

Resonance alone is not a sufficient condition for SME. For most particle distributions, such as thermal distributions or even bi-Maxwellians, wave modes will experience resonant damping rather than growth if Eq. (1.8) is fulfilled. In order for growth to occur, the imaginary part of the wave frequency, ω_i, must be positive. This requires the presence of a population inversion, where there is an excess of particles at higher energies or momenta for at least part of the distribution function $F(p_\parallel, p_\perp)$. In the simplest case of perpendicular wave propagation,

$$\omega_i \propto \frac{\partial F}{\partial p_\perp}. \tag{1.9}$$

Therefore, the requirement for wave growth is $\frac{\partial F}{\partial p_\perp} > 0$ (Melrose, 2017). The full expression for the absorption coefficient is discussed in much greater detail in Sec. 2.3, where the other terms are given for arbitrary propagation direction. The definition of the population inversion is also often given in terms of the particle energy E, in which case the requirement is that $\frac{\partial F}{\partial E}$ grows faster than E^2 (e.g. Rybicki & Lightman, 1979). We discuss different population inversions in Sec. 1.3.2 below. For efficient SME, the resonance ellipse defined by Eq. (1.8) for growing modes must primarily overlap with the region of momentum space where the population inversion is present to avoid damping from other particles. The amplification of the signal is exponential, with the power P gained over a distance d given by

$$P \propto e^{-i\omega_i d/c}. \tag{1.10}$$

The frequency of the fastest growing mode is usually close to $\omega_r \sim l\Omega/\gamma$, where $\omega = \omega_r + i\omega_i$. For this reason, a highly magnetised plasma is generally preferred, as otherwise the emission frequency at the primary harmonic will be lower than the plasma frequency, $\omega_p = \sqrt{\frac{4\pi n q^2}{m}}$ (e.g. Wu, 1985). Here, n is the number density. In a cold plasma, the highly magnetised condition is satisfied for magnetisations of $\bar{\sigma} > 1$, where

$$\bar{\sigma} = \frac{\Omega^2}{\omega_p^2} = \frac{B^2}{4\pi n m c^2}. \tag{1.11}$$

While in the context of FRBs a highly magnetised environment is more likely in the case of a magnetar central engine (e.g. Beloborodov, 2020), emission is still possible in the weakly magnetised case at higher harmonics where the Razin effect (also known as the Razin-Tsytovich effect) is important (Sagiv & Waxman, 2002). This effect occurs when the refractive index N_r differs from its vacuum value due to the impact of the plasma on the electromagnetic wave. This results in a change of the beaming angle of the emission from the accelerating charge, strongly altering the properties of the emission (Rybicki & Lightman, 1979). This can be seen by examining the beaming angle for a relativistic particle θ_b (Sagiv & Waxman, 2002):

$$\theta_b \approx \begin{cases} \left(\frac{1}{\gamma^2}\left(\frac{\omega_c}{\omega}\right) + 1 - N_r^2\right)^{1/2}, & \omega \gg \omega_c \\ \left(\frac{1}{\gamma^2} + 1 - N_r^2\right)^{1/2}, & \omega \sim \omega_c \\ \left(\frac{1}{\gamma^2}\left(\frac{\omega_c}{\omega}\right)^{2/3} + 1 - N_r^2\right)^{1/2}, & \omega \ll \omega_c \end{cases} \tag{1.12}$$

where $\omega_c = \gamma^3 \omega_p$ is the characteristic synchrotron frequency. When $N_r \sim 1$, these reduce to their vacuum equivalents. However, when $N_r = 1 - \frac{\omega_p^2}{\omega^2} < 1$, as in a cold relativistic plasma, the plasma effects become important. The approximate value at which this occurs can be estimated by comparing the magnitude of $\frac{\omega_p^2}{\omega^2}$ to the other terms in the beaming angle expressions given in Eq. (1.12). The resulting frequency is called the Razin frequency, and is given by (Sagiv & Waxman, 2002)

$$\omega_R^* = \omega_p \min\left\{\gamma, \sigma^{-1/4}\right\}. \tag{1.13}$$

This frequency thus provides an approximate value for the peak emission frequency due to SME in the weakly magnetised regime (e.g. Sagiv & Waxman, 2002; Waxman, 2017).

1.3.2 Population inversion

The problem of how to obtain the necessary population inversion to support SME is a crucial one. In this section, we briefly review some of the models for the formation of population inversions in astrophysical plasmas, before describing in greater detail the specific mechanism that is the focus of this work, namely non-resonant interactions with Alfvén waves, in Sec. 1.3.3.

Initial work on AKR and DAM suggested that a loss-cone distribution could provide the necessary population inversion to power SME (e.g. Wu & Lee, 1979; Hewitt et al., 1982). A loss-cone forms when particles travel into regions of enhanced magnetic field. These particles have a pitch-angle defined by

$$\alpha = \tan^{-1}\left(\frac{p_\perp}{p_\parallel}\right). \tag{1.14}$$

Particles with large pitch-angles are reflected by the strong magnetic field, while those with small pitch-angles may escape. In the case of AKR for example, these particles enter the atmosphere, leaving a gap in the distribution at low pitch-angles (Wu & Lee, 1979). Defining the minimum pitch-angle at which particles are reflected as α_{lc}, the loss-cone distribution can be approximated as (Wu, 1985)

$$F_{lc}(p,\alpha) = \begin{cases} A\exp\left(\frac{-p^2}{\xi^2}\right) & \alpha > \alpha_{lc} \\ 0 & \alpha < \alpha_{lc} \end{cases}, \tag{1.15}$$

where A is the normalisation constant, and ξ characterises the thermal spread of the particles. This distribution contains the required $\frac{\partial F}{\partial p_\perp} > 0$ at the transition from the empty region of the distribution $\alpha \sim \alpha_{lc}$, as can be seen in Fig. 1.3a.

Although the loss-cone is still considered a possible driver of Jovian DAM (Melrose, 2017), later work, including measurements from satellites, indicated the presence of a ring or shell distribution (Pritchett & Strangeway, 1985; Winglee & Dulk, 1986). A thermal ring distribution takes the form

$$F_r(p_\parallel, p_\perp) = A \exp\left(-\frac{p_\parallel^2}{\xi_\parallel^2} - \frac{(p_\perp - p_0)^2}{\xi_\perp^2}\right), \tag{1.16}$$

where p_0 is the characteristic momentum of the distribution. The name 'ring distribution' refers to the fact that, in the $p_x - p_y$ plane, the distribution forms a ring. An example of such a distribution is shown in Fig. 1.3b in the $v_\parallel - v_\perp$ plane. The shell distribution is an extension of the ring to three dimensions:

$$F_{rs}(p_\parallel, p_\perp) = A \exp\left(-\frac{\left(\sqrt{p_\parallel^2 + p_\perp^2} - p_0\right)^2}{\xi^2}\right). \tag{1.17}$$

An example of this type of distribution is shown in Fig. 1.3c. Such distributions may form in this context through the presence of electric fields associated with an Alfvénic Poynting flux originating from magnetic reconnection in the Earth's magnetotail (Melrose, 2017). This energy is used to accelerate the electrons to higher momenta.

The combination of the ring/shell and loss-cone is known as a horseshoe distribution, and is thought to be the true source of the population inversion in AKR (e.g. Bingham & Cairns, 2000; Ergun et al., 2000; Treumann, 2006). This distribution is similar to a more extreme version of the crescent-shaped distribution generated by non-resonant interactions with Alfvén waves which will be discussed extensively through this work. A sample horseshoe distribution is shown in Fig. 1.3d using the following distribution function,

$$F_h(p_\parallel, p_\perp) = A \exp\left(-\frac{\left(\sqrt{p_\parallel^2 + p_\perp^2} - p_0\right)^2}{\xi^2}\right) L(p_\parallel), \tag{1.18}$$

where

$$L(p_\parallel) = \begin{cases} 1 - \frac{p_\parallel^2}{p^2} & p_\parallel > 0 \\ 1 & p_\parallel \leq 0 \end{cases}. \tag{1.19}$$

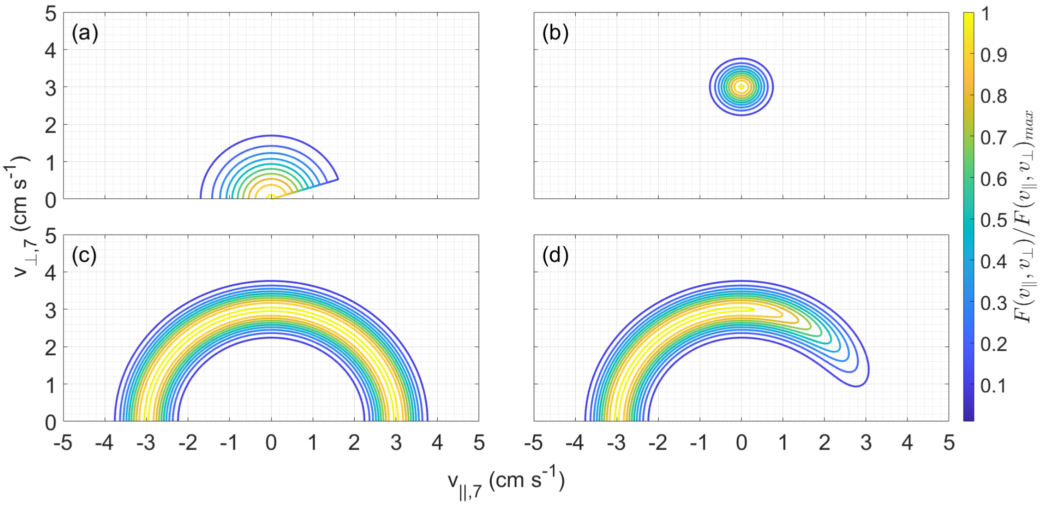

Figure 1.3: Contour plots of various distributions containing population inversions. **Panel (a)** shows a loss-cone distribution (Eq. (1.15)) with $\xi = 2.5 \times 10^7$cm s^{-1} and $\alpha_{lc} = \pi/10$. **Panel (b)** displays a ring distribution (Eq. (1.16)) with $\xi_\| = \xi_\perp = 5 \times 10^6$cm s^{-1} and $v_0 = p_0/m = 3 \times 10^7$cm s^{-1}. A ring-shell distribution (Eq. (1.17)) is shown in **panel (c)** with $\xi = 5 \times 10^6$cm s^{-1} and $v_0 = p_0/m = 3\times10^7$cm s^{-1}. Finally, **panel (d)** shows a horseshoe distribution (Eq. (1.18)), where again $\xi = 5 \times 10^6$cm s^{-1} and $v_0 = p_0/m = 3 \times 10^7$cm s^{-1}. The distributions have been plotted as functions of velocity rather than momentum as the parameters used are non-relativistic. Each distribution has a region where $\frac{\partial F}{\partial v_\perp} > 0$, providing the necessary population inversion for SME.

In the context of FRBs, the ring distribution is also commonly invoked to explain SME. However, the formation channel of the distribution in this case is quite different. In these models, the ring distribution is formed in relativistic magnetised shocks. The enhanced magnetic field at the shock front produces a soliton-like structure in which particles are reflected (e.g. Alsop & Arons, 1988; Gallant et al., 1992; Amato & Arons, 2006; Plotnikov & Sironi, 2019). Particle-in-cell (PIC) simulations in electron-positron plasmas (e.g. Sironi et al., 2021) and those also containing ions (e.g. Sironi & Spitkovsky, 2011) have shown strong evidence for the presence of SME in this model. It has also been proposed that similar distributions may form through radiation reaction cooling (Bilbao & Silva, 2023; Bilbao et al., 2024, 2025).

1.3.3 Non-resonant interactions with Alfvén waves

In this work, we focus on the formation of population inversions through non-resonant interactions between Alfvén waves and plasma. The potential importance of such interactions was first noted in the 2000s in the context of stellar coronae. Many stars, including the Sun, possess hot stellar coronae. The plasma in the corona has a low plasma β value, where

$$\beta = \frac{8\pi n k_B T}{B^2}, \tag{1.20}$$

is the ratio of the thermal pressure to the magnetic pressure. In such plasmas, conventional plasma heating of protons through cyclotron resonance is not possible, as the typical velocities and wave frequencies are too low compared to Ω. This process was initially investigated through test-particle simulations (Wang et al., 2006) and quasilinear theory (Wu & Yoon, 2007). Wu & Yoon (2007) showed that for weak turbulence, the non-resonant interaction results in an increase in the apparent perpendicular temperature by a factor of $1+4\epsilon$, where ϵ is a measure of the turbulence level defined as

$$\epsilon = \frac{1}{4n_p T_0} \int dk \frac{B_k^2}{8\pi}. \tag{1.21}$$

Here, T_0 is the initial temperature, n_p is the proton density and B_k is the spectral wave magnetic field. In contrast, the parallel temperature is only weakly affected.

The quasilinear analysis was later extended to moderate turbulence levels by Yoon et al. (2009). This work identified that the apparent perpendicular heating was actually pitch-angle diffusion that depends on the turbulence level, agreeing with test particle simulations. For very low turbulence levels this manifested as perpendicular heating, but for higher turbulence levels parallel effects also become significant (e.g. Yoon et al., 2009; Nariyuki et al., 2010). It is important to note that the heating that occurs is not permanent. In the absence of the Alfvén waves, the enhanced perpendicular temperature decays (e.g. Wang & Wu, 2009; Wu et al., 2014a). For this reason the mechanism is sometimes referred to as 'pseudoheating' rather than true heating.

Various authors noted that the same mechanism can be applied to electrons, and that the crescent-shaped particle distribution that resulted from the non-resonant interaction contained a population inversion (e.g. Wu et al., 2012; Zhao & Wu, 2013; Wu, 2014). This population inversion was shown to be sufficient to produce maser emission across a range of parameters (e.g. Tong et al., 2017). In general, these studies approximate the crescent-shaped distribution through an analytical model distribution, rather than directly calculating the distribution for the parameters in question.

To extend the idea of non-resonant interactions with Alfvén waves to the environment around FRBs, a fully relativistic treatment is required. This is because the temperatures involved may be relativistic (e.g. Babul & Sironi, 2020; Beloborodov, 2020), with

$$\theta = \frac{k_B T}{m_e c^2} \sim 1. \tag{1.22}$$

Furthermore, plasmas around the possible FRB progenitors, such as magnetars, are so highly magnetised that the Alfvén velocity is relativistic and approaches the speed of light. To fully explore the viability of the model, we therefore investigate the fully relativistic quasilinear kinetic equation. We detail the derivation and properties of this equation in Sec. 2.2 below.

1.4 Thesis outline

This thesis is structured as follows:

- Chapter 2 details the established theory behind quasilinear kinetic theory and maser emission.
- Chapter 3 discusses the non-resonant interaction between Alfvén waves and a relativistic plasma, and analyses the evolution of the particle distribution.
- Chapter 4 describes how such interactions may form a crescent-shaped particle distribution which can support SME and explores the parameter space where this can occur. Chapters 3 and 4 are based on work published in Long & Pe'er (2023) and Long & Pe'er (2025a).
- Chapter 5 applies the results from the previous chapters, calculating the SME growth rates and applying the results to a specific FRB model where SME produces the signal in the relativistic magnetar wind. This chapter is based on material in Long & Pe'er (2025b).
- Chapter 6 contains the summary and discusses the future outlook.
- Finally, Appendix A contains additional material comparing the full relativistic results in Chapter 3 to analytical approximations, Appendix B contains a detailed examination of specific terms discussed in Chapter 4, and Appendix C deals with the specifics of resonance ellipses, and is of relevance to Chapter 5.

These chapters can be linked to the overall framework of the model, which consists of four stages, as follows:

1. A starquake occurs, generating Alfvén waves that are emitted from the surface of a magnetar. This stage is addressed in Chapter 5.
2. These waves propagate into the magnetar wind. This process is also addressed in Chapter 5.
3. In the wind, non-resonant interactions occur between the Alfvén waves and the wind plasma, resulting in a crescent-shaped population inversion. This area is the main focus of the thesis, and is examined in Chapters 3 & 4.
4. This population inversion is capable of supporting SME, which amplifies electromagnetic (EM) waves to produce the FRB signal. The details of this process are the main focus of Chapter 5.

Chapter 2

Theory

In this chapter, we review the derivations of and physics behind two equations which underpin much of the work in this thesis. In Sec. 2.1, we discuss the quasilinear kinetic equation for the interaction between Alfvén waves and a non-relativistic plasma, while in Sec. 2.2 we review the derivation of the quasilinear equation in the relativistic case. The resulting equation is used throughout the thesis. Sec. 2.3 addresses a related but separate topic, namely the dispersion relation for electromagnetic waves in a relativistic plasma, from which the maser growth rates are calculated in Chapter 5.

2.1 Review of the non-relativistic quasilinear equation

The first examination of the non-resonant interaction using quasilinear theory was carried out by Wu & Yoon (2007), who used the following quasilinear kinetic equation:

$$\begin{aligned}\frac{\partial F}{\partial t} =&\frac{e^2}{2m_p^2}\int dk E_k^2\left[\left(1-\frac{k_\parallel v_\parallel}{\omega}\right)\frac{1}{v_\perp}\frac{\partial}{\partial v_\perp}v_\perp+\frac{k_\parallel v_\perp}{\omega}\frac{\partial}{\partial v_\parallel}\right]\\ &\times\frac{\gamma}{\left(\omega\pm\Omega_p-k_\parallel v_\parallel\right)^2+\gamma^2}\\ &\times\left[\left(1-\frac{k_\parallel v_\parallel}{\omega}\right)\frac{1}{v_\perp}\frac{\partial}{\partial v_\perp}+\frac{k_\parallel v_\perp}{\omega}\frac{\partial}{\partial v_\parallel}\right]F.\end{aligned}\tag{2.1}$$

Here m_p is the proton mass, E_k is the spectral electric field, Ω_p is the proton cyclotron frequency and γ is the temporal growth rate of the Alfvénic turbulence. For shear Alfvén waves, $\mathbf{k}=k_\parallel\hat{\mathbf{z}}$ and the parallel electric field $E_{kz}=0$. As mentioned above, Wu & Yoon (2007) noted that for Alfvén waves in a magnetised plasma, the conditions $\Omega_p\gg\omega$, $\Omega_p\gg k_\parallel v_\parallel$ and $\Omega_p\gg\gamma$ all hold, implying that resonance interactions are not important in such a scenario. This allows the simplification

$$\frac{\gamma}{\left(\omega\pm\Omega_p-k_\parallel v_\parallel\right)^2+\gamma^2}\approx\frac{\gamma}{\Omega_p^2}.\tag{2.2}$$

This allows Eq. (2.1) to be written as

$$\begin{aligned}\frac{\partial F}{\partial t} =&\frac{1}{2n_p m_p}\int dk\left(\frac{\partial}{\partial t}\frac{B_k^2}{8\pi}\right)\left[\left(1-\frac{k_\parallel v_\parallel}{\omega}\right)\frac{1}{v_\perp}\frac{\partial}{\partial v_\perp}v_\perp+\frac{k_\parallel v_\perp}{\omega}\frac{\partial}{\partial v_\parallel}\right]\\ &\times\left[\left(1-\frac{k_\parallel v_\parallel}{\omega}\right)\frac{1}{v_\perp}\frac{\partial}{\partial v_\perp}+\frac{k_\parallel v_\perp}{\omega}\frac{\partial}{\partial v_\parallel}\right]F,\end{aligned}\tag{2.3}$$

where B_k is the spectral magnetic field. Here, it has been assumed that $B_k\sim e^{-i(\omega+i\gamma)t}$ and therefore

$$2\gamma B_k^2=\frac{\partial B_k^2}{\partial t}.\tag{2.4}$$

Furthermore, the relation $B_k^2=\left(\frac{c}{v_A}\right)^2E_k^2$ has been used, where

$$\frac{v_A}{c} = \frac{B}{\sqrt{4\pi n m_p}} \tag{2.5}$$

is the non-relativistic Alfvén velocity. As Wu & Yoon (2007) were interested in low-β plasmas, the terms proportional to $k_{\parallel}v/\omega$ are much smaller than unity, resulting in a kinetic equation which only depends on perpendicular terms:

$$\frac{\partial F}{\partial t} = \frac{1}{2n_p m_p}\int dk \left(\frac{\partial}{\partial t}\frac{B_k^2}{8\pi}\right)\frac{1}{v_\perp}\frac{\partial}{\partial v_\perp}\left(v_\perp \frac{\partial F}{\partial v_\perp}\right). \tag{2.6}$$

After the series of simplifications described above, it is possible to solve Eq. (2.6) analytically for an initial Maxwellian distribution

$$F(\bar{v}_\parallel, \bar{v}_\perp, \epsilon = 0) = \frac{1}{\pi^{3/2}} e^{-\bar{v}_\parallel^2 - \bar{v}_\perp^2}, \tag{2.7}$$

where $\bar{v} = v(2k_B T_0/m_p)^{-1/2}$ is the velocity normalised to the thermal velocity, T_0 is the initial temperature, and ϵ is a measure of the turbulence level defined as

$$\epsilon = \frac{1}{4n_p k_B T_0}\int dk \frac{B_k^2}{8\pi}. \tag{2.8}$$

As shown in Wu & Yoon (2007), the solution is given by

$$F(\bar{v}_\parallel, \bar{v}_\perp, \epsilon) = \frac{1}{\pi^{3/2}} e^{-\bar{v}_\parallel^2 - \frac{\bar{v}_\perp^2}{1+4\epsilon}}. \tag{2.9}$$

This result supported previous test-particle simulations which showed that this non-resonant interaction primarily acted to increase the apparent perpendicular temperature of the particle distribution.

The analysis was later extended to moderate turbulence levels by Yoon et al. (2009). In this case, a slightly different initial quasilinear kinetic equation was used,

$$
\begin{aligned}
\frac{\partial F}{\partial t} =& \frac{e^2}{4m_p^2}\sum_{l=\pm 1}\int dk\frac{1}{v_\perp}\left[\left(1-\frac{k_\parallel v_\parallel}{\omega}\right)\frac{1}{v_\perp}\frac{\partial}{\partial v_\perp}+\frac{k_\parallel v_\perp}{\omega}\frac{\partial}{\partial v_\parallel}\right] \\
&\times\left\{v_\perp\left[\pi\delta(\omega-l\Omega_p-k_\parallel v_\parallel)|E_k|^2-\frac{\partial}{2\partial\omega}\left(PV\frac{1}{\omega-l\Omega_p-k_\parallel v_\parallel}\right)\frac{\partial|E_k|^2}{\partial t}\right]\right. \\
&\times\left.\left[\left(1-\frac{k_\parallel v_\parallel}{\omega}\right)\frac{1}{v_\perp}\frac{\partial}{\partial v_\perp}+\frac{k_\parallel v_\perp}{\omega}\frac{\partial}{\partial v_\parallel}\right]F\right\}. \qquad (2.10)
\end{aligned}
$$

Here PV denotes the principal value. While this equation reduces to Eq. (2.3) in the non-resonant case, it allows for the possibility that the Alfvén waves are generated externally. Yoon et al. (2009) noted that in the wave frame, Eq. (2.10) takes the form of a pitch-angle diffusion equation,

$$
\frac{\partial F(v,\mu,\epsilon_B)}{\partial \epsilon_B}=\frac{\partial}{\partial\mu}\left((1-\mu^2)\frac{\partial F_s(v,\mu,\epsilon_B)}{\partial\mu}\right) \qquad (2.11)
$$

where $\mu = \cos\alpha$ in the wave frame, and ϵ_B is a measure of the turbulence, though unlike in Wu & Yoon (2007) it is defined relative to the background magnetic field such that $\epsilon_B = \int d\mathbf{k}\frac{B_k^2}{4B_0^2}$. Since our interest extends beyond the non-relativistic regime, it is necessary to extend these equations to the fully relativistic quasilinear case, which we discuss in the following section.

2.2 Relativistic quasilinear equation

In this section we derive the relativistic quasilinear kinetic equation following the derivation in Chapters 10, 16, and 17 of Stix (1992). The analysis begins from the relativistic Vlasov equation,

$$
\frac{\partial f_s}{\partial t}+\mathbf{v}\cdot\frac{\partial f_s}{\partial \mathbf{r}}+q_s\left(\mathbf{E}+\frac{\mathbf{v}\times\mathbf{B}}{c}\cdot\frac{\partial f_s}{\partial \mathbf{p}}\right)=0, \qquad (2.12)
$$

where s denotes the species. In quasilinear analysis, the distribution function is split into components such that f_0 is the distribution averaged over several wave periods in time and space, while f_1 is the rapidly varying part of the distribution function. The slow time evolution $\frac{\partial f_0}{\partial t}$ is calculated by averaging over the contributions from the products of the rapidly fluctuating distribution f_1 and electromagnetic field terms $\mathbf{E_1}$ and $\mathbf{B_1}$, such that

$$\begin{aligned}\frac{\partial f_0(p_\parallel, p_\perp, t)}{\partial t} &= -\,q\left\langle \int_0^{2\pi} \frac{d\phi}{2\pi} \nabla_{\mathbf{p}} \cdot \left[\left(\mathbf{E_1} + \frac{\mathbf{v}\times\mathbf{B_1}}{c}\right) f_1\right]\right\rangle \\ &= -\,q \lim_{V\to\infty} \int \frac{d^3\mathbf{k}}{V} \int_0^{2\pi} \frac{d\phi}{2\pi} \nabla_{\mathbf{p}} \cdot \left[\left(\mathbf{E_k} + \frac{\mathbf{v}\times\mathbf{B_k}}{c}\right) f_{-k}\right].\end{aligned} \tag{2.13}$$

Here, we have assumed that the distribution function can be averaged over the gyro-angle ϕ, and the subscript k denotes a Fourier transform. Furthermore, throughout this section we omit the species subscript for clarity. In order to evaluate the integral in Eq. (2.13), it is necessary to both expand the divergence term $\nabla_{\mathbf{p}} \cdot \left[\left(\mathbf{E_k} + \frac{\mathbf{v}\times\mathbf{B_k}}{c}\right) f_{-k}\right]$, as well as calculate the fluctuation f_k. As a first step, $\mathbf{B}_k$ can be replaced using Maxwell's induction equation $\left(\mathbf{B} = \frac{\mathbf{k}c}{\omega} \times \mathbf{E}\right)$ so that

$$\mathbf{E}_k + \frac{\mathbf{v}\times\mathbf{B}_k}{c} = \left[\mathbf{1}\left(1 - \frac{\mathbf{v}\cdot\mathbf{k}}{\omega}\right) + \frac{\mathbf{v}\mathbf{k}}{\omega}\right] \cdot \mathbf{E}_k, \tag{2.14}$$

where $\mathbf{1}$ is the unit dyadic. It is also useful to express some of the vector quantities in terms of their components,

$$
\begin{aligned}
\mathbf{B_0} =& B_0\hat{\mathbf{z}}, \\
\mathbf{v} =& v_\perp \cos\phi \hat{\mathbf{x}} + v_\perp \sin\phi \hat{\mathbf{y}} + v_\parallel \hat{\mathbf{z}} = v_\perp \hat{\boldsymbol{\rho}} + v_\parallel \hat{\mathbf{z}}, \\
\nabla_{\mathbf{p}} =& \hat{\boldsymbol{\rho}} \frac{\partial}{\partial p_\perp} + \hat{\boldsymbol{\phi}} \frac{1}{p_\perp} \frac{\partial}{\partial p_\perp} + \hat{\mathbf{z}} \frac{\partial}{\partial p_\parallel}, \\
\mathbf{k} =& k_\perp \cos\theta \hat{\mathbf{x}} + k_\perp \sin\theta \hat{\mathbf{y}} + k_\parallel \hat{\mathbf{z}} \\
=& k_\perp \cos(\phi - \theta) \hat{\boldsymbol{\rho}} + k_\perp \sin(\phi - \theta) \hat{\boldsymbol{\phi}} + k_\parallel \hat{\mathbf{z}}, \\
\mathbf{E} =& E_x \hat{\mathbf{x}} + E_y \hat{\mathbf{y}} + E_z \hat{\mathbf{z}} \\
&= (E_x \cos\phi + E_y \sin\phi) \hat{\boldsymbol{\rho}} + (-E_x \sin\phi + E_y \cos\phi) \hat{\boldsymbol{\phi}} + E_z \hat{\mathbf{z}}.
\end{aligned}
\tag{2.15}
$$

Here, $\hat{\boldsymbol{\rho}}$ is the unit vector in the perpendicular direction and $\hat{\boldsymbol{\phi}} = \hat{\mathbf{z}} \times \hat{\boldsymbol{\rho}}$. We also make the further useful definition

$$
E^{\pm} = \frac{1}{2} \left(E_x \pm i E_y \right) e^{\mp i\theta}. \tag{2.16}
$$

With these considerations we can expand the term in Eq. (2.13) to get

$$
\begin{aligned}
\nabla_{\mathbf{p}} \cdot \left[\left(\mathbf{E_k} + \frac{\mathbf{v} \times \mathbf{B_k}}{c} \right) f_{-k} \right] = \cos(\phi - \theta) \left[(E_k^+ + E_k^-) S f_{-k} - E_{kz} R f_{-k} \right] \\
- i \sin(\phi - \theta)(E_k^+ - E_k^-) S f_{-k} + E_{kz} \frac{\partial f_{-k}}{\partial p_\parallel} + C_\phi.
\end{aligned}
\tag{2.17}
$$

Here C_ϕ contains all the $\frac{\partial}{\partial \phi}$ terms which will not need to be calculated as they do not contribute to the final result, while S and R denote the differential operators

$$
\begin{aligned}
Sf_{-k} &= \left(1 - \frac{k_\parallel v_\parallel}{\omega}\right)\frac{1}{p_\perp}\frac{\partial}{\partial p_\perp}(p_\perp f_{-k}) + \frac{k_\parallel v_\perp}{\omega}\frac{\partial f_{-k}}{\partial p_\parallel}, \\
Rf_{-k} &= \frac{k_\parallel v_\perp}{\omega}\frac{\partial f_{-k}}{\partial p_\parallel} - \frac{k_\perp v_\parallel}{\omega}\frac{1}{p_\perp}\frac{\partial}{\partial p_\perp}(p_\perp f_{-k}).
\end{aligned}
\tag{2.18}
$$

The next step is to determine f_k by solving the first-order Vlasov equation:

$$
\left(\frac{df_1}{dt}\right)_0 = -q_s\left(\mathbf{E_1} + \frac{\mathbf{v}}{c} \times \mathbf{B_1}\right) \cdot \frac{\partial f_0}{\partial \mathbf{p}}, \tag{2.19}
$$

where $\left(\frac{df_1}{dt}\right)_0$ is the rate of change along the zero-order trajectory $\mathbf{r}'(t')$. The solution is found by integrating over time:

$$
f_1(\mathbf{r}, \mathbf{v}, t) = -q\int_{-\infty}^{t} dt' \left(\mathbf{E_1}(\mathbf{r}', t') + \frac{\mathbf{v}'}{c} \times \mathbf{B_1}(\mathbf{r}', t')\right) \cdot \frac{\partial f_0(\mathbf{p}')}{\partial \mathbf{p}'}. \tag{2.20}
$$

Using Eq. (2.14) yields

$$
f_1(\mathbf{r}, \mathbf{v}, t) = -q\int_{-\infty}^{t} dt' e^{i\mathbf{k}\cdot\mathbf{r}' - i\omega t'}\mathbf{E} \cdot \left[\mathbf{1}\left(1 - \frac{\mathbf{v}' \cdot \mathbf{k}}{\omega}\right) + \frac{\mathbf{v}'\mathbf{k}}{\omega}\right] \cdot \frac{\partial f_0(\mathbf{p}')}{\partial \mathbf{p}'}. \tag{2.21}
$$

The particles follow the zero-order trajectory in the field, namely

$$
\frac{d\mathbf{p}'}{dt'} = \frac{qB_0}{c}\mathbf{v}' \times \hat{\mathbf{z}} = \omega_c \mathbf{p}' \times \hat{\mathbf{z}}. \tag{2.22}
$$

Here $\omega_c = qB_0/(\gamma mc) = \Omega/\gamma$. The solution to Eq. (2.22) reaches $\mathbf{r}' = \mathbf{r}$ and $\mathbf{v}' = \mathbf{v}$ at $t' = t$ and can be solved with the help of the definitions given in Eq. (2.15) and the following expressions:

$$
\begin{aligned}
\tau &= t = t', \\
v'_x &= v_\perp \cos\left(\phi + \omega_c \tau\right), \\
v'_y &= v_\perp \sin\left(\phi + \omega_c \tau\right), \\
v'_z &= v_\parallel, \\
x' &= x - \frac{v_\perp}{\omega_c}[\sin\left(\phi + \omega_c \tau\right) - \sin\phi], \\
y' &= y + \frac{v_\perp}{\omega_c}[\cos\left(\phi + \omega_c \tau\right) - \cos\phi], \\
z' &= z - v_\parallel \tau.
\end{aligned}
\tag{2.23}
$$

The argument of the exponential term for the electric field can be written as

$$
\mathbf{k} \cdot \mathbf{r}' - \omega t' = \mathbf{k} \cdot \mathbf{r} - \omega t + \beta, \tag{2.24}
$$

where

$$
\beta = -\frac{k_\perp v_\perp}{\omega_c}[\sin\left(\phi - \theta + \omega_c \tau\right) - \sin(\phi - \theta)] + (\omega - k_\parallel v_\parallel)\tau. \tag{2.25}
$$

Finally, we define the following useful derivative operators which arise when evaluating Eq. (2.21),

$$
\begin{aligned}
U &= \frac{\partial f_0}{\partial p_\perp} + \frac{k_\parallel}{\omega}\left(v_\perp \frac{\partial f_0}{\partial p_\parallel} - v_\parallel \frac{\partial f_0}{\partial p_\perp}\right), \\
V &= \frac{k_\perp}{\omega}\left(v_\perp \frac{\partial f_0}{\partial p_\parallel} - v_\parallel \frac{\partial f_0}{\partial p_\perp}\right),
\end{aligned}
\tag{2.26}
$$

which allow f_1 to be written as

$$f_1(\mathbf{r},\mathbf{p},t) = -qe^{i\mathbf{k}\cdot\mathbf{r}-i\omega t}\int_0^\infty d\tau e^{i\beta}\Big\{E_x U\cos(\phi+\omega_c\tau) + E_y U\sin(\phi+\omega_c\tau)$$
$$+ E_z\left[\frac{\partial f_0}{\partial p_\parallel} - V\cos(\phi+\omega_c\tau-\theta)\right]\Big\}. \qquad (2.27)$$

Rewriting Eq. (2.27) in Fourier form leads to the expression

$$f_k = -\,q\int_0^\infty d\tau e^{i\beta}\Big\{\cos(\phi-\theta+\omega_c\tau)\left[\left(E_k^+ + E_k^-\right)U - E_{kz}V\right]$$
$$-i\sin(\phi-\theta+\omega_c\tau)(E_k^+ - E_k^-)U + E_{kz}\frac{\partial f_0}{\partial p_\parallel}\Big\}. \qquad (2.28)$$

We can now evaluate the integral over ϕ, which can be carried out using some Bessel function identities (Montgomery & Tidman, 1964), the details of which can be found in Eq. (10-43) and Table 14-1 in Stix (1992). These relations are of the form

$$\int_0^{2\pi} d\phi\, e^{-ib[\sin(\phi+\omega_c\tau)-\sin\phi]}G(\phi,\tau) = 2\pi\sum_{l=-\infty}^{\infty} e^{-il\omega_c\tau}H(l,b), \qquad (2.29)$$

where $G(\phi,\tau)$ is a trigonometric function (e.g. $\cos(\phi+\omega_c\tau)$ etc.) and $H(l,b)$ is a function depending on the products of Bessel functions (e.g. $J_l(b)^2$ etc.). Here, $b = k_\perp v_\perp/\omega_c$ and $J_l(b)$ is a Bessel function of the first kind of order l. These expressions allow the integral to be evaluated as follows:

$$\int_0^{2\pi} \frac{d\phi}{2\pi} \nabla_{\mathbf{p}} \cdot \left[\left(\mathbf{E_k} + \frac{\mathbf{v} \times \mathbf{B_k}}{c} \right)^* f_k \right]$$
$$= \sum_{l=-\infty}^{\infty} \left\{ \left[(E_k^+ + E_k^-)S - E_{kz}R \right] \frac{l}{b} J_l(b) \right.$$
$$\left. + (E_k^+ - E_k^-)S J_l'(b) + E_{kz} J_l(b) \frac{\partial}{\partial p_\parallel} \right\}^* \tag{2.30}$$
$$\times \left[-q \int_0^\infty d\tau e^{i(\omega - k_\parallel v_\parallel - n\omega_c)\tau} \right] \left\{ \frac{l}{b} J_l(b) [(E_k^+ + E_k^-)U - E_{kz}V] \right.$$
$$+ J_l'(b)(E_k^+ - E_k^-)U + J_l(b) E_{kz} \frac{\partial f_0}{\partial p_\parallel},$$

where $J_l'(b)$ is the first derivative of $J_l(b)$ with respect to b. The integration over τ for each term takes the form

$$\int_0^\infty d\tau e^{i(\omega - k_\parallel v_\parallel - l\omega_c)\tau} = \frac{i}{\omega - k_\parallel v_\parallel - l\omega_c}, \tag{2.31}$$

where the $e^{-il\omega_c\tau}$ term is a result of the integration over ϕ described above. After some further algebra (see Eqs. (17-37) and (17-38) in Stix (1992)) we reach the reasonably compact expression

$$\int_0^{2\pi} \frac{d\phi}{2\pi} \nabla_{\mathbf{p}} \cdot \left[\left(\mathbf{E_k} + \frac{\mathbf{v} \times \mathbf{B_k}}{c} \right)^* f_k \right]$$
$$= -iq \sum_{l=-\infty}^{\infty} S \psi_{lk}^* \frac{1}{\omega - k_\parallel v_\parallel - l\omega_c} \psi_{lk} U, \tag{2.32}$$

where

$$\psi_{lk} = E_k^+ J_{l-1}(b) + E_k^- J_{l+1}(b) + \frac{p_\parallel}{p_\perp} E_{kz} J_l(b). \tag{2.33}$$

For shear Alfvén waves, the wave mode investigated throughout this work, $E_{kz} \to 0$ and $b \ll 1$, or indeed $b = 0$ in the ideal case. As a result, the only contributions to ψ_k that will be significant are those containing Bessel functions of order 0. For small arguments,

$$J_l(b) \approx \frac{1}{\Gamma(l+1)} \left(\frac{b}{2}\right)^l, \tag{2.34}$$

so all the other terms will be negligible. The sum can therefore be restricted to $l = \pm 1$, resulting in

$$\begin{aligned} &\int_0^{2\pi} \frac{d\phi}{2\pi} \nabla_{\mathbf{p}} \cdot \left[\left(\mathbf{E_k} + \frac{\mathbf{v} \times \mathbf{B_k}}{c} \right)^* f_k \right] \\ &\qquad = -\frac{iq}{4} \sum_{l=\pm 1} S \frac{|E_k|^2}{\omega - k_\parallel v_\parallel - l\omega_c} U, \end{aligned} \tag{2.35}$$

where we have used the fact that for $l = \pm 1$, $\psi_{lk} = E_k^\pm$, and $|E_k^\pm|^2 = E_{kx}^2 + E_{ky}^2 = |E_k|^2$.

The final step of the derivation is to take advantage of the Sokhotski–Plemelj theorem to write (Stix, 1992),

$$\frac{1}{\omega - l\omega_c - k_\parallel v_\parallel} = \mathrm{PV}\left(\frac{1}{\omega - l\omega_c - k_\parallel v_\parallel}\right) - i\pi\delta(\omega - l\omega_c - k_\parallel v_\parallel), \tag{2.36}$$

where PV denotes the principal value and δ is the Dirac delta function. The principal value part can be simplified further by including the imaginary part of the wave frequency so that $\omega = \omega_k = \omega_{kr} + i\gamma_k$, with $|\gamma_k| \ll |\omega_{kr}|$. Noting that $\omega_{-k} = -\omega_k^* = -\omega_{kr} + i\gamma_k$ we can write

$$\begin{aligned} &PV\left(\frac{1}{\omega_k - l\omega_c - k_\parallel v_\parallel}\right) + PV\left(\frac{1}{\omega_{-k} - l\omega_c + k_\parallel v_\parallel}\right) \\ &= PV\left(\frac{1}{\omega_{kr} - l\omega_c - k_\parallel v_\parallel + i\gamma_k}\right) + PV\left(\frac{1}{\omega_{-kr} - l\omega_c + k_\parallel v_\parallel - i\gamma_k}\right) \\ &\approx 2i\gamma_k \frac{\partial}{\partial \omega_{kr}} PV\left(\frac{1}{\omega_{kr} - l\omega_c - k_\parallel v_\parallel}\right). \end{aligned} \tag{2.37}$$

This allows us to reach the final form of the quasilinear kinetic equation for a relativistic plasma, as used in Long & Pe'er (2023, 2025a). This is analogous to the non-relativistic version used in Yoon et al. (2009). The final form is

$$\begin{aligned}\frac{\partial F}{\partial t} \;=\; & \frac{e^2}{4}\sum_{l=\pm1}\int d\mathbf{k}\frac{1}{p_\perp}\left[\left(1-\frac{k_\parallel p_\parallel}{\gamma m\omega}\right)\frac{\partial}{\partial p_\perp}+\frac{k_\parallel p_\perp}{\gamma m\omega}\frac{\partial}{\partial p_\parallel}\right] \\ & \times\left\{p_\perp\left[\pi\delta\left(\omega-l\omega_c-\frac{k_\parallel p_\parallel}{\gamma m}\right)|E_k|^2\right.\right. \\ & \left.-\frac{\partial}{2\partial\omega}\left(PV\left(\frac{1}{\omega-l\omega_c-\frac{k_\parallel p_\parallel}{\gamma m}}\right)\right)\frac{\partial|E_k|^2}{\partial t}\right] \\ & \left.\times\left[\left(1-\frac{k_\parallel p_\parallel}{\gamma m\omega}\right)\frac{\partial}{\partial p_\perp}+\frac{k_\parallel p_\perp}{\gamma m\omega}\frac{\partial}{\partial p_\parallel}\right]F\right\}, \end{aligned} \tag{2.38}$$

where we have replaced f_0 by F and used $\frac{\partial}{\partial t}|E_k|^2 = 2\gamma_k|E_k|^2$. This equation can also be derived by following the method in Yoon et al. (2009), who noted that the resonant quasilinear equation can be generalised by replacing the δ function by the sum of a δ function and principal value term (Yoon et al., 2009).

2.3 Maser emission

To calculate the growth rate of a given wave mode, the dispersion relation for the particle distribution in question must be solved. In this section, we describe the dispersion relation and outline how the growth rate for maser emission can be calculated. The derivations presented are primarily sourced from Chapter 10 of Stix (1992) and Wu (1985).

The general form of the dispersion relation is

$$\Lambda = \det(\mathbf{\Lambda}) = 0, \tag{2.39}$$

where the elements of $\mathbf{\Lambda}$ are given by

$$\Lambda_{ij} = N_r^2 \left(\frac{k_i k_j}{k^2} - \delta_{ij} \right) + \varepsilon_{ij}(\mathbf{k}, \omega). \tag{2.40}$$

Here, $N_r = kc/\omega$ is the refractive index and $\boldsymbol{\varepsilon}$ is the dielectric tensor. The dielectric tensor describes the response of the plasma to an electric field $\mathbf{E}$ such that

$$\nabla \times \mathbf{B} = \frac{1}{c}\frac{\partial \mathbf{E}}{\partial t} + \frac{4\pi \mathbf{j}}{c} = \frac{1}{c}\frac{\partial (\boldsymbol{\varepsilon} \cdot \mathbf{E})}{\partial t}, \tag{2.41}$$

and can be written in terms of the susceptibility $\boldsymbol{\chi}$ as

$$\boldsymbol{\varepsilon}(\mathbf{k}, \omega) = \mathbf{1} + \sum_s \boldsymbol{\chi}_s(\mathbf{k}, \omega). \tag{2.42}$$

As previously, the sum over s denotes the sum over the different components of a particle distribution and over the different particle species if present. The susceptibility is linked to the plasma current $\mathbf{j}$ through the linear relation

$$\mathbf{j}_s = \boldsymbol{\sigma}_s \cdot \mathbf{E} = \frac{-i\omega}{4\pi} \boldsymbol{\chi_s} \cdot \mathbf{E}, \tag{2.43}$$

where $\boldsymbol{\sigma}$ is the plasma conductivity.

Eq. (2.43) allows us to calculate the susceptibility for a given particle distribution with the aid of the Vlasov equation for a collisionless plasma given by Eq. (2.12) as well as the definition of the plasma current

$$\mathbf{j} = \sum_s q_s \int d^3\mathbf{p} \mathbf{v_s} f_s. \tag{2.44}$$

The solution to the first-order Vlasov equation can now be used to determine the first-order plasma current $\mathbf{j}$ and hence the susceptibility for an arbitrary distribution f_0. The current is calculated by taking the velocity moment of f_1 and is linked to the susceptibility tensor $\boldsymbol{\chi}$ through Eq. (2.43):

$$\mathbf{j} = \sum_s \mathbf{j_s} = \sum_s q_s \int d^3\mathbf{p}\mathbf{v_s} f_{s1}(\mathbf{r},\mathbf{p},t) = -\frac{i\omega}{4\pi}\sum \boldsymbol{\chi_s}\cdot\mathbf{E}. \tag{2.45}$$

We have already derived the expression for f_{s1} in Sec. 2.2, and the relevant form is given in Eq. (2.27). As in Sec. 2.2, the integration over the azimuthal angle can be evaluated with the aid of the Bessel function relations given by Eq. (2.29). Similarly, the integrals over τ also all take the same form as in Eq. (2.31). The simplification $k_y = 0$ has also been made. These steps lead to the following expression for the susceptibility tensor:

$$\boldsymbol{\chi}_s = \frac{\omega_{ps}^2}{\omega\Omega_s}\sum_{l=-\infty}^{\infty}\int_0^{\infty} 2\pi p_\perp dp_\perp \int_{\infty}^{\infty} dp_\parallel \left(\frac{\omega_c}{\omega - k_\parallel v_\parallel - l\omega_c}\right)\mathbf{S_l}, \tag{2.46}$$

where

$$\mathbf{S_l} = \begin{pmatrix} \frac{l^2 J_l^2(b)}{b^2} p_\perp U & \frac{ilJ_l(b)J_l'(b)}{b} p_\perp U & \frac{lJ_l^2(b)}{b} p_\perp W \\ -\frac{ilJ_l(b)J_l'(b)}{b} p_\perp U & J_l'^2(b) p_\perp U & -iJ_l(b)J_l'(b) p_\perp W \\ \frac{lJ_l^2(b)}{b} p_\parallel U & iJ_l(b)J_l'(b) p_\parallel U & J_l^2(b) p_\parallel W \end{pmatrix}. \tag{2.47}$$

Here, W is a further derivative operator defined as

$$W = \left(1 - \frac{l\omega_{cs}}{\omega}\right)\frac{\partial f_{0s}}{\partial p_\parallel} + \frac{n\omega_{cs}}{\omega p_\perp}\frac{\partial f_{0s}}{\partial p_\perp}. \tag{2.48}$$

Eq. (2.46) can be further manipulated (see e.g. Equations 10-46 and 10-47 in Stix (1992)) into the following final form which is used throughout this work to calculate maser growth rates:

$$\begin{aligned} \boldsymbol{\chi}_s = 2\pi\frac{\omega_{ps}^2}{\omega^2}\int_{-\infty}^{\infty} \mathrm{d}u_\parallel \int_0^{\infty} \mathrm{d}u_\perp & \left\{\frac{u_\parallel}{\gamma}\left(u_\perp \frac{\partial}{\partial u_\parallel} - u_\parallel \frac{\partial}{\partial u_\perp}\right)\right\} \\ \times F_s(u_\parallel, u_\perp)\hat{\mathbf{e}}_\mathbf{z}\hat{\mathbf{e}}_\mathbf{z} + \omega & \left[\frac{\partial}{\partial u_\perp} + \frac{k_\parallel}{\gamma\omega}\left(u_\perp\frac{\partial}{\partial u_\parallel} - u_\parallel\frac{\partial}{\partial u_\perp}\right)\right] \\ \times F_s(u_\parallel, u_\perp) & \sum_{l=-\infty}^{\infty}\frac{\mathbf{T_l}}{\gamma\omega - l\Omega_s - k_\parallel u_\parallel}. \end{aligned} \tag{2.49}$$

Here, $\mathbf{u} = \mathbf{p}/m$ and $F_s = f_{0s}$. The tensor $\mathbf{T_l}$ is given by

$$\mathbf{T_l}(b) = \begin{pmatrix} \frac{l^2\Omega_s^2}{k_\perp^2} J_l^2(b) & -i\frac{l\Omega_s}{k_\perp} u_\perp J_l(b) J_l'(b) & \frac{l\Omega_s}{k_\perp} u_\parallel J_l^2(b) \\ i\frac{l\Omega_s}{k_\perp} u_\perp J_l(b) J_l'(b) & u_\perp^2 J_l'^2(b) & i u_\perp u_\parallel J_l(b) J_l'(b) \\ \frac{l\Omega_s}{k_\perp} u_\parallel J_l^2(b) & -i u_\perp u_\parallel J_l(b) J_l'(b) & u_\parallel^2 J_l^2(b) \end{pmatrix}. \quad (2.50)$$

As in Sec. 2.2, the integral may be calculated by taking advantage of the Sokhotski–Plemelj theorem (Stix, 1992),

$$\frac{1}{\gamma\omega - l\Omega_s - k_\parallel u_\parallel} = \mathrm{PV}\left(\frac{1}{\gamma\omega - l\Omega_s - k_\parallel u_\parallel}\right) - i\pi\delta(\gamma\omega - l\Omega_s - k_\parallel u_\parallel). \quad (2.51)$$

When calculating the maser growth we retain only the δ function term as we are dealing with a resonant process (e.g. Wu, 1985). This δ-function defines the resonance condition and determines which parts of the distribution function contribute to either growth or damping of the electromagnetic waves. If $N_r \cos\theta < 1$, the delta function defines a resonance ellipse in momentum space, with the resonant perpendicular momentum given by

$$\frac{u_l}{c} = \sqrt{(N_r \cos^2\theta - 1)\frac{u_\parallel^2}{c^2} + 2\frac{l\Omega_s}{\omega_r} N_r \cos\theta \frac{u_\parallel}{c} + \left(\frac{l^2\Omega_s^2}{\omega_r^2} - 1\right)}. \quad (2.52)$$

In contrast, if $N_r \cos\theta > 1$, the resonance condition takes the form of a hyperbola, while if $N_r \cos\theta = 1$ it can be described as a parabola. For the particle distributions in this work, the peak growth rate will typically be for propagation angles close to the perpendicular, and as such the resonance condition can be described by the expression for an ellipse given in Eq. (2.52).

As described in Sec. 1.3.1, the wave frequency contains real and imaginary parts such that $\omega = \omega_r + i\omega_i$, whose values can be calculated by solving the dispersion relation. To simplify the calculation of the growth rate and emission frequency, we make the approximation that plasma consists of a thermal component which dominates the dispersion relation (denoted by the subscript 0) and that the component containing the population inversion (denoted by the subscript e) only contributes to the damping or amplification of the modes propagating through the background plasma. In this regime, the growth rate ω_i can be approximated as (Wu, 1985)

$$\frac{\omega_i}{\omega_r} = -\frac{\mathrm{Im}(\Lambda(\mathbf{k},\omega))}{\omega_r \frac{\partial}{\partial \omega_r}(\mathrm{Re}(\Lambda_0(\mathbf{k},\omega_r))}, \tag{2.53}$$

where we have assumed $\omega_i \ll \omega_r$. Here, Λ contains contributions from both $\boldsymbol{\chi}_0$ and $\boldsymbol{\chi}_e$, while Λ_0 only contains the terms from $\boldsymbol{\chi}_0$.

The sign of ω_i clearly depends on the sign of Λ and hence $\boldsymbol{\chi}$. As can be seen from Eq. (2.49), this is determined by the sign of the differential operator

$$\left[\frac{\partial}{\partial u_\perp} + \frac{k_\parallel}{\gamma\omega}\left(u_\perp \frac{\partial}{\partial u_\parallel} - u_\parallel \frac{\partial}{\partial u_\perp}\right)\right] F. \tag{2.54}$$

For perpendicular propagation, $k_\parallel = 0$ and this reduces to $\frac{\partial F}{\partial u_\perp}$. If this term is positive, $\omega_i > 0$ and wave growth will occur, resulting in maser emission. This is the origin of the need for the population inversion of energetic particles introduced in Sec. 1.3.1. In contrast, if the differential operator above is negative, damping will occur with the energy of the wave being transferred to the particle distribution.

To calculate the value of ω_i from Eq. (2.53), the real parts of the wave frequency must first be determined. In Sec. 2.3.1 below we discuss the electromagnetic modes in cold electron-proton and electron-positron plasmas, and describe how they feed into the calculations of the maser growth rate.

2.3.1 Cold plasma dispersion relation

For a general cold plasma, the dispersion relation is given by $\mathrm{Re}\left(\Lambda_0\left(\mathbf{k},\omega\right)\right) = 0$ (e.g. Baldwin et al., 1969), where

$$\Lambda_0 = \begin{vmatrix} \varsigma - N_r^2\cos^2\theta & -ig & N_r^2\cos\theta\sin\theta \\ ig & \varsigma - N_r^2 & 0 \\ N_r^2\cos\theta\sin\theta & 0 & h - N_r^2\sin^2\theta \end{vmatrix}. \tag{2.55}$$

The quantities ς, g and h are given by

$$\begin{aligned} \varsigma &= 1 - \sum_s \frac{\omega_{ps}^2}{\omega_r^2 - \Omega_s^2}, \\ g &= \sum_s \frac{\omega_{ps}^2\Omega_s}{\omega_r(\omega_r^2 - \Omega_s^2)}, \\ h &= 1 - \sum_s \frac{\omega_{ps}^2}{\omega_r^2}. \end{aligned} \tag{2.56}$$

In the case of an electron-proton/ion plasma, the electron contribution is more important as both the plasma and gyration frequencies of the protons/ions are much lower. In contrast, for a pair plasma both species have equal mass so both contributions must be included. However, this mass symmetry also leads the ς_{xy} and ς_{yx} terms to vanish (Stewart & Laing, 1992; Iwamoto, 1993). The resulting cold plasma dispersion relation is therefore

$$\Lambda_0 = \begin{vmatrix} \varsigma - N_r^2\cos^2\theta & 0 & N_r^2\cos\theta\sin\theta \\ 0 & \varsigma - N_r^2 & 0 \\ N_r^2\cos\theta\sin\theta & 0 & h - N_r^2\sin^2\theta \end{vmatrix} = 0. \tag{2.57}$$

To examine the modes supported by such plasmas, we first consider the case of perpendicular propagation. This simplifies the dispersion relation as $\Lambda_{xz} = \Lambda_{zx} = 0$. In both the electron-ion (e-i) and electron-positron (e$^{\pm}$) plasmas this results in two allowed electromagnetic modes. These are referred to as the ordinary (O-) and extraordinary (X-) modes. In the ordinary mode the dispersion relation is the same as in an unmagnetised plasma, and the wave electric field $\mathbf{E_1}$ is parallel to the background magnetic field $\mathbf{B_0}$. The behaviour of this wave is governed by the Λ_{zz} term in the dispersion relation. As it behaves as if the plasma is unmagnetised, it has a lower cut-off (where

$N_r = 0$) at $\omega_O = \omega_{pe}$ for the e-i plasma and at $\omega_O = \omega_{p^\pm}$ for the e$^\pm$ plasma. Here $\omega_{p^\pm}$ is the plasma frequency of the whole pair plasma. The dispersion relation for the O-mode is shown as a solid line in Fig. 2.1a for an e-i plasma and in Fig. 2.1b for a pair plasma.

The X-mode, on the other hand, has an electric field perpendicular to $\mathbf{B_0}$, and depends on the Λ_{yy} term in the dispersion relation. Note that we have assumed $k_y = 0$ throughout this section, hence why the X-mode depends only on the 'yy' term. The extraordinary mode has two branches, with the lower branch often referred to as the Z-mode or slow mode in e-i plasmas. We will refer to this mode as the slow X-mode. The X-mode displays significant differences in behaviour depending on the plasma composition.

In an e-i plasma the mode has two cut-offs and two resonances, where $N_r \to \infty$. The cut-offs are given by

$$\omega_{X^\pm} = \sqrt{\frac{(\Omega_e + \Omega_i)^2}{4} + \omega_{pe}^2 + \omega_{pi}^2} \mp \frac{(\Omega_e - \Omega_i)}{2} \approx \sqrt{\frac{\Omega_e^2}{4} + \omega_{pe}^2} \mp \frac{\Omega_e}{2}, \quad (2.58)$$

while the resonances are found at the lower and upper hybrid frequencies

$$\omega_{UH,LH} = \frac{\omega_{pe}^2 + \omega_{pi}^2 + \Omega_e^2 + \Omega_i^2}{2} \pm \sqrt{\frac{(\omega_{pe}^2 - \omega_{pi}^2 + \Omega_e^2 - \Omega_i^2)^2}{4} + \omega_{pe}^2 \omega_{pi}^2}. \quad (2.59)$$

As the ion frequencies are much lower than the electron frequencies these can be approximated as

$$\begin{aligned} \omega_{UH} &\approx \sqrt{(\omega_{pe}^2 + \Omega_e^2} \\ \omega_{LH} &\approx 0. \end{aligned} \quad (2.60)$$

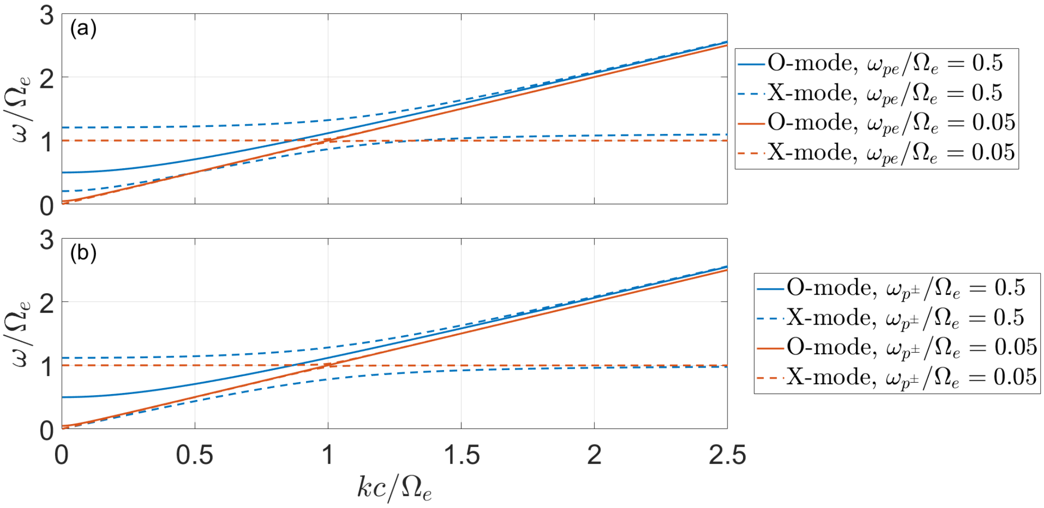

Figure 2.1: The dispersion relation for perpendicular propagation in a cold plasma. **Panel (a)** shows the relation for an electron-proton/ion plasma. The blue lines show the results for $\omega_{pe}/\Omega_e = 0.5$, while the orange lines are for $\omega_{pe}/\Omega_e = 0.05$. The solid lines show the ordinary mode dispersion relation, while the extraordinary modes are shown by dashed lines. The extraordinary mode has cut-offs at $\omega_{X^\pm}$ and a visible resonance at ω_{UH}, placing an upper bound on the slow X-mode. **Panel (b)** shows the dispersion relation for an electron-positron plasma. In this case, the blue lines show the results for $\omega_{p^\pm}/\Omega_e = 0.5$, while the orange lines are for $\omega_{p^\pm}/\Omega_e = 0.05$. The solid and dashed lines have the same meaning as in panel (a). This dispersion relation only has one cut-off at $\omega_X = \sqrt{\omega_{p\pm}^2 + \Omega_e^2}$, while the upper bound on the slow X-mode is provided by the sole resonance at $\omega = \Omega_e$.

Extraordinary mode waves can therefore propagate in the frequency ranges $\omega_{X^-} < \omega < \omega_{UH}$ (for the slow mode) and $\omega > \omega_{X^+}$ for the upper branch. For this reason, the slow mode is a trapped mode and cannot transition to being a vacuum electromagnetic mode without mode conversion taking place.

In a pair plasma the extraordinary mode also has two branches. However, in this case there is only one cut-off due to the mass symmetry. This cut-off occurs at $\omega_X = \sqrt{\omega_{p\pm}^2 + \Omega_e^2}$, while the sole resonance occurs at $\omega_{res} = \Omega_e$. The dispersion relation for the X-mode is shown as a dashed line in Fig. 2.1a for an e-i plasma and in Fig. 2.1b for a pair plasma.

For the plasma of interest, we calculate the growth rates ω_i using Eq. (2.53) for both the ordinary and extraordinary modes. To the lowest order in n_e/n_o, $\mathrm{Im}(\Lambda(\mathbf{k},\omega))$ can be written as

$$\begin{aligned}\mathrm{Im}(\Lambda(\mathbf{k},\omega)) &= \Psi_{xx}\mathrm{Im}(\chi^e_{xx}(\mathbf{k},\omega_r)) + \Psi_{yy}\mathrm{Im}(\chi^e_{yy}(\mathbf{k},\omega_r)) \\ &\quad + \Psi_{zz}\mathrm{Im}(\chi^e_{zz}(\mathbf{k},\omega_r)) + \Psi_{xz}\mathrm{Im}(\chi^e_{xz}(\mathbf{k},\omega_r)) \\ &\quad + \Psi_{xy}\mathrm{Re}(\chi^e_{xy}(\mathbf{k},\omega_r)) + \Psi_{yz}\mathrm{Re}(\chi^e_{yz}(\mathbf{k},\omega_r)),\end{aligned} \tag{2.61}$$

with

$$\begin{aligned}\Psi_{xx} &= N_r^4\sin^2\theta - N_r^2(\varsigma\sin^2\theta + h) + \varsigma h, \\ \Psi_{yy} &= -N_r^2(\varsigma\sin^2\theta + h\cos^2\theta) + \varsigma h, \\ \Psi_{zz} &= N_r^4\cos^2\theta - N_r^2\varsigma(1+\cos^2\theta) + \varsigma^2 - g^2, \\ \Psi_{xy} &= 2g(h - N_r^2\sin^2\theta), \\ \Psi_{xz} &= 2N_r^2(N_r^2 - \varsigma)\sin\theta\cos\theta, \\ \Psi_{yz} &= 2N_r^2 g\sin\theta\cos\theta.\end{aligned} \tag{2.62}$$

As $g = 0$ for the electron-positron plasma, $\Psi_{xy} = \Psi_{yz} = 0$. Combining these equations and finally integrating along the contour defined by the resonance condition allows the growth rate for a given mode to be calculated.

Chapter 3

Non-resonant interactions between Alfvén waves and relativistic plasmas

3.1 Introduction

As discussed in Chapter 1, the identity of the emission mechanism responsible for fast radio bursts remains an open question, prompting the development of numerous theories. All models share the need to explain the extremely high FRB brightness temperatures of up to $T_b \sim 10^{36}$ K (e.g. Katz, 2016a), far in excess of those achievable by incoherent radiation. One of the primary coherent emission mechanisms invoked to explain the observed FRB signal is synchrotron maser emission (SME) (e.g. Lyubarsky, 2014; Long & Pe'er, 2018; Metzger et al., 2019).

The synchrotron maser, or its mildly relativistic equivalent the cyclotron maser, is a proposed emission mechanism not only for FRBs but also for many other coherent astrophysical phenomena such as Auroral Kilometric Radiation (AKR) in the Earth's magnetosphere (Wu & Lee, 1979; Wu, 1985), Jovian Decametric Radiation (e.g. Hewitt et al., 1982), and blazars (Begelman et al., 2005). SME requires a certain set of plasma conditions: (i) an inverse population of energetic electrons, and (ii) a background magnetic field. Once these conditions are satisfied, the interaction between the inverse electron population and electromagnetic waves in the plasma results in negative absorption and stimulated emission for certain plasma parameters (Wu, 1985; Treumann, 2006).

To achieve the required population inversion, the particle distribution must either grow faster than E^2 (Sagiv & Waxman, 2002), or satisfy $\frac{\partial F}{\partial v_\perp} > 0$ (Wu, 1985). Here, $F(v_\perp, v_\parallel)$ is the particle distribution function, $v_\perp(v_\parallel)$ is the velocity perpendicular (parallel) to the background magnetic field, and E is the particle's energy. The process by which this population inversion forms is crucial to understanding the parameter space where SME is a viable emission mechanism. Various processes have been proposed to pump the electrons into the inverse population. Many of these models, such as the 'loss-cone' (Wu, 1985; Freund & Wu, 1976) and 'ring-shell' (Pritchett & Strangeway, 1985; Winglee & Dulk, 1986) models were developed for non- or mildly relativistic scenarios such as AKR.

In the context of FRBs, the environment may be relativistic with temperatures of $k_B T \approx m_e c^2$ (e.g. Babul & Sironi, 2020; Beloborodov, 2020). In previous works (Long & Pe'er, 2023, 2025a), we showed that non-resonant interactions between Alfvén waves and a plasma can produce a population inversion capable of supporting SME with a high efficiency, even in such relativistic plasmas. This mechanism does not require a shock wave as in the other primary models for relativistic SME, where a soliton-like structure is formed at the front of a strongly magnetised shock in which particles gyrate around the enhanced magnetic field and form a semi-coherent ring in momentum space (e.g. Alsop & Arons, 1988; Gallant et al., 1992; Amato & Arons, 2006; Plotnikov & Sironi, 2019). Similar ring distributions may also be formed through radiation reaction cooling (Bilbao & Silva, 2023; Bilbao et al., 2024, 2025).

Non-resonant interactions between the Alfvén waves and the relativistic plasma induce pitch-angle diffusion in low β plasmas, where β is the ratio of the plasma pressure to the magnetic pressure. In the emission regions of FRBs the environment is highly magnetised, satisfying this condition even at relativistic temperatures. The resulting deformation of the initial particle distribution into a crescent shape in momentum space is capable of supporting a population inversion (Zhao et al., 2013; Wu et al., 2014b).

In this chapter, we solve the quasilinear kinetic equation describing the non-resonant interaction between Alfvén waves and a relativistic plasma (Long & Pe'er, 2023, 2025a). The details of how this interaction alters the temperature, kinetic energy and bulk motion of the relativistic plasma are explored. The impact of the interaction on the formation of a population inversion and its application to FRBs is examined in Chapters 4 and 5.

This chapter is organised as follows. In Sec. 3.2 we detail the physical setup of our model and the equations which describe it. The behaviour of the full relativistic quasilinear kinetic equation for different parameters and the numerical methods used to solve the equation are examined in Sec. 3.3. In Sec. 3.4 we present results for the evolution of the properties of the plasma due to the non-resonant interaction, while in Sec. 3.5 we analyse how the results are changed for non-Maxwellian initial distributions. The results are discussed in Sec. 3.6.

3.2 Non-resonant interaction of particles with Alfvén waves: evolution of the particle distribution function

We examine a large parameter space in both temperature T and magnetisation σ. We define

$$\sigma = \frac{B^2}{4\pi w m_s c^2} = \frac{\Omega_s^2}{\omega_{ps}^2 w} \tag{3.1}$$

Here $\Omega_s = eB/m_s c$ is the cyclotron frequency of the plasma as a whole and $\omega_{ps} = \sqrt{4\pi n_s e^2/m_s}$ is the plasma frequency, e is the electron charge, B is the background magnetic field, n_s is the particle number density and w is the specific enthalpy density. The subscript s denotes the plasma species. For a pair plasma the masses in question will be those of electrons, while for an electron-proton/ion plasma the heavier species dominates. We will also use $\bar{\sigma} = \Omega_s^2/\omega_{ps}^2$ as the magnetisation in the cold, non-relativistic plasma case. The entire magnetisation parameter space $\bar{\sigma} > 10^{-4}$ is investigated at temperatures in the range $10^{-3} \leq \theta \leq 3$, where $\theta = \frac{k_B T}{mc^2}$ is the normalised temperature, providing a full picture of the interaction across all the relevant physical parameters.

To examine the problem we consider a relativistic plasma of density n embedded in a background magnetic field $\mathbf{B}$. The initial particle distribution $F_0(p_\parallel, p_\perp, \theta_0)$, is primarily modelled as a Maxwell-Jüttner distribution with temperature θ_0, where $p_\perp = \gamma m v_\perp$ and $p_\parallel = \gamma m v_\parallel$ are the relativistic momenta in the perpendicular and parallel directions to the background magnetic field respectively. Here, $\gamma = (1 + (p_\perp/mc)^2 + (p_\parallel/mc)^2)^{1/2}$ is the Lorentz factor. Other particle distributions (Bi-Maxwellians and beamed distribution) are discussed in Sec. 3.5. The non-resonant interaction between the particles and the waves causes the distribution to evolve, with the details of the development depending on the magnetisation and temperature. This evolved distribution is specified at time t by $F(p_\parallel, p_\perp, t)$. In order for non-resonant interactions to occur, it is necessary for Alfvén waves to propagate through the plasma in addition to the steady background magnetic field. In a typical FRB scenario, the Alfvén waves are generated by a central neutron star/magnetar, resulting in a wavevector that is expected to be in the parallel direction only. The spectral magnetic and electric fields of the waves are denoted as B_k and E_k respectively, where k is the wavenumber. The waves are assumed to vary slowly in time, and to have a broad spectrum (Wu & Yoon, 2007; Yoon et al., 2009).

We use kinetic theory to study the interaction between the waves and particles. The quasilinear approximation of this theory (Vedenov et al., 1961;

Drummond & Rosenbluth, 1962) is used to determine how the particle distribution changes due to the interaction with the Alfvén waves. As described in Chapter 2, the variables of the Vlasov equation are split into slowly varying average and first order fluctuation terms. The complete equation, which contains both the resonant (line 2) and the non-resonant (line 3) terms, and is correct in both relativistic and non-relativistic regimes, is

$$\begin{aligned}\frac{\partial F}{\partial t} = & \frac{e^2}{4}\sum_{l=\pm1}\int d\mathbf{k}\frac{1}{p_\perp}\left[\left(1-\frac{k_\parallel p_\parallel}{\gamma m\omega}\right)\frac{\partial}{\partial p_\perp}+\frac{k_\parallel p_\perp}{\gamma m\omega}\frac{\partial}{\partial p_\parallel}\right] \\ & \times\left\{p_\perp\left[\pi\delta\left(\omega-l\omega_c-\frac{k_\parallel p_\parallel}{\gamma m}\right)|E_k|^2\right.\right. \\ & \left.-\frac{\partial}{2\partial\omega}\left(PV\left(\frac{1}{\omega-l\omega_c-\frac{k_\parallel p_\parallel}{\gamma m}}\right)\right)\frac{\partial|E_k|^2}{\partial t}\right] \\ & \left.\times\left[\left(1-\frac{k_\parallel p_\parallel}{\gamma m\omega}\right)\frac{\partial}{\partial p_\perp}+\frac{k_\parallel p_\perp}{\gamma m\omega}\frac{\partial}{\partial p_\parallel}\right]F\right\},\end{aligned} \tag{3.2}$$

as derived in Chapter 2. Here, as in Chapter 2, $\omega_c = eB/\gamma mc$ is the particle gyration frequency; ω is the Alfvén wave frequency (whose dispersion relation is described in Sec. 3.2.1 below) and l is the harmonic number. We have omitted the species subscript for clarity. The integration is over the Alfvénic wavevector $\mathbf{k}$, which is assumed to be in the direction parallel to $\mathbf{B_0}$, as described above.

The equation is governed by whether the resonance condition

$$\omega - l\omega_c - \frac{k_\parallel p_\parallel}{\gamma m} = 0 \tag{3.3}$$

is satisfied. While this is the case in many plasmas, it is not in FRB emission regions. Due to strong magnetic fields, plasmas in these environments tend to have a low β. For Alfvén waves in such a plasma, the inequalities $\omega_c \gg \omega$ and $\omega_c \gg \frac{k_\parallel p_\parallel}{\gamma m}$ hold (Wu & Yoon, 2007), resulting in no contribution from the resonant term. Furthermore, as is shown below, even in plasmas with higher β values the resonance condition may not be satisfied if the maximum wavenumber of the system is sufficiently small. The presence of the $\frac{\partial |E_k|^2}{\partial t}$ term requires that the Alfvén wave electric field varies temporally in the non-resonant case, a restriction that is not found in the resonant regime.

To ensure that the above conditions are always satisfied, the maximum wavenumber of the Alfvén wave, $k_{\rm max}$, must not be too large. Assuming an Alfvén relation of $\omega = kc$ in the highly magnetised and relativistic case, the condition for the non-resonant interaction to remain dominant becomes $\omega_c \gg k_{\rm max} c$. We can further assume that the Alfvén wave is generated by some instability of the neutron star such as a quake (Blaes et al., 1989). Thus the wavelength $\lambda = \xi R_*$ will be some fraction ξ of the neutron star radius R_*, with a corresponding wavenumber of $k \sim 2\pi/(\xi R_*)$. The condition of validity thus becomes $2\pi c/(\omega_c R_*) \ll \xi$. Using fiducial values of $R_* = 10^6$ cm and $\omega_c = 10^9$ rad s^{-1}, which is appropriate for FRBs, we obtain the condition $\xi \gg 2 \times 10^{-4} \omega_{c,9}^{-1} R_{*,6}^{-1}$, where we use the convention $Q = 10^x Q_x$ in cgs units. Typical wavelengths of waves in neutron star crusts are estimated to be of the order of $\lambda \sim 10^4$ cm to $\lambda \sim 10^7$ cm, the equivalent of $\xi \sim 10^{-2} R_{*,6}^{-1}$ to $\xi \sim 10 R_{*,6}^{-1}$(Blaes et al., 1989; Beloborodov, 2023). Therefore, the maximum value of $k_{\rm max}$ will not exceed a fraction of ω_c/c, confirming that the interaction will remain in the non-resonant regime. In low magnetisation cases, the value of $k_{\rm max}$ will be lower due to the reduced Alfvén velocity, resulting in an even less restrictive limit.

The non-resonant term can itself be simplified through the approximation (Yoon et al., 2009):

$$\frac{\partial}{2\partial\omega}\left(PV\left(\frac{1}{\omega - l\omega_c - \frac{k_\parallel p_\parallel}{\gamma m}}\right)\right)\frac{\partial\,|E_k|^2}{\partial t} \approx -\frac{1}{2\omega_c^2}\frac{\partial\,|E_k|^2}{\partial t}. \tag{3.4}$$

In order to present Eq. (3.2) more clearly, we expand the equation and separate the terms, using the $l = \pm 1$ harmonics. The resulting expression is

$$
\begin{aligned}
\frac{\partial F}{\partial t} = \frac{e^2}{4m^2c^2\omega_c^2} \Bigg\{ & \left(\frac{I_1\left(2 + \frac{q_\perp^2}{\gamma^2}\right)}{\gamma} - 2\frac{I_2 q_\parallel}{\gamma^2} \right) \frac{\partial F}{\partial q_\parallel} \\
& + \left[\frac{1}{q_\perp} \left(I_3 \left(1 + 2\frac{q_\perp^2}{\gamma^2} \right) + \frac{I_2 q_\parallel^2}{\gamma^2} - \frac{I_1 q_\parallel \left(2 + \frac{q_\perp^2}{\gamma^2}\right)}{\gamma} \right) \right. \\
& \left. - \frac{I_2 q_\perp}{\gamma^2} \right] \frac{\partial F}{\partial q_\perp} \\
& + \frac{I_2 q_\perp^2}{\gamma^2} \frac{\partial^2 F}{\partial q_\parallel^2} \\
& + \left(I_3 + \frac{I_2 q_\parallel^2}{\gamma^2} - 2\frac{I_1 q_\parallel}{\gamma} \right) \frac{\partial^2 F}{\partial q_\perp^2} \\
& + \left(2\frac{I_1 q_\perp}{\gamma} - 2\frac{I_2 q_\perp q_\parallel}{\gamma^2} \right) \frac{\partial^2 F}{\partial q_\parallel \partial q_\perp} \Bigg\},
\end{aligned} \tag{3.5}
$$

where $q = p/mc = \gamma\frac{v}{c} = \gamma\beta$, and $I_1 = \int d\mathbf{k}\frac{\partial|E_k|^2}{\partial t}\frac{ck_\parallel}{\omega}$, $I_2 = \int d\mathbf{k}\frac{\partial|E_k|^2}{\partial t}\frac{c^2k_\parallel^2}{\omega^2}$ and $I_3 = \int d\mathbf{k}\frac{\partial|E_k|^2}{\partial t}$. Eq. (3.5) is correct in the limit of strong magnetic fields, in both the relativistic and non-relativistic regimes.

Each line in Eq. (3.5) describes a different component of the overall evolution, which we respectively denote as $\left(\frac{\partial F}{\partial t}\right)_x$. From top to bottom, these terms describe parallel advection $\left(\frac{\partial F}{\partial t}\right)_{\parallel,1}$, perpendicular advection $\left(\frac{\partial F}{\partial t}\right)_{\perp,1}$, parallel diffusion $\left(\frac{\partial F}{\partial t}\right)_{\parallel,2}$, perpendicular diffusion $\left(\frac{\partial F}{\partial t}\right)_{\perp,2}$ and a mixed term $\left(\frac{\partial F}{\partial t}\right)_{mix}$.

3.2.1 Dispersion relation of the Alfvén waves

In order to solve the time evolution of the distribution function described by Eq. (3.5), one needs to evaluate the integrals I_1, I_2 and I_3. The integrals I_1 and I_2 are calculated using either the non-relativistic Alfvén dispersion relation $\omega = kv_A$, where v_A is the Alfvén velocity, or the full relativistic solution given by (Asenjo et al., 2009; Muñoz et al., 2014),

$$\omega^2 - c^2k^2 = \sum_s \omega_{ps}^2 \frac{\omega'}{f_s\bar{\gamma}_s\omega' - \Omega_s}. \tag{3.6}$$

Here $\omega' = \omega - kv_0$; v_0 is the particles' bulk velocity (in case it is non-zero); $f_s = K_3\left(\frac{m_sc^2}{k_BT_s}\right) \Big/ K_2\left(\frac{m_sc^2}{k_BT_s}\right)$ is the plasma's enthalpy; $\bar{\gamma}_s$ is the species Lorentz factor. K_l denotes a modified Bessel function of the second kind of order l.

In the non-relativistic regime the ratios between the integrals are simply given by $I_1 = \frac{v_A}{c}I_2 = \frac{c}{v_A}I_3$. In this limit therefore $I_2 > I_1 > I_3$ for all $v_A < c$. This relationship also holds in the relativistic case, provided that $k_{\max}$ is sufficiently small that the $\omega - k$ relationship remains linear, which is the case for the parameter space examined in this work.

To demonstrate this, expanding Eq. (3.6) for a two species plasma gives

$$\omega^2 - c^2k^2 = \omega_{p-}^2 \frac{\omega'}{f_-\bar{\gamma}_-w' - \Omega_-} + \omega_{p+}^2 \frac{\omega'}{f_+\bar{\gamma}_+w' - \Omega_+}, \tag{3.7}$$

where the subscript + denotes the positively charged species and the subscript − denotes the electrons. Defining $\mu = m_+/m_-$ as the mass ratio of the two species and assuming both species have equal f and $\bar{\gamma}$, the above equation can be written as

$$\omega^2 - \omega\left(\frac{\omega_{p+}^2}{f\bar{\gamma}\omega - \Omega_+} + \frac{\mu\omega_{p+}^2}{f\bar{\gamma}\omega + \mu\Omega_+}\right) - c^2k^2 = 0, \tag{3.8}$$

for particles with zero bulk velocity. In the low frequency limit, $f\bar{\gamma}\omega < \Omega_+$, one can make the following approximations:

$$\begin{aligned} \frac{\omega_{p+}^2}{f\bar{\gamma}\omega - \Omega_+} &\approx -\frac{\omega_{p+}^2}{\Omega_+}\left(1 + \frac{f\bar{\gamma}\omega}{\Omega_+}\right) \\ \frac{\mu\omega_{p+}^2}{f\bar{\gamma}\omega + \mu\Omega_+} &\approx \frac{\omega_{p+}^2}{\Omega_+}\left(1 - \frac{f\bar{\gamma}\omega}{\mu\Omega_+}\right). \end{aligned} \tag{3.9}$$

The term in brackets in Eq. (3.8) can therefore be written as

$$\left(\frac{\omega_{p+}^2}{f\bar{\gamma}\omega - \Omega_+} + \frac{\mu\omega_{p+}^2}{f\bar{\gamma}\omega + \mu\Omega_+}\right) \approx -\frac{f\bar{\gamma}\omega\omega_{p+}^2}{\Omega_+^2}\left(1 + \frac{1}{\mu}\right), \tag{3.10}$$

and the entire dispersion relation can therefore be approximated as

$$\omega^2\left(1 + \frac{f\bar{\gamma}\omega_{p+}^2}{\Omega_+^2}\left(1 + \frac{1}{\mu}\right)\right) \approx c^2k^2, \tag{3.11}$$

showing that the relativistic Alfvén wave dispersion relation is linear in the low frequency regime of interest to this work, with a corresponding relativistic Alfvén velocity of $v_{A,rel} = c\left(1 + \frac{f\bar{\gamma}\omega_{p+}^2}{\Omega_+^2}\left(1 + \frac{1}{\mu}\right)\right)^{-1/2}$.

3.2.2 Spectrum of the Alfvén wave

The outcome of the wave-particle interaction is insensitive to the precise spectrum chosen, provided that the Alfvén wave dispersion relation is linear, as in this case $I_1 = \frac{v_{A,rel}}{c} I_2 = \frac{c}{v_{A,rel}} I_3$ always holds. We demonstrate this below. Consider waves having a power-law spectrum where the spectral electric field is given by $E_k(t) = E_0(t)k^{-\varphi}$. Using $\frac{\partial |E_k(t)|^2}{\partial t} = 2\Gamma_k E_k(t)^2$, where Γ_k is the spectral growth rate of the Alfvén wave, the terms I_1, I_2 and I_3 become

$$\begin{aligned}
I_1 &= 2\int d\mathbf{k}\Gamma_k E_0^2 k_\parallel^{-2\varphi}\frac{k_\parallel}{\omega} = \frac{2}{v_{A,rel}}\int d\mathbf{k}\Gamma_k E_0^2 k_\parallel^{-2\varphi}, \\
I_2 &= 2\int d\mathbf{k}\Gamma_k E_0^2 k_\parallel^{-2\varphi}\frac{ck_\parallel^2}{\omega^2} = \frac{2c}{v_{A,rel}^2}\int d\mathbf{k}\Gamma_k E_0^2 k_\parallel^{-2\varphi}, \\
I_3 &= 2\int d\mathbf{k}\Gamma_k E_0^2 \frac{k_\parallel^{-2\varphi}}{c} = \frac{2}{c}\int d\mathbf{k}\Gamma_k E_0^2 k_\parallel^{-2\varphi},
\end{aligned} \tag{3.12}$$

with ratios that are independent of the power-law exponent. Note that we explicitly used the assumption that the propagation direction of the Alfvén waves is parallel to the background magnetic field.

The magnitude of each I_x term ($x = 1, 2, 3$), and thus the time-scale and turbulence dependence of the process, is also independent of the precise spectrum provided that: (i) the spectral growth rate Γ_k is a constant and (ii) the total energy contained in the spectra in question is the same.

To illustrate a case which satisfies the above requirements, we continue the example of a power-law spectrum presented in Eq. (3.12) with the added constraint that Γ_k is constant. The I_x terms can be written as

$$\begin{aligned}
I_1 &= \frac{2\Gamma_k E_0^2}{(-2\varphi+1)v_{A,rel}}\left(k_{\max}^{-2\varphi+1} - k_{\min}^{-2\varphi+1}\right), \\
I_2 &= \frac{2\Gamma_k c E_0^2}{(-2\varphi+1)v_{A,rel}^2}\left(k_{\max}^{-2\varphi+1} - k_{\min}^{-2\varphi+1}\right), \\
I_3 &= \frac{2\Gamma_k E_0^2}{(-2\varphi+1)c}\left(k_{\max}^{-2\varphi+1} - k_{\min}^{-2\varphi+1}\right).
\end{aligned} \tag{3.13}$$

Comparing this to a flat spectrum ($\varphi = 0$),the ratio $I_{x,\text{flat}}/I_{x,\text{power-law}}$ is given by

$$\frac{I_{x,\text{flat}}}{I_{x,\text{power-law}}} = \frac{\left(k_{\max}^{-2\varphi+1} - k_{\min}^{-2\varphi+1}\right)}{(k_{\max} - k_{\min})(1-2\varphi)}. \tag{3.14}$$

This is the same factor obtained when comparing the energy density of a flat spectrum $E_k = E_0$ and power-law spectrum $E_k = E_0' k^{-\varphi}$:

$$\begin{aligned}
\int dk E_0^2 &= \int dk E_0'^2 k^{-2\varphi}, \\
E_0^2(k_{\max} - k_{\min}) &= E_0'^2 \frac{\left(k_{\max}^{-2\varphi+1} - k_{\min}^{-2\varphi+1}\right)}{(1-2\varphi)}, \\
\frac{E_0^2}{E_0'^2} &= \frac{\left(k_{\max}^{-2\varphi+1} - k_{\min}^{-2\varphi+1}\right)}{(k_{\max} - k_{\min})(1-2\varphi)},
\end{aligned} \tag{3.15}$$

where we have assumed an equal wavenumber range in both cases. This demonstrates that the magnitudes of the I_x terms, and thus the time-scale of the interaction, are independent of the Alfvén wave spectrum in this case.

3.3 Methods and analysis

3.3.1 Solving the non-resonant wave-particle interaction

To solve Eq. (3.5), a number of numerical schemes were used. These include the Crank-Nicolson, upwind differencing and fully implicit finite difference methods (Press et al., 2007). The equation was solved in `MATLAB` on a term by term basis. The initial conditions are the initial distribution function F_0, which is taken to be a Maxwell-Jüttner distribution with a normalised temperature $\theta = \frac{k_B T}{mc^2}$; and the magnetisation $\bar{\sigma} = \Omega^2/\omega_p^2$. We assume that $m = m_e$ as we are primarily interested in the scenario of FRBs, in which case the most likely emission environment is the pair wind of a neutron star/magnetar. However, the results can be rescaled appropriately by using the correct Alfvén velocity for other plasma compositions.

The Alfvén wave turbulence is described by the quantity $\eta = \frac{\int d\mathbf{k} B_k^2}{B^2}$, the ratio of the wave to background magnetic field energy density. This ratio is assumed to take the form $\eta(t) = \eta_0 e^{2\Gamma t}$, where η_0 is the initial turbulence level. Based on the discussion in Sec. 3.2.2, we take $\Gamma = \Gamma_k$ as a constant for simplicity. To ensure the quasilinear approximation remains valid, we require $\eta < 1$ and $\Gamma < \Omega$. We further assume a single temperature and density describing all species. The equation is evolved in units of $\tau = \frac{1}{4}\frac{v_{A,rel}^2}{c^2}\left\langle\frac{\partial\eta}{\partial t}\right\rangle t$, where $\left\langle\frac{\partial\eta}{\partial t}\right\rangle$ is the time averaged value. The state of the distribution depends on the turbulence level of the Alfvén waves, and the time to reach a given state depends on the growth rate of this turbulence. The results in Secs. 3.4 are therefore presented in terms of η for clarity.

The distribution function at a given value of τ is calculated by solving Eq. (3.5). This requires calculating the values for the integrals I_1, I_2 and I_3. We use the dispersion relation (Eq. (3.6)) as discussed in Sec. 3.2.1. While the values of these integrals determine the time-scale for reaching a steady state, their ratio determines the amount of energy available in the population inversion.

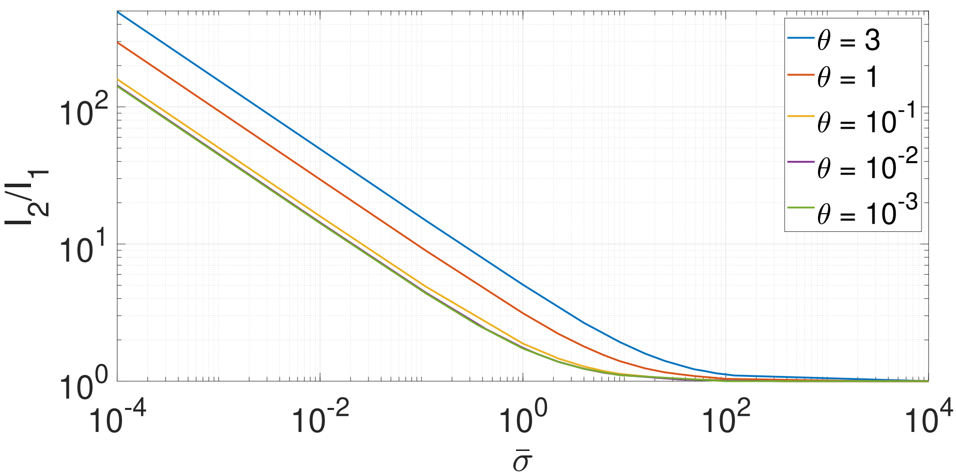

Figure 3.1: The value of I_2/I_1 versus magnetisation $\bar{\sigma}$ for a wavenumber range $0 < k < 0.01\Omega/c$, showing how for a given $\bar{\sigma}$, I_2/I_1 increases with temperature. For $\bar{\sigma} \lessapprox 1$, the relationship between the two quantities is $I_2/I_1 \propto \bar{\sigma}^{-1/2}$.

The ratio I_2/I_1 is presented in Fig. 3.1, showing its dependence on both magnetisation and temperature. This ratio is equal to $I_2/I_1 = c/v_{A,rel}$ in the linear regime, although the numerical results we show are general. The value of I_2/I_1 decreases as the magnetisation increases, asymptoting to a value of $I_2/I_1 = 1$ at a temperature dependent magnetisation of $\bar{\sigma} \gtrapprox 10$. Physically, this occurs when $v_{A,rel}$ approaches c. For lower magnetisations $\bar{\sigma} \lessapprox 1$, the relationship becomes $I_2/I_1 \propto \bar{\sigma}^{-1/2}$. This is to be expected as $v_{A,rel} \propto \bar{\sigma}^{1/2}$. In this regime, the value of I_2/I_1 increases with temperature for all magnetisations in this range due to the decrease in $v_{A,rel}$ at higher temperatures.

Results were obtained across a large parameter space, with temperatures ranging from $\theta = 10^{-3}$ to $\theta = 3$ and magnetisations greater than $\bar{\sigma} \approx 10^{-4}$ examined. As a demonstration of the evolution of the initial Maxwell-Jüttner distribution, Fig. 3.2 shows contour plots of the distribution at $\eta = 0$, $\eta = 0.1$, $\eta = 0.3$ and $\eta = 1$. The results in Fig. 3.2 are for an initial temperature of $\theta = 10^{-2}$ and $I_2/I_1 = 1$, equivalent to $\sigma \gtrapprox 10^2$. The formation of the crescent shape is visible through the extension of the initial distribution to larger values of $q_\perp$ for $q_\parallel > 0$, with the arms of the crescent expanding as the distribution continues to evolve. The numerical results are validated by comparing to the analytical low turbulence solution given in Wu & Yoon (2007) in Appendix A. We examine the overall evolution and properties of the particle distribution function in Secs. 3.4 and 3.5 below, before examining the formation of the crescent-shaped population inversion in detail in Chapter 4.

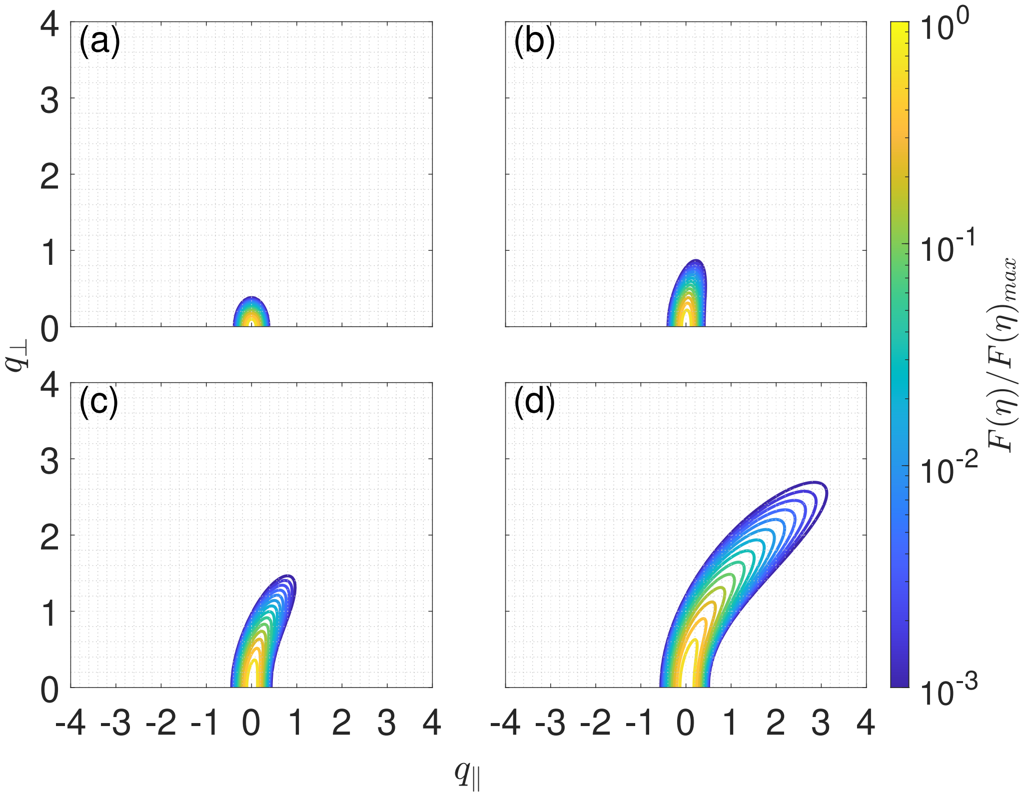

Figure 3.2: Contour plots of the distribution function F for an initial Maxwell-Jüttner distribution in the high magnetisation regime with $\theta = 10^{-2}$ and $I_2/I_1 = 1$. **Panel (a)** shows the initial distribution function F_0; **panel (b)** shows F at $\eta = 0.1$; **panel (c)** shows the distribution at $\eta = 0.3$ and **panel (d)** shows the distribution at $\eta = 1$. The progression from the initial to the final turbulence shows the development of the arms of the crescent-shaped population inversion. The values are normalised to the maximum value of $F(\eta)$ and are plotted on a log scale.

3.4 Results: Maxwellian distributions

A natural way to examine the impact of the non-resonant interaction on the plasma is by examining its effect on the kinetic energy, temperature, and possible bulk motion of the distribution. In this section, we examine the evolved particle distributions resulting from initial Maxwell-Jüttner distributions across a wide range of temperatures and magnetisations.

We define the following physical quantities of relevance to the analysis. The kinetic energy of the distribution is given by

$$\langle KE \rangle = E_{tot} = \int d\mathbf{q}(\gamma(\mathbf{q}) - 1)F(\mathbf{q}). \tag{3.16}$$

The parallel and perpendicular temperatures can be defined through the relativistic pressure such that

$$\begin{aligned} \theta_\perp =& \frac{1}{2}\int d\mathbf{q}\frac{q_\perp^2}{\gamma(\mathbf{q})}F(\mathbf{q}), \\ \theta_\parallel =& \int d\mathbf{q}\frac{q_\parallel^2}{\gamma(\mathbf{q})}F(\mathbf{q}), \end{aligned} \tag{3.17}$$

with the temperature anisotropy given by $A = \theta_\perp/\theta_\parallel$. We also define the average parallel and perpendicular momenta

$$\begin{aligned} \langle q_\perp \rangle =& \int d\mathbf{q}\ q_\perp F(\mathbf{q}), \\ \langle q_\parallel \rangle =& \int d\mathbf{q}\ q_\parallel F(\mathbf{q}), \end{aligned} \tag{3.18}$$

where F has been normalised appropriately in each case.

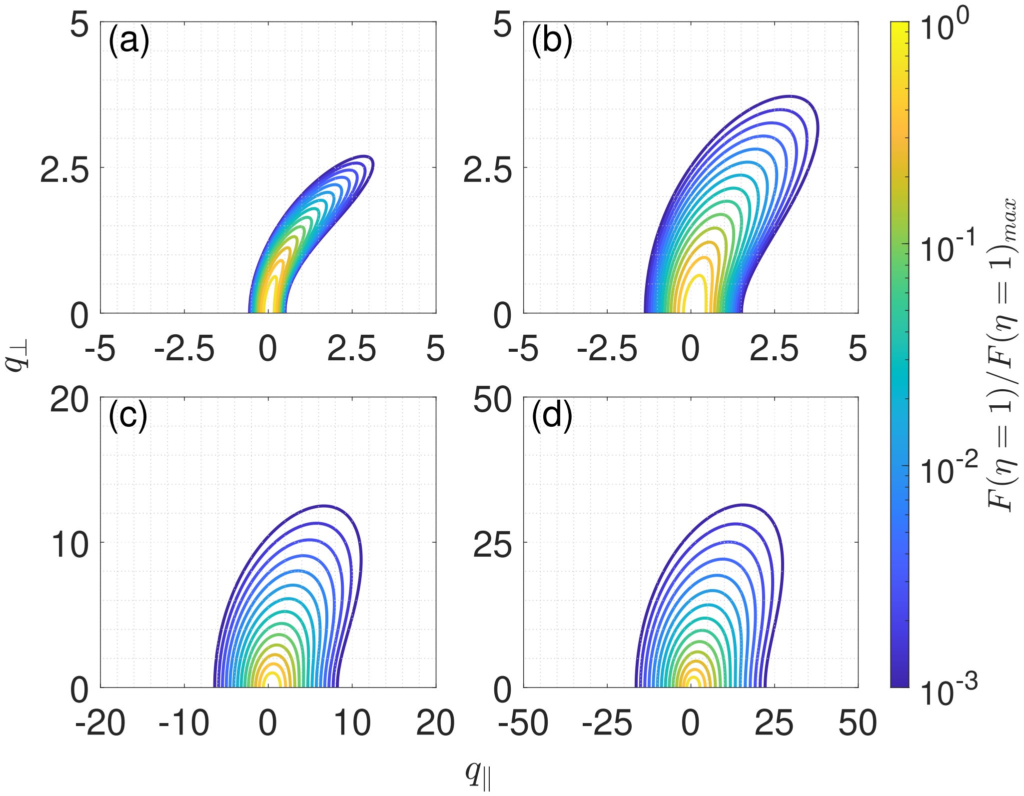

Figure 3.3: Contour plots of the distribution function F at a turbulence level of $\eta = 1$ for an initial Maxwell-Jüttner distribution in the high magnetisation regime $I_2/I_1 = 1$. **Panel (a)** shows the result for an initial temperature of $\theta = 10^{-2}$; **panel (b)** is for $\theta = 10^{-1}$; **panel (c)** has $\theta = 1$ and **panel (d)** has $\theta = 3$. The values are normalised to the maximum value of $F(\eta = 1)$ and are plotted on a log scale. Note how the arms of the crescent shape are more pronounced at lower temperatures due to the reduced width of the distribution.

3.4.1 Varying temperature

We first analyse how the initial temperature affects the properties of the plasma. Contour plots of F are shown for initial temperatures of $10^{-2} \leq \theta \leq 3$ in Fig. 3.3 at a turbulence level of $\eta = 1$. These results are for the high magnetisation case with $I_2/I_1 = 1$. Note that the scales on the axes are not the same due to the different widths of the particle distributions in momentum space. The properties of these distributions are shown in Fig. 3.4 as a function of η. The average kinetic energy is shown in Fig. 3.4a, the temperature anisotropy in Fig. 3.4b, the perpendicular and parallel temperatures in Figs. 3.4c and 3.4d, and the average perpendicular and parallel momenta in Figs. 3.4e and 3.4f. In each case the quantities are shown for initial temperatures ranging from $\theta = 10^{-3}$ to $\theta = 3$.

In each case some clear trends emerge. In the case of the kinetic energy, there is naturally no significant increase until the energy of the turbulence becomes comparable to the thermal energy of the distribution, as can be seen in Fig. 3.4a. For this reason, the lower initial temperatures show dramatic increases in temperature, while the hotter distributions have only a moderate increase. As expected, higher initial temperatures require correspondingly higher turbulence levels to undergo significant changes. Once the turbulence level does increase sufficiently, the kinetic energy increases linearly as the wave energy is transferred to the particle distribution.

The temperature anisotropy A undergoes two distinct phases of evolution, as shown in Fig. 3.4b. For lower levels of turbulence, A increases as η increases. This initial increase is well modelled by the non-relativistic perpendicular evolution result found by Wu & Yoon (2007), who found that $A \sim 1 + 4\epsilon$, where ϵ is defined in Eq. (2.8). This function is shown as the dashed maroon line for the $\theta = 10^{-3}$ case. This anisotropy results from the increase in perpendicular temperature of $\theta_\perp(\epsilon) = \theta_\perp(1 + 4\epsilon)$, which is also shown as a dashed maroon line in Fig. 3.4c for $\theta = 10^{-3}$. At moderate values of η the anisotropy reaches its maximum value before beginning to decrease again. This decrease is due to the increase in the apparent parallel temperature at this point, as can be seen in Fig. 3.4d. We note that this is not a true temperature, but is partly caused by the formation of the crescent-shaped arms of the distribution which extend to large positive parallel momentum values. However, the spread of the distribution in the parallel direction does also increase as the perpendicular temperature increases. This can be seen by the fact that the parallel diffusion term is proportional to $q_{\perp}^2$ (see the $\left(\frac{\partial F}{\partial t}\right)_{\|,2}$ term in Eq. (3.5)). The maximum temperature anisotropy possible decreases with increasing temperature, as the hotter distribution is less affected by the Alfvén waves due to its higher internal energy.

While the increase in $\langle q_{\perp} \rangle$ shown in Fig. 3.4e closely mirrors the increase in perpendicular temperature, the average parallel momentum increases linearly with time. This is due to the constant shift to higher positive parallel momenta caused by the Alfvén waves. This results in a bulk parallel momentum of $q_{\|} > 0$, as is discussed further in Chapter 4.

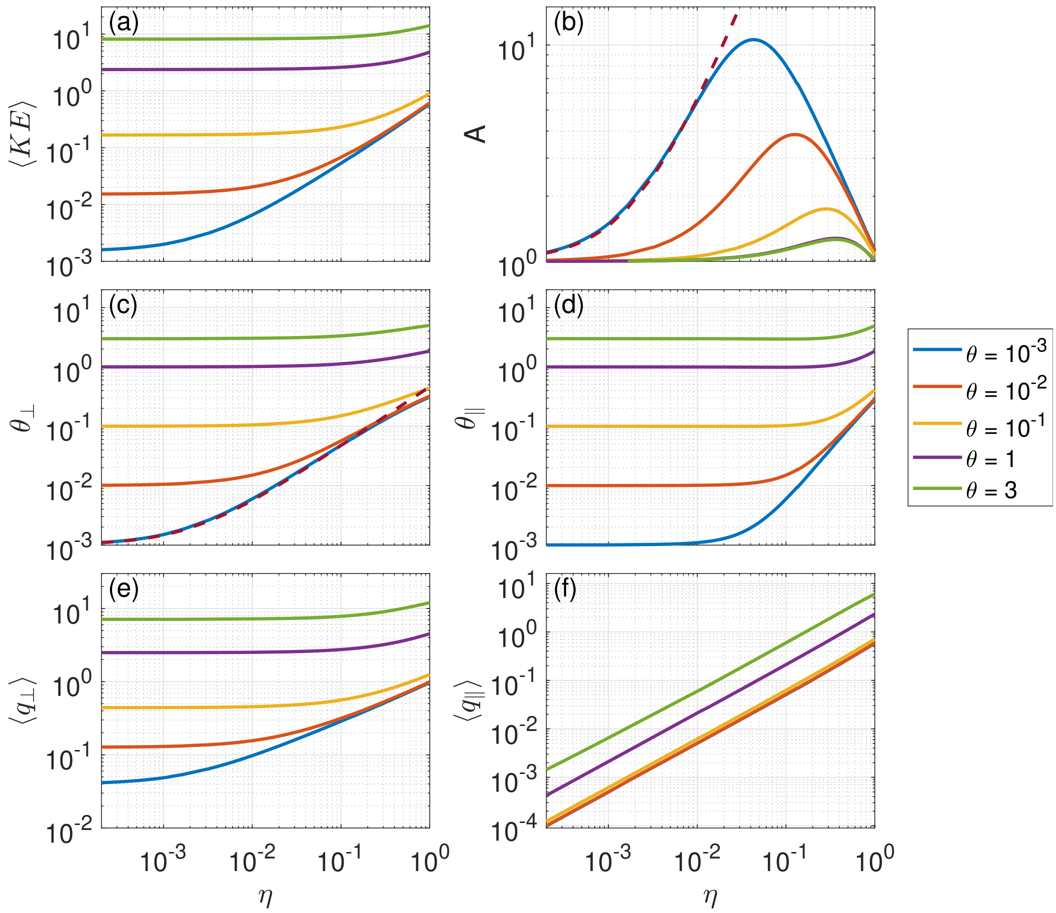

Figure 3.4: Parameters of the particle distribution in the high magnetisation case ($I_2/I_1 = 1$) as a function of the turbulence level η. **Panel (a)** shows the average kinetic energy. **Panel (b)** the temperature anisotropy A. **Panel (c)** shows the perpendicular temperature while **panel (d)** shows the parallel temperature. The average perpendicular and parallel momenta are shown in **panel (e)** and **panel (f)** respectively. In each case the quantities are shown for initial temperatures ranging from $\theta = 10^{-3}$ to $\theta = 3$, shown as different colour solid lines. The dashed maroon lines in panels (b) and (c) show the perpendicular evolution approximation from Wu & Yoon (2007) for the $\theta = 10^{-3}$ case.

3.4.2 Varying magnetisation

The other primary parameter which defines the behaviour of the particles is the magnetisation, primarily through its impact on the Alfvén velocity and the terms I_1, I_2 and I_3. The evolution of an initial Maxwell-Jüttner distribution with $\theta = 10^{-2}$ (shown in Fig. 3.5a) is shown for different magnetisations in the other panels of Fig. 3.5. Fig. 3.5b shows a contour plot for $I_2/I_1 = 1$, Fig. 3.5c shows a contour plot for $I_2/I_1 = 3$ and Fig. 3.5d shows a contour plot for $I_2/I_1 = 10$. All are presented for a turbulence level of $\eta = 1$. The impact of the magnetisation on the formation of the crescent shape is immediately clear, with the shape becoming much less pronounced as I_2/I_1 increases.

The dependence of the plasma properties on varying magnetisations is shown in Fig. 3.6 as a function of η for $1 \leq I_2/I_1 \leq 100$. All results presented are again for an initial temperature of $\theta = 10^{-2}$. The average kinetic energy is shown in Fig. 3.6a, the temperature anisotropy in Fig. 3.6b, the perpendicular and parallel temperatures in Figs. 3.6c and 3.6d, and the average perpendicular and parallel momenta in Figs. 3.6e and 3.6f. As in Figs. 3.4b and 3.4c, the non-relativistic perpendicular evolution from Wu & Yoon (2007) is shown as the dashed maroon line for the $I_2/I_1 = 1$ case.

Pronounced differences are clear across all the quantities examined. In each case, the properties of the particle distribution are disturbed more from their initial conditions in the high magnetisation scenario ($I_2/I_1 = 1$). The general behaviour is the same as the magnetisation decreases, with the kinetic energy, temperature anisotropy, temperatures and average momenta all increasing with η. However, the rate at which these quantities change decreases as the magnetisation increases. Indeed, for $I_2/I_1 \gtrsim 10 - 30$, there is very little change in the temperature or kinetic energy, even for high turbulence levels. There is still, however, an increase in the parallel bulk velocity, as can be seen in Fig. 3.5d. Although less pronounced evolution is expected at lower magnetisation due to the relatively larger plasma β, the more detailed analysis presented in Chapter 4 below shows that this is not the sole cause of the observed behaviour.

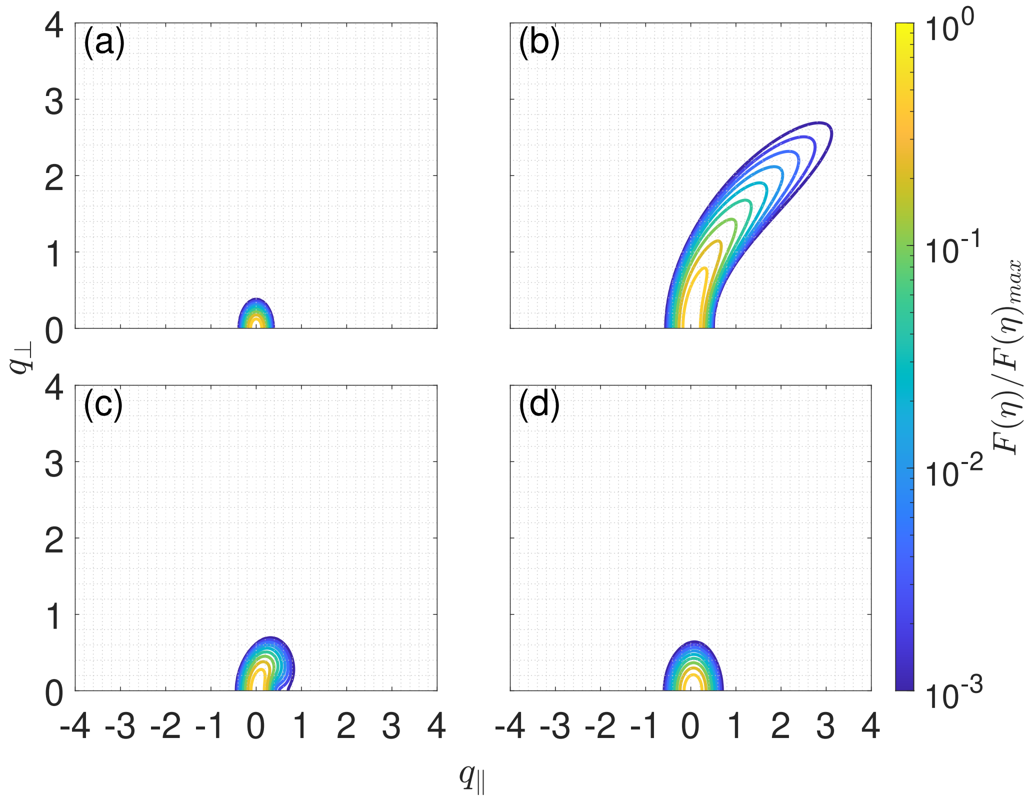

Figure 3.5: Contour plots of an initial Maxwell-Jüttner distribution. All plots have an initial temperature of $\theta = 10^{-2}$. **Panel (a)** shows the initial distribution ($\eta = 0$). **Panel (b)** shows the distribution for $I_2/I_1 = 1$ at $\eta = 1$. **Panel (c)** shows the distribution for $I_2/I_1 = 3$ at $\eta = 1$ while **panel (d)** presents the distribution for $I_2/I_1 = 10$ at $\eta = 1$. The values are normalised to the maximum value of F and are plotted on a log scale. As I_2/I_1 increases, the distribution undergoes smaller changes.

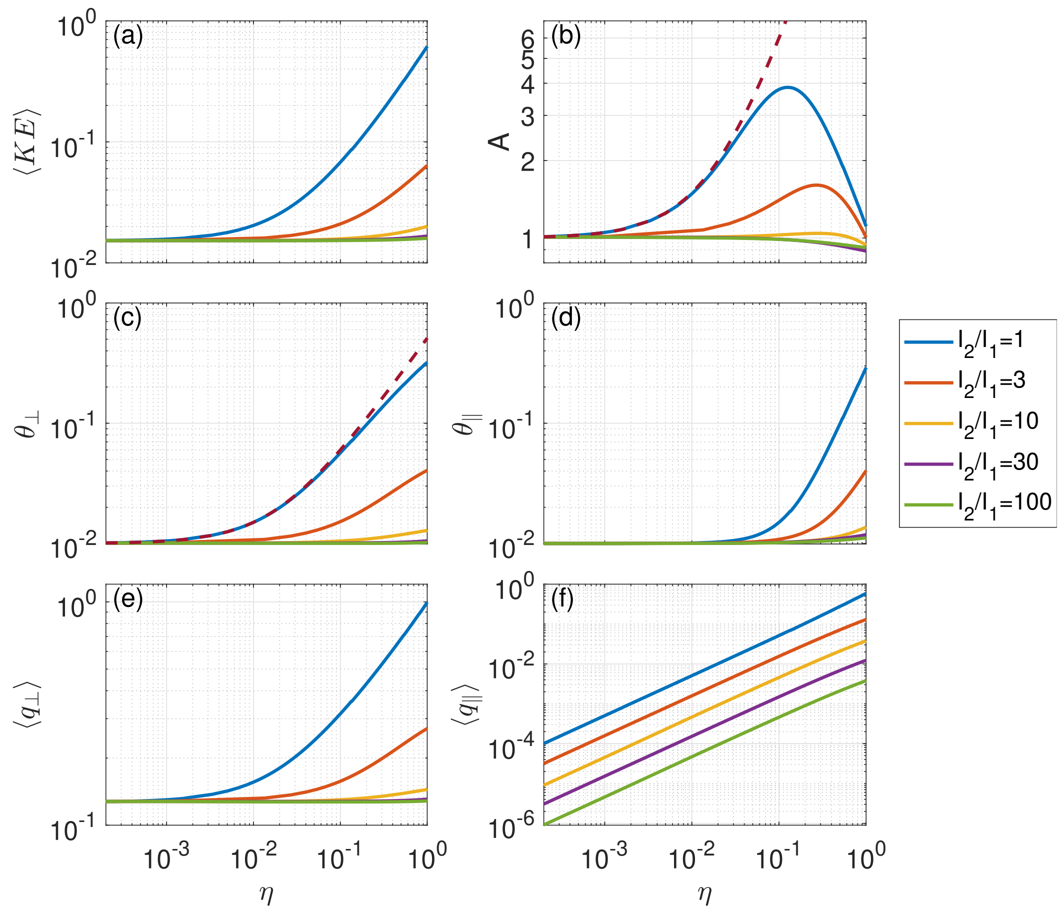

Figure 3.6: Parameters of the particle distribution for varying values of I_2/I_1 as a function of the turbulence level η. **Panel (a)** shows the average kinetic energy. **Panel (b)** the temperature anisotropy A. **Panel (c)** shows the perpendicular temperature while **panel (d)** shows the parallel temperature. The average perpendicular and parallel momenta are shown in **panel (e)** and **panel (f)** respectively. In each case the quantities are shown for an initial temperature of $\theta = 10^{-2}$, with different I_2/I_1 values shown by different colour solid lines. The dashed maroon lines in panels (b) and (c) show the perpendicular evolution approximation from Wu & Yoon (2007) for the $\theta = 10^{-3}$ case.

3.5 Results: Non-Maxwellian distributions

3.5.1 Initial temperature anisotropy

Further insight into the evolution of the plasma can be gained from examining the effect of an initial temperature anisotropy. Such distributions are both common in nature (e.g Gary et al., 2001; Gary, 1993; Verscharen et al., 2019) and can be used to further our understanding of the evolution of an initially isotropic distribution. To examine the situation, we begin from an initial anisotropic Maxwell-Jüttner distribution of the form (Baumjohann & Treumann, 2023)

$$F(q_\perp, q_\parallel) = C \exp\left(-\theta_\perp^{-1}\sqrt{1 + q_\perp^2 + A_0 q_\parallel^2}\right), \tag{3.19}$$

where C is the normalisation factor and A_0 is the initial anisotropy. We examine a range of anisotropies $\frac{1}{5} \leq A_0 = \frac{\theta_\perp}{\theta_\parallel} \leq 5$ in the high magnetisation regime $(I_2/I_1 = 1)$. In each case, the initial perpendicular temperature is $\theta_\perp = 10^{-2}$. The properties of these distributions are shown in Fig. 3.7 as a function of η. The average kinetic energy is shown in Fig. 3.7a, the temperature anisotropy in Fig. 3.7b, the perpendicular and parallel temperatures in Figs. 3.7c and 3.7d, and the average perpendicular and parallel momenta in Figs. 3.7e and 3.7f.

The general trends are the same as in the isotropic case, with all quantities initially increasing as η increases. The presence of the temperature anisotropy has no impact on the perpendicular temperature or average momenta, as can be seen in Figs. 3.7c, 3.7e and 3.7f. However, the parallel temperature increases more rapidly for lower initial values of $\theta_\parallel$, with the values converging to similar values for all A_0 at high turbulence levels. This can be explained by examining Eq. (3.5). The parallel diffusion term, $\left(\frac{\partial F}{\partial t}\right)_{\parallel,2}$, depends on the square of the perpendicular momentum, as discussed in Sec. 3.4.1. Thus, for larger perpendicular momenta, diffusion in the parallel direction proceeds more rapidly. In contrast, the perpendicular diffusion is dominated by the

I_3 term (see the $\left(\frac{\partial F}{\partial t}\right)_{\perp,2}$ term in Eq. (3.5)) in the highly magnetised regime where $I_1 = I_2 = I_3$. This has no dependence on the parallel momentum, and as such is not affected by the temperature anisotropy.

Furthermore, even at small $q_\perp$, the presence of an anisotropy results in the spread of the particle distribution in both the positive and negative parallel directions. This can be seen from the expression for $\frac{\partial F(q_\perp=0)}{\partial t}$ which has been taken from Eq. (3.5):

$$\begin{aligned}\frac{\partial F(q_\perp = 0)}{\partial t} &= -C\frac{\exp\left(-\theta_\perp^{-1}\sqrt{1+Aq_\parallel^2}\right)}{\theta_\perp(1+q_\parallel^2)^{3/2}\sqrt{1+Aq_\parallel^2}} \\ &\times\Big(-(A-1)I_2q_\parallel^2\sqrt{1+q_\parallel^2}+(A-2)I_1q_\parallel(1+q_\parallel^2) \\ &+I_3(1+q_\parallel^2)^{3/2}\Big),\end{aligned} \tag{3.20}$$

where C contains all the constants omitted for clarity. Setting $\frac{\partial F(q_\perp=0)}{\partial t} = 0$ results in the expression

$$-(A-1)I_2q_\parallel^2\sqrt{1+q_\parallel^2}+(A-2)I_1q_\parallel(1+q_\parallel^2)+I_3(1+q_\parallel^2)^{3/2} = 0. \tag{3.21}$$

The solution for $q_\parallel < 0$ in the linear regime where $I_1 = \frac{v_{A,rel}}{c}I_2 = \frac{c}{v_{A,rel}}I_3$ is then given by

$$q_\parallel = -\frac{1}{\sqrt{(I_2/I_1)^2(A-1)^2-1}}. \tag{3.22}$$

A positive $\frac{\partial F}{\partial t}$ in the $q_\parallel < 0$ region is therefore only possible when $I_2/I_1 > 1/|A-1|$, which requires a temperature anisotropy. When the temperature anisotropy is large, the distribution begins to spread in the parallel direction resulting in an equalisation of the temperatures even for small perpendicular momenta. The effect is more pronounced the further A is from unity, which results in the properties of the plasma converging for large values of η, as can be seen in Fig. 3.7.

This convergence can also be seen in the contour plots shown in Fig. 3.8. Here, Fig. 3.8a and 3.8b display contour plots for $A_0 = 2$ at turbulence levels of $\eta = 0$ and $\eta = 1$ respectively, while Figs. 3.8a and 3.8b show the same for $A_0 = 0.5$. The general shape of the distribution is the same in both $\eta = 1$ cases, with the primary difference being the width of the distributions in the parallel direction. This difference in width is present despite the value of $\theta_{\|}$ being approximately equal for both distributions, as can be seen in Fig. 3.7d. This emphasises the point made in Sec. 3.4.1 that the value of $\theta_{\|}$ is not a true temperature, but rather is largely due to the positive parallel momentum of the arms of the crescent as η approaches unity.

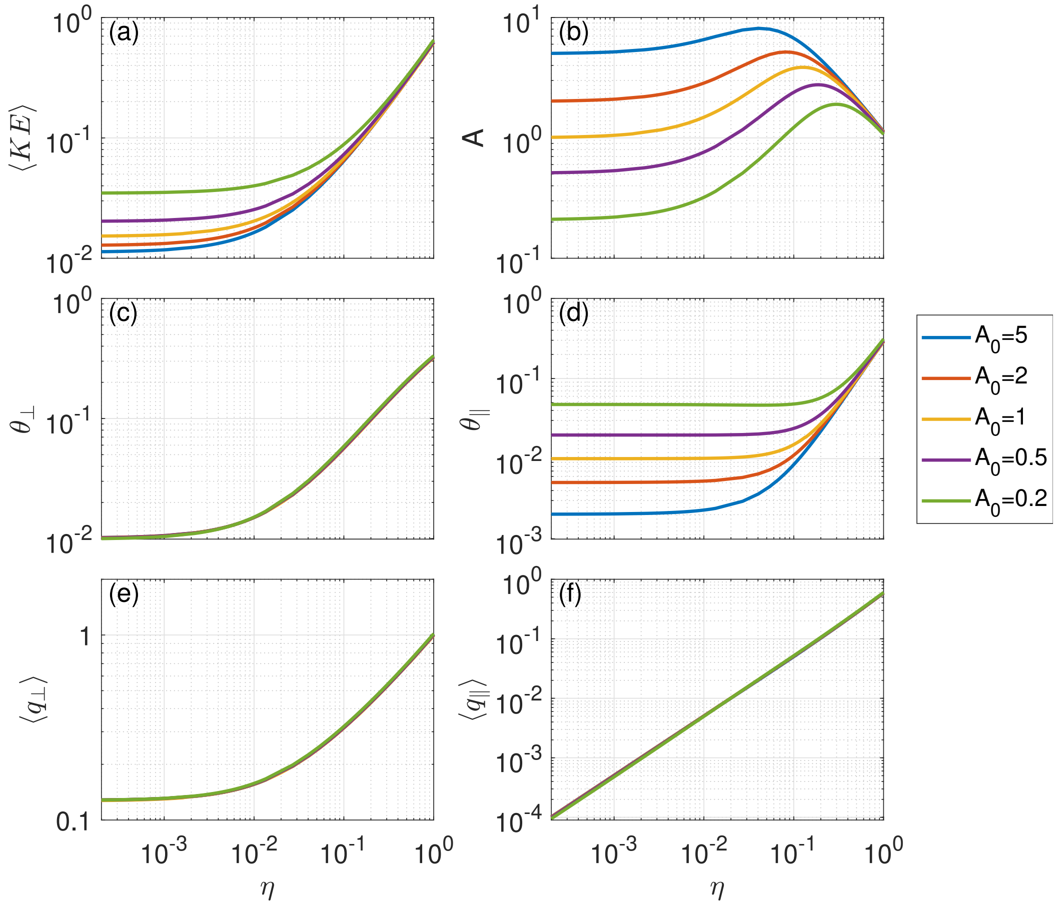

Figure 3.7: Parameters of an anisotropic distribution as a function of the turbulence level η for varying initial A_0 and I_2/I_1. The initial distribution is given by Eq. (3.19). **Panel (a)** shows the average kinetic energy. **Panel (b)** the temperature anisotropy A. **Panel (c)** shows the perpendicular temperature while **panel (d)** shows the parallel temperature. The absolute value of the average perpendicular and parallel momenta are shown in **panel (e)** and **panel (f)** respectively. In panels (c), (e) and (f) all values of A_0 produce very similar results.

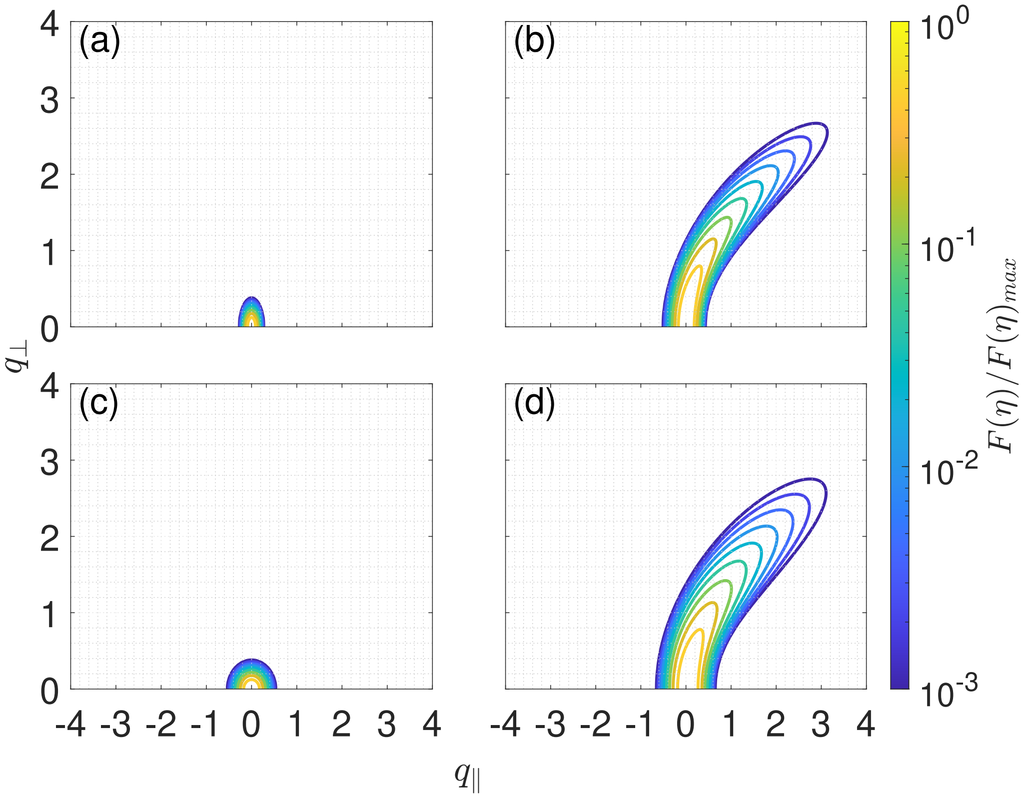

Figure 3.8: Contour plots of the anisotropic distribution given by Eq. (3.19). All plots are for $I_2/I_1 = 1$. **Panel (a)** shows the initial distribution ($\eta = 0$) for $A_0 = 2$ while **panel (b)** shows the distribution for $A_0 = 2$ at $\eta = 1$. **Panel (c)** shows the initial distribution ($\eta = 0$) for $A_0 = 0.5$ and **panel (d)** shows the distribution for $A_0 = 0.5$ at $\eta = 1$. The values are normalised to the maximum value of F and are plotted on a log scale. The width of the distribution in the parallel direction is largely preserved throughout the evolution.

3.5.2 Beam distributions

Distributions containing beams are common across astrophysical systems (e.g Bret et al., 2010; Verscharen et al., 2019). For this reason, in this section we deal with a parallel beam distribution of the form

$$F(q_\perp, q_\parallel) = C \exp\left(-\theta^{-1}\gamma_b\left[\sqrt{1+q_\perp^2+q_\parallel^2} - \beta_b q_\parallel\right]\right) \tag{3.23}$$

where β_b is the beam velocity in the parallel direction and $\gamma_b = (1-\beta_b)^{-1/2}$. We assume that this beam is present in addition to a thermal component with no bulk velocity which dominates the dispersion relation of the Alfvén waves, so that the formalism described in Sec. 3.2.2 can be used throughout.

The properties of the beam distributions are shown in Fig. 3.9 as a function of η for varying I_2/I_1 and β_b. As in the previous sections, the average kinetic energy is shown in Fig. 3.9a, the temperature anisotropy in Fig. 3.9b, the perpendicular and parallel temperatures in Figs. 3.9c and 3.9d, and the average perpendicular and parallel momenta in Figs. 3.9e and 3.9f. In each case the quantities are shown for an initial temperature of $\theta = 10^{-2}$. The kinetic energy and temperatures are calculated in the rest frame of the beam plasma, while the average momenta are calculated in the lab frame. One of the parameter sets is for a beam with a negative beam velocity (i.e. travelling in the opposite direction to the Alfvén waves) of $\beta_b = -0.9$ and is shown in green. For this reason the average parallel momentum in Fig. 3.9f is shown as an absolute value.

The results for this scenario show some interesting differences in comparison to the previous models with no bulk velocity. The increase in energy and temperature is actually larger at lower magnetisations (larger I_2/I_1), the opposite result to the previous cases. At lower magnetisations, the wave actually has a lower phase velocity than the velocity of the particles, resulting in the particles undergoing a reduction in parallel momentum. The effect of pitch-angle scattering is particularly pronounced in this case, with large increases in perpendicular temperature and momentum necessary to conserve the total energy even for quite low turbulence levels. The changes are most extreme for the negative beam velocity case due to the large difference between the wave velocity and β_b.

The strong distortion of the initial particle distribution can be clearly seen in Fig. 3.10. Here, Fig. 3.10a shows the initial distribution for $\beta_b = 0.9$, while Figs. 3.10b, 3.10c and 3.10d show the distribution at $\eta = 1$ for $I_2/I_1 = 1$, $I_2/I_1 = 3$ and $I_2/I_1 = 10$ respectively. For $I_2/I_1 = 1$, $\beta_A > \beta_b$ and particles are scattered to larger values of $q_\parallel$, as in the case with no beam velocity. However, the results shown in Figs. 3.10c and 3.10d demonstrate the major changes that occur when $\beta_A < \beta_b$. As in the previous sections, the large values of $\theta_\parallel$ shown in Fig. 3.9d are not true temperatures but are due to the pitch-angle scattering.

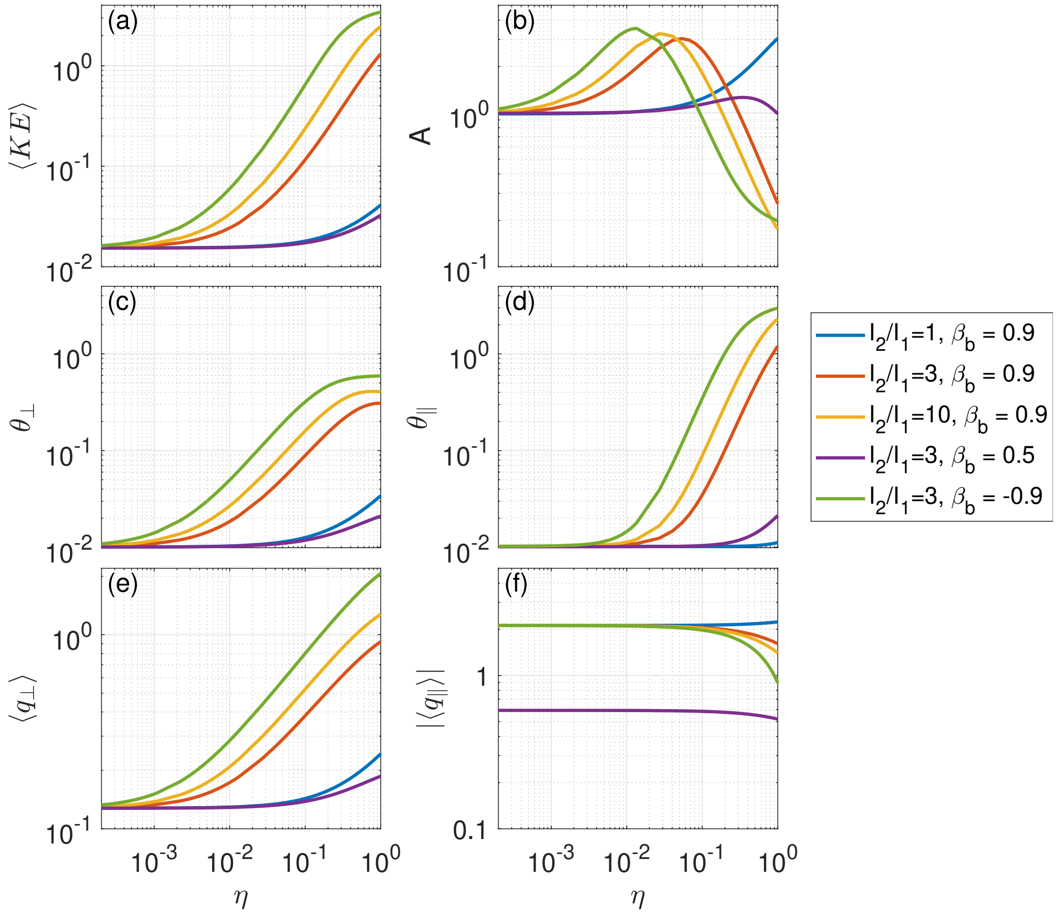

Figure 3.9: Parameters of a beam distribution as a function of the turbulence level η for varying beam velocities β_b and I_2/I_1. **Panel (a)** shows the average kinetic energy. **Panel (b)** the temperature anisotropy A. **Panel (c)** shows the perpendicular temperature while **panel (d)** shows the parallel temperature. The absolute value of the average perpendicular and parallel momenta are shown in **panel (e)** and **panel (f)** respectively. Note that the average parallel momentum is negative for the $I_2/I_1 = 3, \beta_b = -0.9$ case. All quantities are measured in the beam plasma frame except for the average momenta.

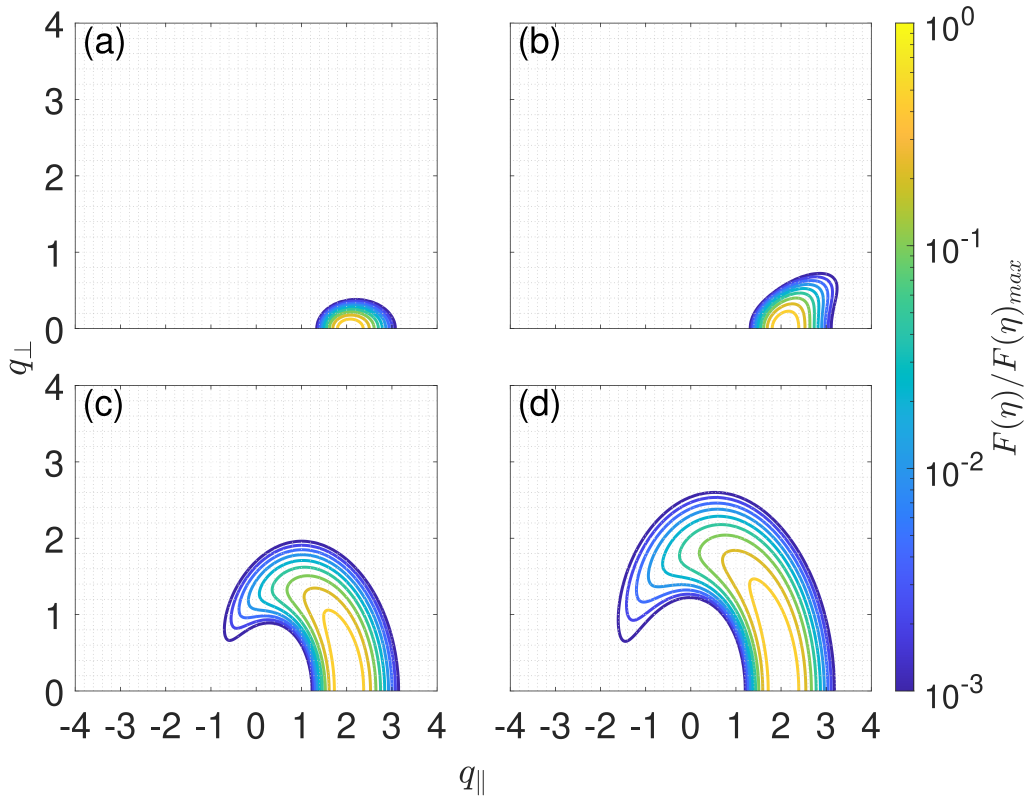

Figure 3.10: Contour plots of the beam distribution function given by Eq. (3.23). All plots are for $\beta_b = 0.9$. **Panel (a)** shows the initial distribution ($\eta = 0$); **panel (b)** shows the distribution for $I_2/I_1 = 1$ at $\eta = 1$; **panel (c)** shows the distribution for $I_2/I_1 = 3$ at $\eta = 1$ and **panel (d)** presents distribution for $I_2/I_1 = 10$ at $\eta = 1$. The values are normalised to the maximum value of F and are plotted on a log scale. Note that in this case the distortion from the initial distribution is greatest for larger values of I_2/I_1.

3.6 Discussion and conclusions

The results presented above indicate that the non-resonant interaction between Alfvén waves and relativistically hot plasmas is capable of significantly changing the properties of said plasma. We show that the interaction is largely independent of the spectrum of the Alfvén waves and primarily depends on the turbulence level. The turbulence imparts energy to the plasma, resulting in an increase in kinetic energy, with the gain in momentum primarily in the perpendicular direction due to pitch-angle scattering. The waves also impart a bulk velocity in the positive parallel direction (i.e. the direction of the waves' propagation). The effect on the plasma is most pronounced at lower temperatures and higher magnetisations, as in these cases the thermal energy of the plasma is relatively lower compared to the wave energy.

The imposition of an initial temperature anisotropy does not significantly alter the results for large turbulence levels. While at lower values of η the properties of the plasma differ greatly due to the initial anisotropy, as the turbulence level increases the particle distribution asymptotes to similar temperatures and kinetic energy. Therefore, a standard isotropic Maxwell-Jüttner distribution provides an adequate approximation for anisotropic distributions in terms of evaluating their response to non-resonant interactions with Alfvén waves. The presence of a temperature anisotropy itself does not guarantee SME, as $A \neq 1$ does not necessarily imply the formation of the required population inversion with a positive perpendicular gradient. For instance, a simple bi-Maxwellian has $\frac{\partial F}{\partial q_\perp} \leq 0$ at all points in momentum space. For this reason, the formation of the crescent shape is crucial for SME, as is discussed in the following chapter. However, the temperature anisotropy formed as a result of the non-resonant interaction is indeed susceptible to other plasma instabilities such as the mirror and firehose instabilities, which are discussed in more detail in Sec. 4.4.

In contrast, the presence of a particle beam results in quite different results. The outcome of the non-resonant interaction in this case depends strongly on the relative velocity of the Alfvén waves and the beam itself. For $v_A > v_b$, the particles are scattered to higher parallel momenta, as in the $v_b = 0$ case. However, if $v_A < v_b$, which is the case for lower magnetisations or higher beam velocities, the particles are naturally scattered to lower parallel momenta. This can result in the formation of strong crescent-shaped distributions even at lower magnetisations, a significant difference to the case with no bulk velocity. As beams are ubiquitous in many different astrophysical scenarios from solar flares (e.g Verscharen et al., 2019) to gamma-ray bursts (GRBs) (e.g Bret et al., 2010), these results may have broad applications. We note that the beam plasma is more susceptible to resonant effects such as Landau damping for wave modes with non-zero parallel electric fields $E_{\|}$, as the condition $\omega = k_{\|} v_{\|}$ can be fulfilled, depending on the magnetisation and beam velocity.

Throughout this chapter we have established and quantified the evolution of various plasma properties as a result of the non-resonant interactions with Alfvén waves. However, in order to evaluate the utility of this mechanism in the case of SME and FRBs, further analysis is necessary to examine the formation of the crescent shape and whether the resulting population inversion is capable of supporting SME. These matters are discussed in Chapters 4 and 5 below.

Chapter 4

The formation of a population inversion through non-resonant interactions

4.1 Introduction

The analysis in Chapter 3 demonstrates that the non-resonant interaction between Alfvén waves and a relativistic plasma can significantly alter the properties of the plasma. The interaction results in enhanced temperature in both the perpendicular and parallel directions, as well as introducing a bulk velocity in the positive parallel direction. Furthermore, at relatively high turbulence levels of $\eta \gtrsim 0.1$ a crescent-shaped distribution is formed, even at relativistic temperatures. This distribution contains the population inversion required for SME, as discussed in Chapters 1 and 2. In this chapter, we analyse the formation of this crescent shape, and how it may be applied to FRBs. We do this by exploring the parameter space in both magnetisation and temperature and by quantifying the behaviour in different physical regimes.

This chapter is structured as follows. Sec. 4.2 presents a detailed analysis of the quasilinear kinetic equation and how different terms contribute to the formation of the crescent shape. Semi-analytical results for the behaviour of individual terms are derived in Appendix B. In Sec. 4.3 we present the results for both the energy fraction contained in the population inversion and the relevant formation time-scales. These results are discussed and compared to the physical conditions necessary to produce FRBs in Sec. 4.4, and the results of the chapter are summarised in the conclusion in Sec. 4.5.

4.2 Quantifying the crescent-shaped distribution

Although the quantities measured in Chapter 3 are important for understanding the general properties of the distorted particle distribution, further analysis is necessary to examine the formation of the crescent-shaped distribution. Therefore, after solving Eq. (3.5) numerically using the methods described in Chapter 3, we calculate the fraction of energy contained in the crescent-shaped part of the distribution function, f_{inv}, as well as the turbulence level needed to reach this value. To obtain f_{inv} we take the distribution obtained through solving Eq. (3.5) and calculate its total kinetic energy, $E_{tot} = \int d\mathbf{p}(\gamma(\mathbf{p}) - 1)F(\mathbf{p})$. We compare this value to the total kinetic energy of another distribution with the same widths as the actual distribution in both the parallel and perpendicular directions. However, this comparison distribution is centred at the coordinates of the maximum value of the actual distribution for all values of $q_\perp$. The resulting distribution is therefore similar to a bi-Maxwellian distribution with non-constant widths as the contributions from the crescent-shaped arms, which are centred at increasingly large values of $q_\parallel > 0$ as $q_\perp$ increases, have been removed. We denote the total kinetic energy of this modified distribution as E_{bi}. We then define f_{inv} by comparing the two energy values: $f_{inv} = (E_{tot} - E_{bi})/E_{tot}$. This quantity is therefore the amount of excess energy contained in the crescent part of the deformed distribution only, and does not include any contributions from changes in energy such as symmetrical increase in the perpendicular or parallel temperature.

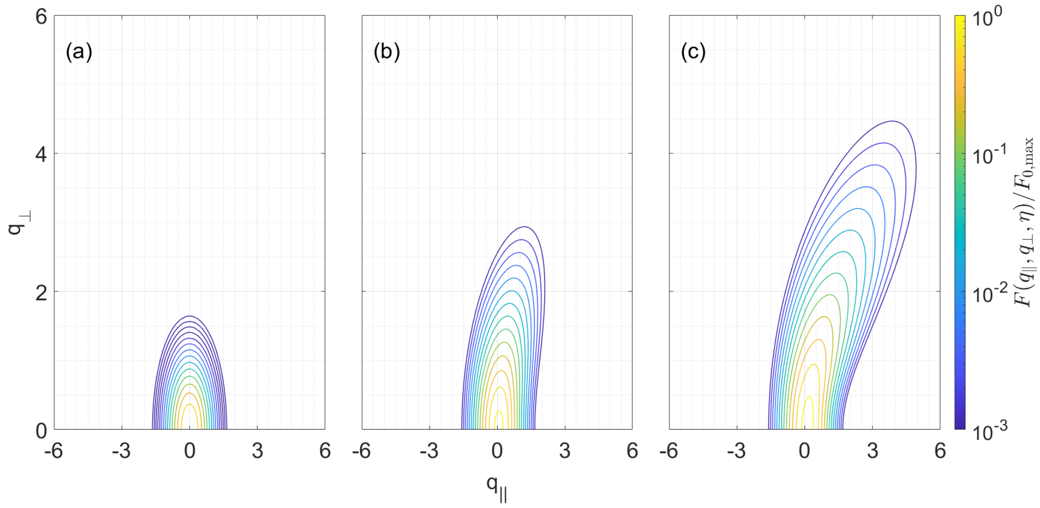

Figure 4.1: Contour plots of the distribution function F for an initial Maxwell-Jüttner distribution in the high magnetisation regime with $\theta = 10^{-1}$ and $I_2/I_1 = 1$. **Panel (a)** shows the initial distribution function F_0; **panel (b)** shows F at $\eta = 0.3$ and **panel (c)** shows the distribution at $\eta = 1$. The progression from the initial to the final time step shows the development of the arms of the crescent-shaped population inversion. The values are normalised to the maximum initial value of $F_0(\theta = 0.1)$ and are plotted on a log scale.

As shown in Chapter 5, the presence of a significant f_{inv} does not guarantee efficient maser emission, as the process also depends on the gradients of the distribution and where the population inversion overlaps with the resonance ellipses. However, it serves as a useful proxy for the level of distortion induced by the non-resonant interactions.

4.2.1 Detailed analysis of the non-resonant interaction at high magnetisations

For consistency across the following analysis, we will focus on an initial Maxwell-Jüttner distribution with an initial temperature of $\theta = 10^{-1}$ and $I_2/I_1 = 1$, equivalent to $\bar{\sigma} \gtrsim 10^2$. The evolution of such a distribution is shown in Fig. 4.1, which presents contour plots at $\eta = 0$, $\eta = 0.3$ and $\eta = 1$.

The formation of the crescent shape is visible through the extension of the initial distribution to larger values of $q_\perp$ for $q_\parallel > 0$, with the arms of the crescent expanding as the distribution continues to evolve.

A plot of $\frac{\partial F_0}{\partial t}$ is shown in Fig. 4.2 for an initial Maxwell-Jüttner distribution with temperature $\theta = 0.1$ and $I_2/I_1 = 1$, the same parameters as displayed in Fig. 4.1. As shown in Fig. 4.2, the primary outcome of the wave-particle interaction is to transfer particles from regions of low perpendicular momentum, $q_\perp \lesssim 0.5$, and negative parallel momentum, $q_\parallel < 0$ (the blue region in Fig. 4.2), to higher perpendicular momenta (in both the positive and negative directions) through pitch-angle diffusion. The resulting regions of positive $\frac{\partial F}{\partial t}$ are primarily in the $q_\parallel > 0$ half of the momentum space. The interaction also results in a bulk momentum in the parallel direction, as can be seen in Fig. 4.1c, where the peak of the distribution is located at $q_\parallel \sim 1$.

To determine how the non-resonant interaction results in the overall evolution shown in Fig. 4.2, it is necessary to compare the terms in Eq. (3.5) with each other. Examining the contributions to $\frac{\partial F_0}{\partial t}$ from each individual term in Fig. 4.3 allows us to determine which terms are most important to the formation of the population inversion. All five terms are presented in Fig. 4.3a to 4.3e, showing $\left(\frac{\partial F_0}{\partial t}\right)_{\parallel,1}$, $\left(\frac{\partial F_0}{\partial t}\right)_{\perp,1}$, $\left(\frac{\partial F_0}{\partial t}\right)_{\parallel,2}$, $\left(\frac{\partial F_0}{\partial t}\right)_{\perp,2}$ and $\left(\frac{\partial F_0}{\partial t}\right)_{mix}$ respectively for the same set of parameters as presented in Fig. 4.2. We note that $\frac{\partial F_0}{\partial t}$ is asymmetric in the parallel direction, which is important to the formation of the crescent shape seen in Fig. 4.1. Indeed, several of the terms in Eq. (3.5) are asymmetric about $q_\parallel = 0$. Both perpendicular terms have a maximum magnitude offset from $q_\parallel = 0$, as can be seen in Fig. 4.3b and 4.3d. This offset is due to the I_3 terms in both coefficients, shown on lines 2 and 4 of Eq. (3.5).

However, the only two terms where the maximum value of $\frac{\partial F_0}{\partial t}$ is centred at $q_\perp > 0$ and $q_\parallel > 0$ are the parallel diffusion term $\left(\frac{\partial F_0}{\partial t}\right)_{\parallel,2}$, displayed in Fig. 4.3c, and the mixed term $\left(\frac{\partial F_0}{\partial t}\right)_{mix}$, shown in Fig. 4.3e. The parallel diffusion term is considerably lower in magnitude than the mixed term, and furthermore is symmetric in the parallel direction. As none of the other terms provide the necessary positive regions of $\frac{\partial F_0}{\partial t}$ at $q_\perp > 0$ and $q_\parallel > 0$, this leads

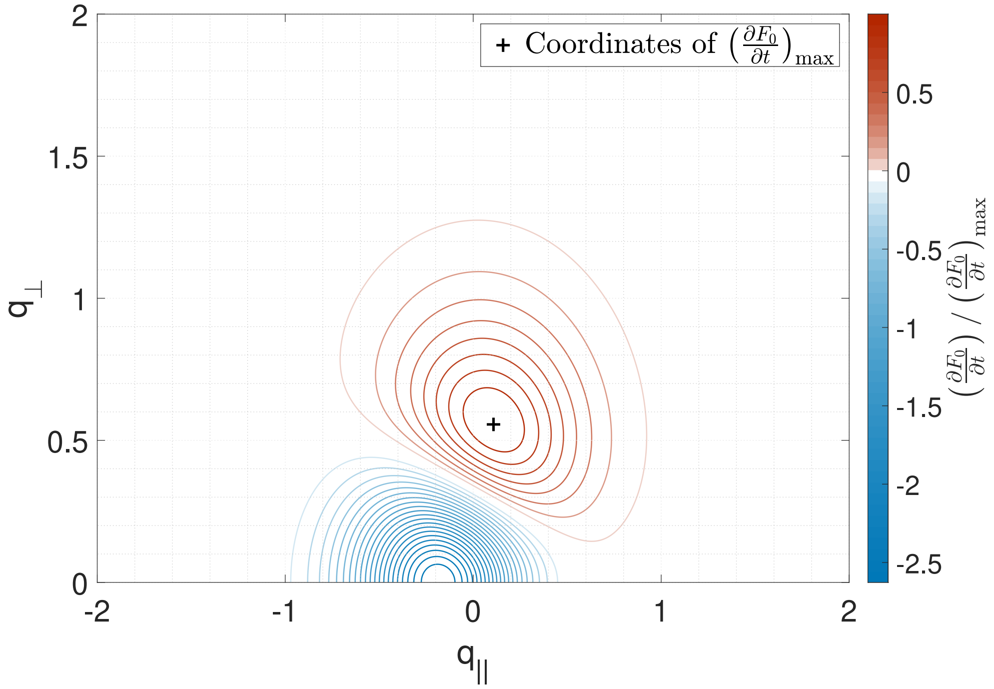

Figure 4.2: Contour plot of $\frac{\partial F_0}{\partial t}$ for a Maxwell-Jüttner distribution in the high magnetisation regime for $\theta = 0.1$ and $I_2/I_1 = 1$. The values are normalised to the maximum value of $\frac{\partial F_0}{\partial t}$. The coordinates of the maximum value of $\frac{\partial F_0}{\partial t}$ are marked by the black crosses. The positive contribution of this term is strongest off-axis in the $q_{||} > 0$ region, and will lead to an evolved distribution as in Fig. 4.1b.

us to conclude that $\left(\frac{\partial F_0}{\partial t}\right)_{mix}$ is the crucial term that determines the level of population inversion that is formed. This is the case even though it is not the largest term for any set of parameters. The overall form of $\frac{\partial F_0}{\partial t}$ in Fig. 4.2 is dominated by the perpendicular terms, but the contribution of the mixed term provides the element that results in the maximum value of $\frac{\partial F_0}{\partial t}$ being centred at a value of $q_{||} > 0$ rather than $q_{||} = 0$. At this high magnetisation, the impact of the substantial region of positive $\frac{\partial F_0}{\partial t}$ from the parallel advection term in Fig. 4.3a is cancelled out by the equivalent negative $\frac{\partial F_0}{\partial t}$ in the same region from both perpendicular terms and the mixed term.

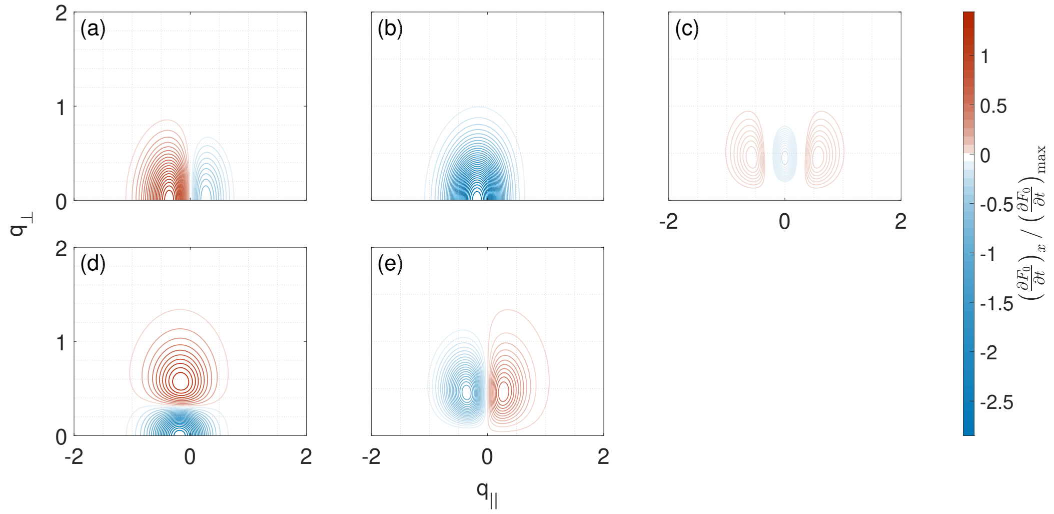

Figure 4.3: Contour plots of each individual term $\left(\frac{\partial F_0}{\partial t}\right)_x$ from Eq. (3.5). Each $\left(\frac{\partial F_0}{\partial t}\right)_x$ is calculated for a Maxwell-Jüttner distribution in the high magnetisation regime with $\theta = 0.1$ and $I_2/I_1 = 1$. The values are normalised to the maximum value of the overall $\frac{\partial F_0}{\partial t}$. **Panel (a)** shows the parallel advection term $\left(\frac{\partial F_0}{\partial t}\right)_{\parallel,1}$ The contribution from this term consists of a strong $\frac{\partial F}{\partial t} > 0$ for $q_\parallel < 0$ and a weaker $\frac{\partial F}{\partial t} < 0$ for $q_\parallel > 0$. **Panel (b)** shows the perpendicular advection term $\left(\frac{\partial F_0}{\partial t}\right)_{\perp,1}$. This term has an entirely negative contribution to the change in the distribution for these parameters and thus does not contribute to the formation of the crescent-shaped inversion. **Panel (c)** shows the parallel diffusion term $\left(\frac{\partial F_0}{\partial t}\right)_{\parallel,2}$. The maximum positive contribution for this term is strongest for $q_\perp > 0$, as in the overall $\frac{\partial F_0}{\partial t}$. However, this term is symmetric in both directions and is also relatively weak compared to the other terms in Eq. (3.5). **Panel (d)** shows the perpendicular diffusion term $\left(\frac{\partial F_0}{\partial t}\right)_{\perp,2}$. This term acts to symmetrically diffuse the particles in the perpendicular direction. Note the similarity to $\frac{\partial F_0}{\partial t}$ in Fig. 4.2, except for the location of the main regions where $\frac{\partial F_0}{\partial t} > 0$. Finally, **Panel (e)** shows the mixed term $\left(\frac{\partial F_0}{\partial t}\right)_{mix}$. The maximum positive contribution for this term is strongest for $q_\perp > 0$ and $q_\parallel > 0$, as in the overall $\frac{\partial F_0}{\partial t}$. This term is also considerably stronger than $\left(\frac{\partial F_0}{\partial t}\right)_{\parallel,2}$, which has a similar form in the $q_\parallel > 0$ part of the momentum space.

4.2.2 Examining the magnetisation and temperature dependence

To obtain an efficient population inversion with a high value of f_{inv}, one requires an evolution of the particle distribution in both the parallel and perpendicular directions. The form of $\frac{\partial F_0}{\partial t}$ (i.e. the general regions in momentum space where the change in the distribution function is positive or negative) is strongly dependent on the magnetisation. This can be seen in the progression of Figs. 4.2, 4.4a, 4.4b, 4.4c and 4.4d which show $\frac{\partial F_0}{\partial t}$ for $I_2/I_1 = 1$, $I_2/I_1 = 2$, $I_2/I_1 = 3$, $I_2/I_1 = 10$ and $I_2/I_1 = 30$ respectively. The temperature in each case is $\theta = 10^{-1}$. The black crosses in each figure show the coordinates of the maximum value $\left(\frac{\partial F_0}{\partial t}\right)_{\max}$. As the magnetisation decreases and I_2/I_1 increases, the main positive regions of $\frac{\partial F_0}{\partial t}$ move from being predominantly in the perpendicular direction to the positive parallel direction. This evolution can be quantified by the coordinates of $\left(\frac{\partial F_0}{\partial t}\right)_{\max}$, denoted as $q_{\parallel,\max}$ and $q_{\perp,\max}$. The angle this point makes with the $q_\parallel$ axis is defined as $\alpha = \tan^{-1}\left(\frac{q_{\perp,\max}}{q_{\parallel,\max}}\right)$. This angle is presented in Fig. 4.5 as a function of the magnetisation for a range of temperatures.

The angle α provides a description of the general form of $\frac{\partial F_0}{\partial t}$. The maximal value of the population inversion occurs for intermediate values of $0 < \alpha < \pi/2$ where a clear crescent shape can form. However, some inversion will occur even for extreme values of $\alpha = 0, \pi/2$, due to the contribution from the mixed term. As discussed in Sec. 4.2.1, this provides the crucial positive regions of $\frac{\partial F}{\partial t}$ for $q_\perp > 0$ and $q_\parallel > 0$. The importance of $\left(\frac{\partial F_0}{\partial t}\right)_{mix}$ for different parameters is further discussed in Sec. 4.2.3 below.

Fig. 4.5 shows the evolution of α for different particle temperatures. While the general form of $\frac{\partial F_0}{\partial t}$ is qualitatively the same for different temperatures, the precise location of the positive and negative regions is temperature dependent. As can be seen, α increases towards $\frac{\pi}{2}$ as the temperature decreases, implying that the distribution function changes predominantly in the perpendicular direction, as described in previous works (e.g. Wu & Yoon, 2007; Yoon

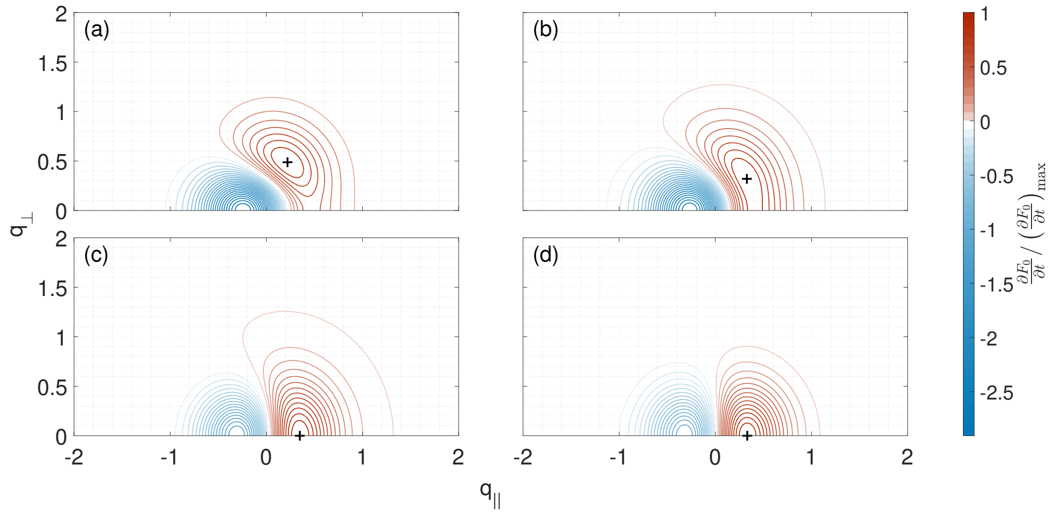

Figure 4.4: Contour plots of $\frac{\partial F_0}{\partial t}$ for Maxwell-Jüttner distributions with $\theta = 0.1$. **Panel (a)** shows $\frac{\partial F_0}{\partial t}$ for $I_2/I_1 = 2$, **panel (b)** shows $\frac{\partial F_0}{\partial t}$ for $I_2/I_1 = 3$, **panel (c)** shows $\frac{\partial F_0}{\partial t}$ for $I_2/I_1 = 10$ and **panel (d)** shows $\frac{\partial F_0}{\partial t}$ for $I_2/I_1 = 30$. In each case the values are normalised to the maximum value of $\frac{\partial F_0}{\partial t}$. The coordinates of the maximum value of $\frac{\partial F_0}{\partial t}$ are marked by the black crosses. The decrease in α with increasing I_2/I_1 (equivalent to decreasing magnetisation) is visible in the progression from panel (a) to panel (c) and (d), with $\alpha = 0$ for $I_2/I_1 = 10$ and $I_2/I_1 = 30$.

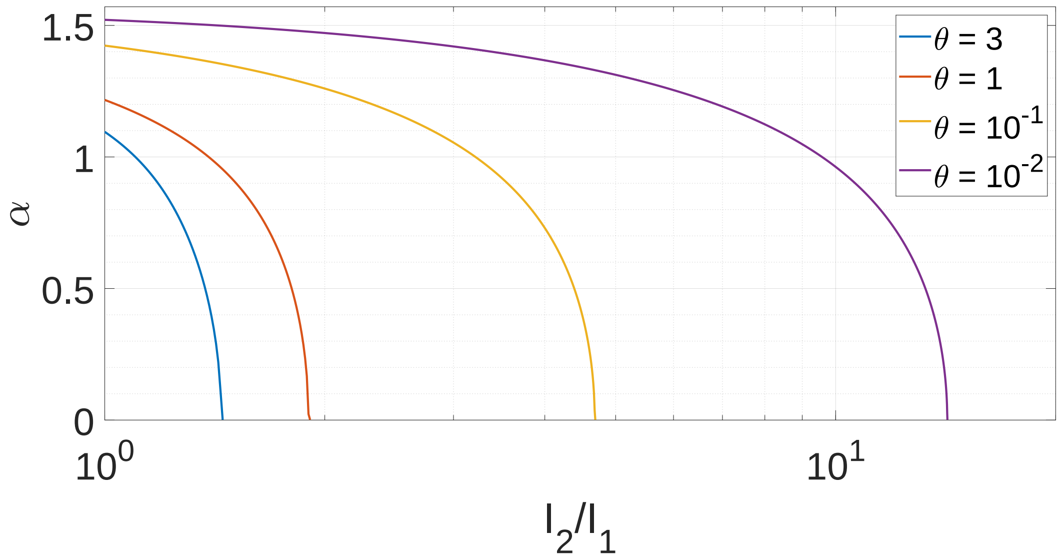

Figure 4.5: The angle $\alpha = \tan^{-1}\left(\frac{q_{\perp,\max}}{q_{\|,\max}}\right)$ is plotted versus I_2/I_1 for temperatures ranging from $\theta = 10^{-2}$ to $\theta = 3$. The solution becomes closer to perpendicular ($\alpha = \pi/2$) at lower temperatures as well as at higher magnetisations (lower values of I_2/I_1).

et al., 2009). While for all parameters there are effects in both the parallel and perpendicular directions, the acceleration of particles in the perpendicular direction through pitch-angle diffusion becomes stronger relative to the parallel processes at lower temperatures. This will affect both the angle α and the widths of the particle distribution in the parallel and perpendicular directions, $\theta_\|$ and $\theta_\perp$. The results for the temperature dependence of α obtained match expectations from previous analyses in the non-relativistic regime which show that the temperature anisotropy $A = \theta_\perp/\theta_\|$ caused by the non-resonant interaction decreases as the temperature increases (Wang et al., 2006).

For all temperatures θ examined, α always decreases toward 0 as the magnetisation decreases. This decrease is largely due to the behaviour of the parallel advection term $\left(\frac{\partial F_0}{\partial t}\right)_{\|,1}$. First, as I_2/I_1 increases, this term becomes positive for $q_\| > 0$, which is in contrast to the case for high magnetisations ($I_2/I_1 \sim 1$) where $\left(\frac{\partial F_0}{\partial t}\right)_{\|,1}$ is negative for $q_\| > 0$. This can be seen by examining the co-

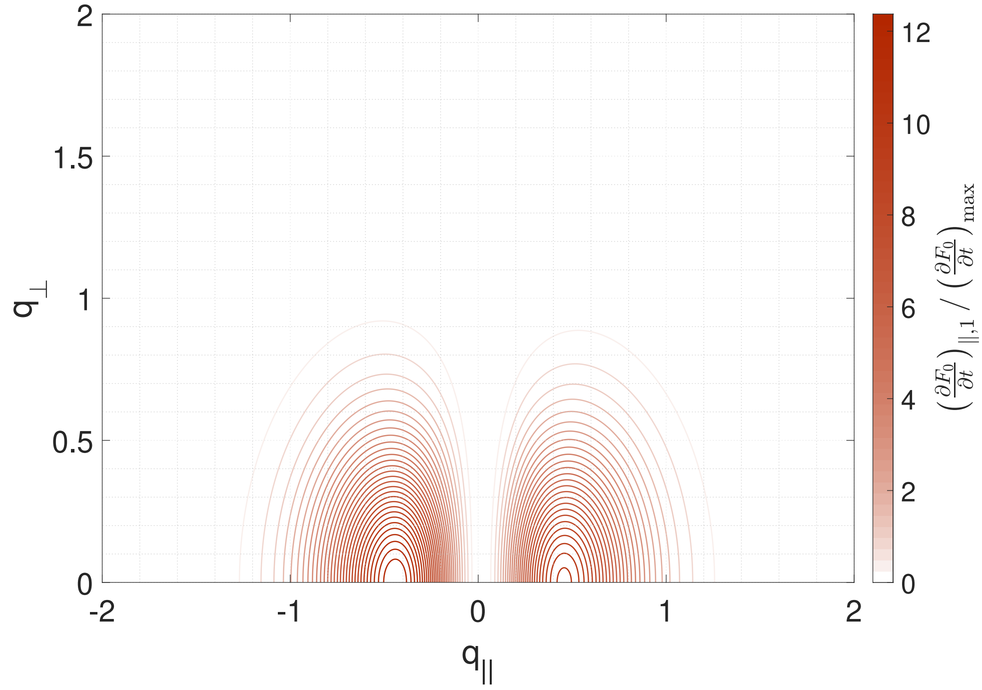

Figure 4.6: Contour plot of $\left(\frac{\partial F_0}{\partial t}\right)_{\|,1}$ for a Maxwell-Jüttner distribution in the low/intermediate magnetisation regime for $\theta = 0.1$ and $I_2/I_1 = 30$. The values are normalised to the maximum value of $\frac{\partial F_0}{\partial t}$. In contrast to the case in Fig. 4.3a where $I_2/I_1 = 1$, for these parameters the contribution from this term consists of a strong $\left(\frac{\partial F_0}{\partial t}\right) > 0$ for both positive and negative $q_\|$.

efficient for this term on line 1 of Eq. (3.5). As I_2/I_1 increases, the term $2\frac{I_2 q_\|}{\gamma^2}$ becomes greater in magnitude than the other terms contributing to $\left(\frac{\partial F_0}{\partial t}\right)_{\|,1}$. As there is an additional factor of $-q_\|$ from the partial derivative $\frac{\partial F}{\partial q_\|}$ in the case of a Maxwell-Jüttner distribution, the dominance of this term results in $\left(\frac{\partial F_0}{\partial t}\right)_{\|,1}$ being positive across all of momentum space. This is shown in Fig. 4.6, which displays $\left(\frac{\partial F_0}{\partial t}\right)_{\|,1}$ for $I_2/I_1 = 30$. This figure also shows that $\left(\frac{\partial F_0}{\partial t}\right)_{\|,1}$ is centred at $q_\perp = 0$, contributing to a decrease in α. This is in contrast to the contribution from the parallel and mixed diffusion terms, which are not centred at $q_\perp = 0$ (see Fig. 4.3c and 4.3e respectively).

Furthermore, the parallel advection term increases in magnitude as I_2/I_1 increases, becoming larger than all others at $I_2/I_1 \sim 1.2$ for $\theta = 10^{-1}$. This can be seen in Fig. 4.7 where the maximum value of each term $\left(\frac{\partial F_0}{\partial t}\right)_{x,\max}$ from Eq. (3.5) is plotted, with $\left(\frac{\partial F_0}{\partial t}\right)_{\parallel,1,\max}$ shown by the solid blue line. These values in Fig. 4.7 are normalised to the overall $\left(\frac{\partial F_0}{\partial t}\right)_{max}$. The value of I_2/I_1 at which the parallel advection term becomes largest is temperature dependent, with the value increasing as the temperature decreases. The other major terms at $I_2/I_1 \sim 1$ are $\left(\frac{\partial F_0}{\partial t}\right)_{\perp,2}$ and $\left(\frac{\partial F_0}{\partial t}\right)_{mix}$, shown by the solid purple and green lines in Fig. 4.7 respectively. As both these terms are second order, they are relatively stronger at lower temperatures due to the factor of θ^{-2} from the derivatives $\frac{\partial^2 F}{\partial q_\perp^2}$ and $\frac{\partial^2 F}{\partial q_\parallel \partial q_\perp}$. This implies that the ratio I_2/I_1 above which the parallel advection term becomes dominant increases at lower temperatures. The increase in strength of the parallel advection term, as well as the relative weakness of the mixed term as the magnetisation decreases, results in $\left(\frac{\partial F_0}{\partial t}\right)_{max}$ shifting closer to $q_\perp = 0$. As is shown in Figs. 4.4c and 4.4d, this combination of factors results in an overall initial evolution that is closer to parallel advection in the low magnetisation parameter space, though pitch-angle diffusion still occurs on a smaller scale.

The reduction in the relative strength of the pitch-angle diffusion relative to the parallel processes when $I_2/I_1 \gg 1$ results in evolved distributions that do not display the obvious crescent shapes observed at high magnetisations (such as in Fig. 4.1c), as discussed in our previous work (Long & Pe'er, 2023). However, particles do still continue to be moved to higher perpendicular momenta for $q_\parallel > 0$ even when $\alpha = 0$, though with much reduced values of f_{inv}. This is shown in our numerical results presented in Sec. 4.3.1.

To summarise the conclusions of the previous paragraphs, the acceleration of particles to larger perpendicular momenta values becomes relatively stronger both as the magnetisation increases and the temperature decreases, resulting in an increase in α up to a maximum value of $\alpha = \pi/2$. This value however does not correspond to the most efficient population inversion as the resulting evolution is almost entirely perpendicular, while for the formation of the population inversion some contribution from the mixed and parallel terms is naturally required to produce a crescent shape. The maximum value of f_{inv} is therefore obtained in the range $0 < \alpha < \pi/2$. We note that these results

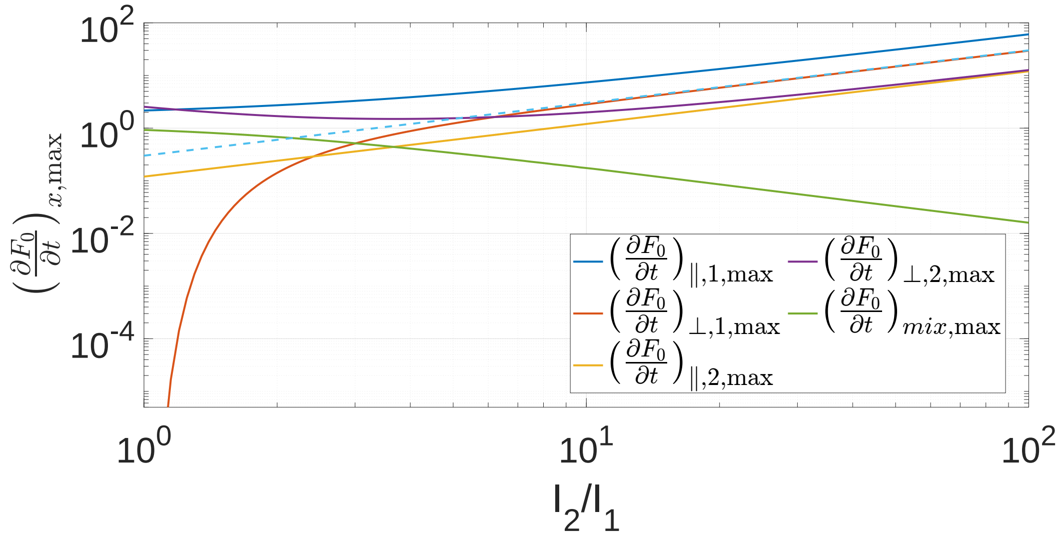

Figure 4.7: Plot of the maximum value of every term in Eq. (3.5), normalised to the maximum value of the total $(\frac{\partial F_0}{\partial t})_{\max}$. The dashed cyan line shows a fit of $\left(\frac{\partial F_0}{\partial t}\right)_{\perp,1,\max} \propto I_2/I_1$. This trend is followed by all terms except the mixed one for $I_2/I_1 \gg 1$. These values are calculated for a temperature of $\theta = 10^{-1}$. As the temperature increases, the first order terms $\left(\frac{\partial F_0}{\partial t}\right)_{\|,1}$ and $\left(\frac{\partial F_0}{\partial t}\right)_{\perp,1}$ will become stronger relative to the others, though the overall trends will be unchanged.

are the equivalent of the mechanism becoming less efficient as the plasma β increases, a result also seen in the non-relativistic regime (Wang & Wu, 2009). We also emphasize that the maximum value of f_{inv} is not solely dependent on α, but also strongly depends on the mixed term as discussed in detail in Secs. 4.2.1 and 4.2.3.

4.2.3 The mixed term and formation of a population inversion

Based on our previous analysis in Sec. 4.2.1, the mixed term is a crucial element to the formation of the population inversion. We emphasize that the mixed term is generally not the largest in magnitude and therefore does not dominate the overall form of the evolved distribution, especially at lower magnetisations. However, it provides the necessary positive $\frac{\partial F_0}{\partial t}$ for $q_\perp > 0$ and $q_\parallel > 0$ that leads to the crescent shape of the distribution. Furthermore, we show in Sec. 4.3 below that the trends followed by the mixed term closely match our numerical results. In order to examine the parametric dependence of this term, it is useful to compare its maximum value $\left(\frac{\partial F_0}{\partial t}\right)_{mix,\max}$ to that of the other terms. Fig. 4.8 presents the ratio of $\left(\frac{\partial F_0}{\partial t}\right)_{mix,\max}$ to the parallel and perpendicular terms $\left(\frac{\partial F_0}{\partial t}\right)_{\parallel,\max}$ and $\left(\frac{\partial F_0}{\partial t}\right)_{\perp,\max}$ as well as to the overall $\left(\frac{\partial F_0}{\partial t}\right)_{\max}$ and the sum of all the other terms except the mixed term $\left(\frac{\partial F_0}{\partial t}-\left(\frac{\partial F_0}{\partial t}\right)_{mix}\right)_{\max}$. Here $\left(\frac{\partial F_0}{\partial t}\right)_{\parallel,\max}=\left(\left(\frac{\partial F_0}{\partial t}\right)_{\parallel,1}+\left(\frac{\partial F_0}{\partial t}\right)_{\parallel,2}\right)_{max}$ and $\left(\frac{\partial F_0}{\partial t}\right)_{\perp,\max}=\left(\left(\frac{\partial F_0}{\partial t}\right)_{\perp,1}+\left(\frac{\partial F_0}{\partial t}\right)_{\perp,2}\right)_{max}$ are the maximum value of combined parallel and perpendicular terms respectively. We combine these terms for clarity of presentation as all the individual terms follow the same trends for $I_2/I_1 \gg 1$, as shown in Fig. 4.7.

In all cases except that of the comparison to the overall $\left(\frac{\partial F_0}{\partial t}\right)_{\max}$, the ratio is proportional to $(I_2/I_1)^{-2}$ at large values of I_2/I_1 ($I_2/I_1 \gtrapprox 6$ for $\theta = 0.1$ as in Fig. 4.8). This is the equivalent of $\left(\frac{\partial F_0}{\partial t}\right)_{mix,\max}/\left(\frac{\partial F_0}{\partial t}\right)_{x,\max} \propto \bar{\sigma}$ at these low and intermediate magnetisations, as $I_2/I_1 \propto \bar{\sigma}^{-1/2}$ for $\bar{\sigma} \ll 1$. As I_2/I_1 approaches 1, equivalent to higher magnetisations of $\bar{\sigma} \gtrapprox 1$, the ratio flattens out, becoming more weakly dependent on I_2/I_1 (see Fig. 3.1 for the temperature dependent I_2/I_1-$\bar{\sigma}$ relationship). These results are derived semi-analytically in Appendix B below.

These trends are true for all temperatures, though the magnetisation at which the linear relationship begins is temperature dependent. This can be seen in Fig. 4.9, which presents the ratio $\left(\frac{\partial F_0}{\partial t}\right)_{mix,\max}/\left(\frac{\partial F_0}{\partial t}\right)_{\perp,\max}$ for different temperatures. We focus on this specific ratio in Fig. 4.9 and in Sec. 4.3 because the other ratios $\left(\frac{\partial F_0}{\partial t}\right)_{mix,\max}/\left(\frac{\partial F_0}{\partial t}\right)_{\parallel,\max}$ and $\left(\frac{\partial F_0}{\partial t}\right)_{mix,\max}/\left(\frac{\partial F_0}{\partial t}-\left(\frac{\partial F_0}{\partial t}\right)_{mix}\right)_{\max}$ show the same trends, and thus carry no new information. The relationship $\left(\frac{\partial F_0}{\partial t}\right)_{mix,\max}/\left(\frac{\partial F_0}{\partial t}\right)_{\perp,\max} \propto (I_2/I_1)^{-2}$ begins at increasing values of I_2/I_1 as the temperature decreases.

To clarify this behaviour in terms of a more intuitive physical quantity, the same ratio is plotted in Fig. 4.10 versus the relativistic magnetisation σ. This

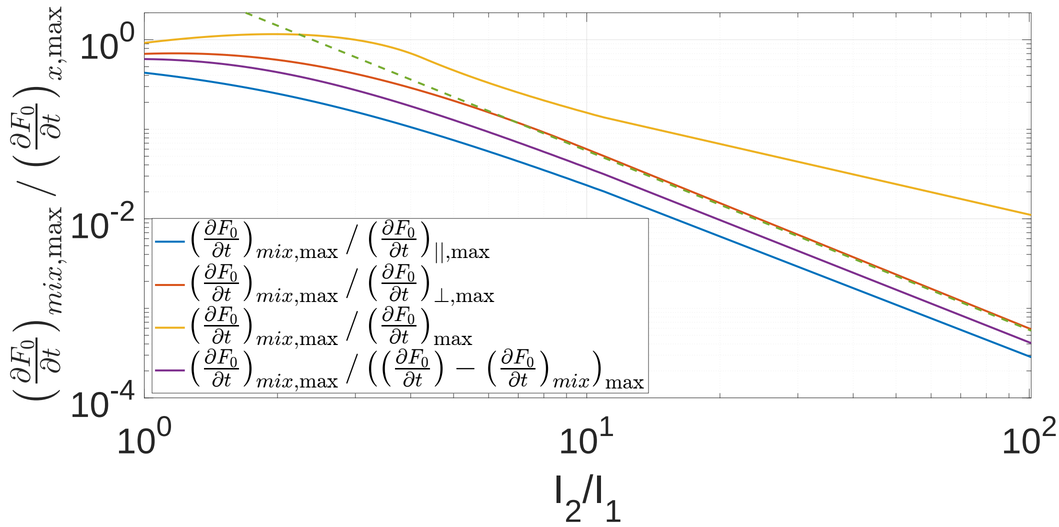

Figure 4.8: Plot of the ratio of $\left(\frac{\partial F_0}{\partial t}\right)_{mix,\max}$ for the mixed term to the maximum value of the parallel terms $\left(\frac{\partial F_0}{\partial t}\right)_{\|,\max}$ (blue), perpendicular terms $\left(\frac{\partial F_0}{\partial t}\right)_{\perp,\max}$ (orange), overall solution $\left(\frac{\partial F_0}{\partial t}\right)_{\max}$ (yellow) and $\left(\left(\frac{\partial F_0}{\partial t}\right) - \left(\frac{\partial F_0}{\partial t}\right)_{mix}\right)_{\max}$ (purple). The dashed green line indicates a fit of $\left(\frac{\partial F_0}{\partial t}\right)_{mix,\max} / \left(\frac{\partial F_0}{\partial t}\right)_{\perp,\max} \propto (I_2/I_1)^{-2}$. These values are calculated for a temperature of $\theta = 10^{-1}$.

shows the $\left(\frac{\partial F_0}{\partial t}\right)_{mix,\max} / \left(\frac{\partial F_0}{\partial t}\right)_{\perp,\max} \propto \sigma$ trend at low magnetisations, as described above. The region where the ratio flattens out, namely $I_2/I_1 \lesssim 2-10$ (depending on the temperature), corresponds to a much larger region in terms of the magnetisation due to the asymptotic behaviour of the $I_2/I_1 - \sigma$ relationship as the relativistic Alfvén velocity approaches the speed of light. This results in the relatively broader non-power-law regions in Fig. 4.10 compared to Fig. 4.9. These trends are reproduced in the numerical results for f_{inv} presented below in Sec. 4.3, supporting our conclusion about the importance of the mixed term.

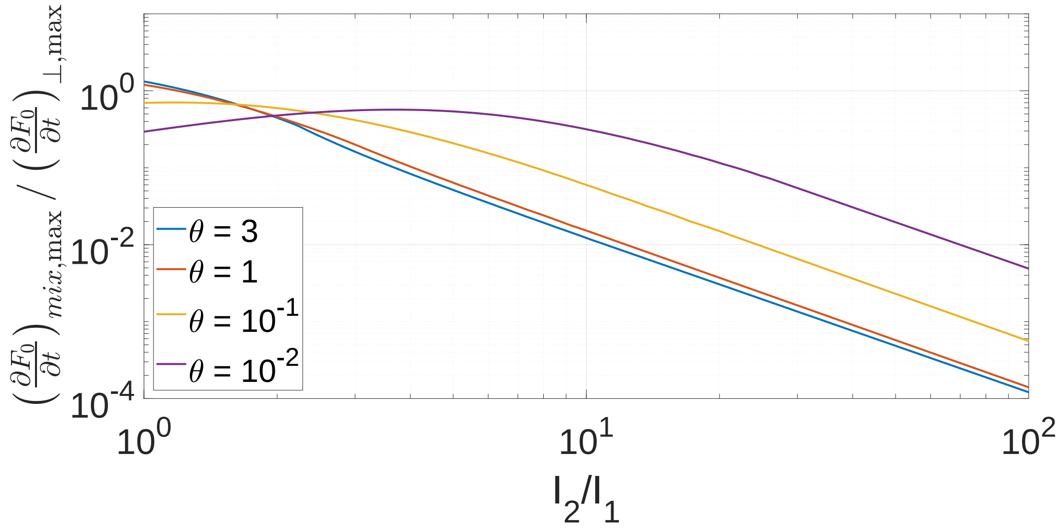

Figure 4.9: The ratio of the maximum value of the mixed term, $\left(\frac{\partial F_0}{\partial t}\right)_{mix,\max}$, to the maximum value of the perpendicular terms, $\left(\frac{\partial F_0}{\partial t}\right)_{\perp,\max}$, plotted versus I_2/I_1. Each line represents a different temperature, with the peak of the ratio not at $I_2/I_1 = 1$ for $\theta = 10^{-2}$, as discussed in Sec. 4.3.

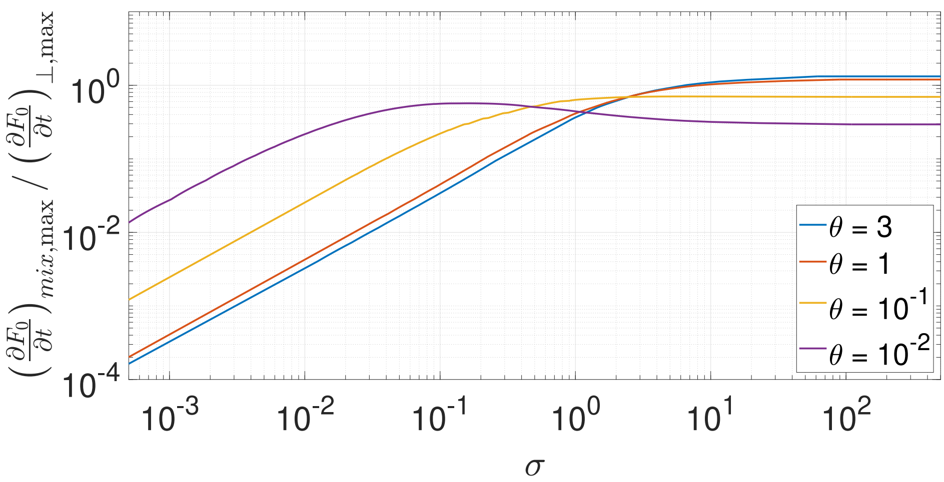

Figure 4.10: The ratio of the maximum value of the mixed term, $\left(\frac{\partial F_0}{\partial t}\right)_{mix,\max}$, to the maximum value of the perpendicular terms, $\left(\frac{\partial F_0}{\partial t}\right)_{\perp,\max}$, plotted versus the relativistic magnetisation σ. Note the broadness of the region where $\left(\frac{\partial F_0}{\partial t}\right)_{mix,\max} / \left(\frac{\partial F_0}{\partial t}\right)_{\perp,\max}$ is not proportional to σ in comparison to the equivalent region in Fig. 4.9, caused by the asymptotic behaviour of σ as a function of I_2/I_1 for $\sigma > 1$.

4.3 Results

4.3.1 The energy in the population inversion

Fig. 4.11a to 4.11d show the fraction of energy in the population inversion, f_{inv} versus σ for temperatures of $\theta = \{3, 1, 10^{-1}, 10^{-2}\}$ respectively. All the results below are presented in terms of σ rather than I_2/I_1 as the magnetisation is a more useful physical quantity. The results are presented for values of $\eta = 1$ and $\eta = 0.3$. This range of values represents the upper limits on the maximum achievable values of f_{inv} while satisfying the constraints of quasilinear theory. The theory is valid for values of η not much smaller than unity (e.g. Yoon et al., 2009). Magnetisations of $\sigma > 10^{-4}$ were examined. The results show that the behaviour of f_{inv} with respect to the magnetisation of the plasma can be divided up into three regimes. These consist of a high magnetisation regime where f_{inv} is only weakly dependent on σ, an intermediate magnetisation regime where $f_{inv} \propto \sigma$, and a low magnetisation regime where f_{inv} decreases rapidly as the magnetisation decreases. These regimes and their properties are discussed in detail below, and a summary of the different regimes is given in Table 4.1.

The transition between the high and intermediate magnetisation regimes occurs at $\sigma = \sigma_1$. We define this value as the maximum magnetisation for which $f_{inv} \propto \sigma$. Above this value, the fraction of energy in the population inversion depends weakly on the magnetisation, as can be seen by the flattening out of f_{inv} for $\sigma > \sigma_1$ in Fig. 4.11a to 4.11d. This transition occurs for all η values presented. We note that this transition is not a sharp cut-off at precisely σ_1, but a more gradual change, as can be seen in both the numerical results (Fig. 4.11a to 4.11d) and the ratio of $\left(\frac{\partial F_0}{\partial t}\right)_{mix,\max} / \left(\frac{\partial F_0}{\partial t}\right)_{\perp,\max}$ (Fig. 4.9 and 4.10). As discussed in Sec. 4.2.1, the relative strength of the mixed term is important to the formation of the population inversion. Indeed, the trend of f_{inv} can be explained by the similar behaviour of $\left(\frac{\partial F_0}{\partial t}\right)_{mix,\max} / \left(\frac{\partial F_0}{\partial t}\right)_{\perp,\max}$ in the same magnetisation regime, as shown in Fig. 4.10.

While for higher temperatures of $\theta > 10^{-1}$ the fraction of energy in the inversion simply transitions to an asymptotic value for $\sigma > \sigma_1$, this is not the case for $\theta = 10^{-2}$ (see Fig. 4.11d). At this lower temperature, both f_{inv} and $\left(\frac{\partial F_0}{\partial t}\right)_{mix,\max} / \left(\frac{\partial F_0}{\partial t}\right)_{\perp,\max}$ initially increase with σ until reaching a peak value at σ_{peak}. This magnetisation corresponds to the value at which the inversion contains the highest energy fraction for a given temperature. However, f_{inv} then decreases as σ increases up to σ_0, which we define as the magnetisation at which $I_2/I_1 = 1$. As discussed in Sec. 3.2.1, this value is obtained when $v_{A,rel} \to c$. The change in behaviour at lower temperatures can be explained by noting that at σ_0, the direction of $\left(\frac{\partial F_0}{\partial t}\right)_{\max}$ is almost exactly perpendicular for $\theta = 10^{-2}$, as is shown in Fig. 4.5. This is not the most efficient angle for the formation of the crescent shape, as particles need to be accelerated to larger values of $q_\perp$ in the region $q_\parallel > 0$, rather than in the region centred at $q_\parallel = 0$.

When the magnetisation $\sigma > \sigma_0$, the ratios of the various terms in Eq. (3.5) are almost constant as $v_{A,rel} \to c$. Therefore, the fraction of energy in the inversion is independent of σ when $\sigma > \sigma_0$. This region is shown by the horizontal bars in Fig. 4.11a to 4.11d, which continue indefinitely to higher values of σ. For temperatures of $\theta \geq 10^{-1}$, σ_0 also corresponds to σ_{peak}, as the ratio $\left(\frac{\partial F_0}{\partial t}\right)_{mix,\max} / \left(\frac{\partial F_0}{\partial t}\right)_{\perp,\max}$ is at its greatest for $I_2/I_1 = 1$. Therefore, for these temperatures f_{inv} is at its maximum value for all $\sigma \geq \sigma_0$.

Below σ_1, the plasma is in the intermediate magnetisation region where the fraction of energy in the population inversion increases linearly with σ. As in the high magnetisation regime, this behaviour can be explained by the relative strength of the mixed term, as $\left(\frac{\partial F_0}{\partial t}\right)_{mix,\max} / \left(\frac{\partial F_0}{\partial t}\right)_{\perp,\max}$ is also proportional to σ for $\sigma < \sigma_1$. This reduction in f_{inv} corresponds to the weakening of the pitch-angle diffusion as the magnetisation decreases (and plasma β increases), as discussed in Sec. 4.2.2. In this regime the crescent shape no longer forms as clearly as in the high magnetisation regime, as can be seen by comparing Fig. 4.4c, which shows $\frac{\partial F_0}{\partial t}$ in this intermediate magnetisation regime, to Fig. 4.4a and 4.4b which have $\sigma > \sigma_1$.

Table 4.1: A summary of the relationship between f_{inv} and σ in the different magnetisation regimes

magnetisation	f_{inv}
$\sigma_0 < \sigma$	Constant
$\sigma_1 < \sigma < \sigma_0$	Weakly dependent on σ
$\sigma_2 < \sigma < \sigma_1$	$f_{inv} \propto \sigma$
$\sigma < \sigma_2$	Decreases sharply as σ decreases

The $f_{inv} \propto \sigma$ relationship holds for all $\sigma_1 > \sigma > \sigma_2$. Here, σ_2 is the magnetisation value below which a cut-off exists. This effect occurs due to the appearance of a positive region of $\frac{\partial F}{\partial t}$ centred at $q_\perp = 0$ and $q_\| < 0$ once the magnetisation drops below this cut-off value. Above this threshold there is little to no diffusion in the parallel direction, with particles rather being moved to larger positive $q_\|$ values only. However, below σ_2, particles begin to spread in both the positive and negative $q_\|$ direction, sharply reducing the fraction of particles being added to the population inversion. The contrast in $\frac{\partial F}{\partial t}$ between the two scenarios is visible by comparing Fig. 4.4d, which presents $\frac{\partial F}{\partial t}$ for $A = 1$, to Fig. 4.12, which shows $\frac{\partial F}{\partial t}$ for $A = 1.1$. $I_2/I_1 = 30$ and $\theta = 10^{-1}$ in both cases. In order for this effect to occur, a temperature anisotropy with $\theta_\perp > \theta_\|$ is required, as is shown below. Such an anisotropy always occurs due to the non-resonant interaction (Wang et al., 2006), and the cut-off effect acts to reduce this anisotropy by increasing $\theta_\|$. As discussed in Chapter 3, the strength of A depends on both the magnetisation and temperature. For the low magnetisation regime in question here, the temperature anisotropy is generally small, with $1 \lesssim A < 1.2$, before decreasing to values of $A < 1$ at higher turbulence levels. However, this decrease is not a true change in temperature, but rather is driven by the increase in parallel bulk velocity.

An approximation for the value of σ_2 can be found by determining when $\frac{\partial F}{\partial t}$ first becomes positive for $q_\perp = 0$ and $q_\| < 0$. In Sec. 3.5.1, this was determined to occur at values of

$$q_\| = -\frac{1}{\sqrt{(I_2/I_1)^2(A-1)^2 - 1}}. \tag{4.1}$$

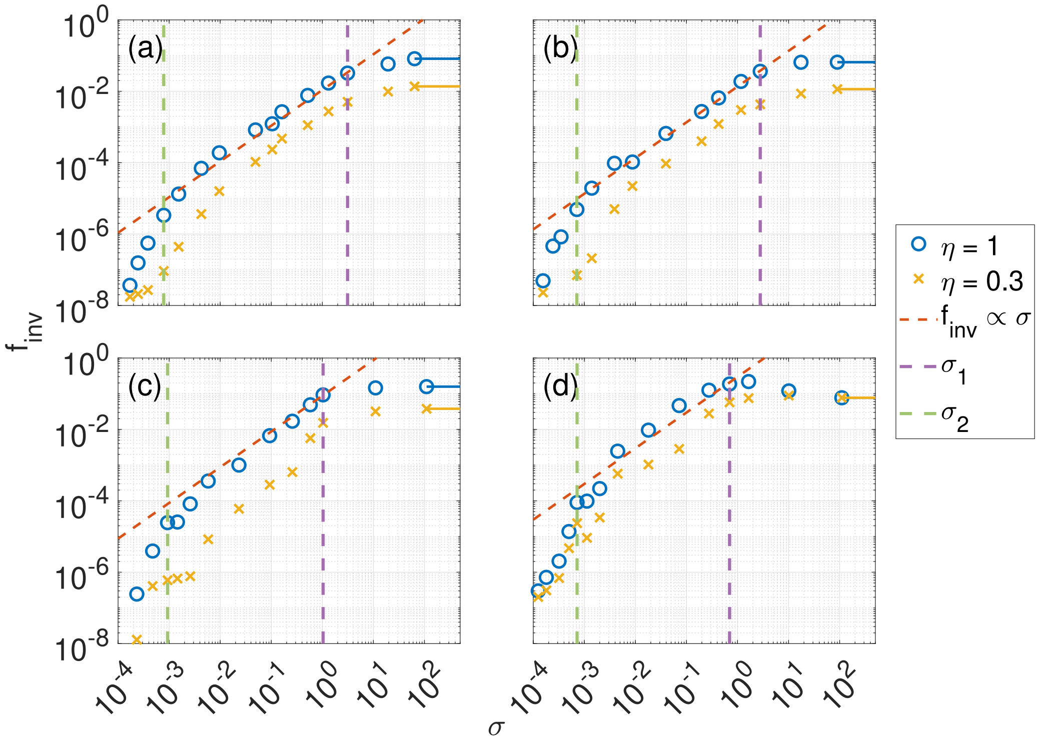

Figure 4.11: The energy in the inversion versus magnetisation, with different temperatures in each panel. **Panel (a)** presents results for $\theta = 3$, **panel (b)** for $\theta = 1$, **panel (c)** for $\theta = 10^{-1}$ and **panel (d)** shows results for $\theta = 10^{-2}$. In each panel the blue circles show the energy fraction obtained for $\eta = 1$, while the yellow 'x's show the energy fraction at $\eta = 0.3$. The purple dashed line (σ_1) divides the high and intermediate magnetisation regime, and the green dashed line (σ_2) is the boundary between the low and intermediate magnetisation regimes, showing where the cut-off occurs. The dashed orange line shows a fit of $f_{inv} \propto \sigma$ in the intermediate magnetisation regime in each case.

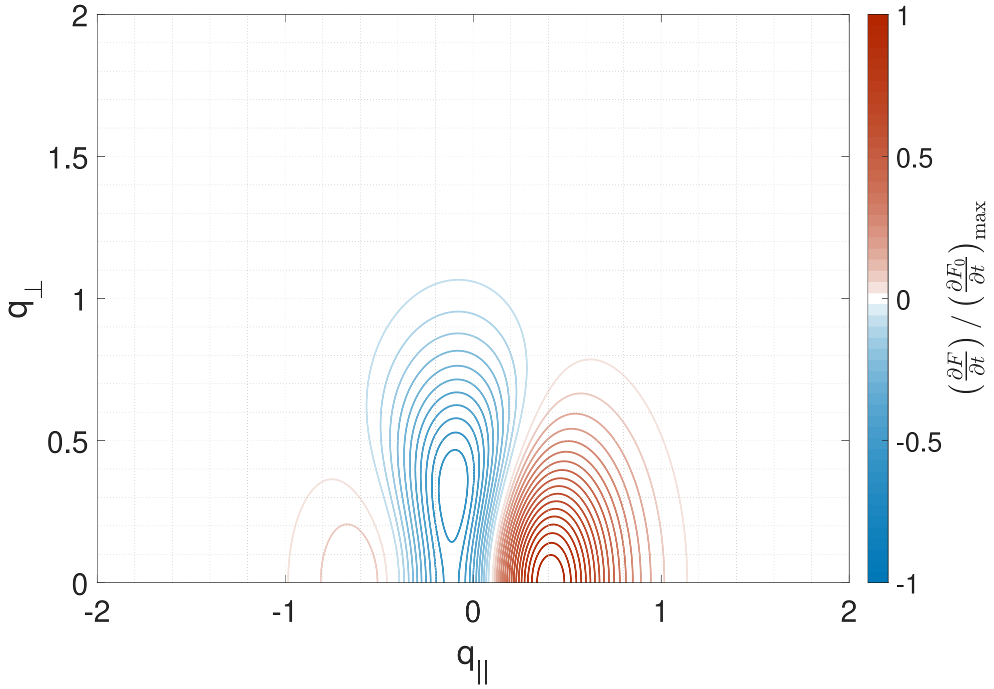

Figure 4.12: Contour plot of $\frac{\partial F}{\partial t}$ for an anisotropic Maxwell-Jüttner distribution in the low magnetisation regime with $\theta = 0.1$, $I_2/I_1 = 30$ and $A = 1.1$. Note the appearance of the positive region of $\frac{\partial F}{\partial t}$ centred at $q_\perp = 0$ for $q_\parallel < 0$, which is completely absent when no temperature anisotropy is present.

As I_2/I_1 increases, the required anisotropy becomes smaller. In other words, this effect occurs sooner for lower magnetisations, resulting in the lower values of f_{inv} as σ decreases. This relationship is only weakly dependent on the temperature, with the only effect occurring as a result of the temperature dependence of the $\sigma - I_2/I_1$ relationship, as shown in Fig. 3.1. The maximum value of σ for which a positive $\frac{\partial F}{\partial t}$ in the $q_\parallel < 0$ region will appear is plotted in Fig. 4.13 as a function of the temperature anisotropy. The figure extends only to $\sigma = 10^2$ as this is the approximate value at which $I_2/I_1 \to 1$. At low magnetisations the cut-off effect occurs for any anisotropy $A > 1$. The effect will therefore have an impact on the evolution of the distribution almost immediately. The needed anisotropy increases as the magnetisation increases, with $A = 2$ required for $\sigma > \sigma_0$ (equivalent to $I_2/I_1 = 1$). This result means that the positive $\frac{\partial F}{\partial t}$ in the $q_\parallel < 0$ region will appear for all parameters provided a sufficient temperature anisotropy exists, though in the high magnetisation cases the crescent shape will have already largely formed before this occurs. The weak temperature dependence is also apparent in Fig. 4.13, with only a factor of ~ 2 in difference in the values of σ for $\theta = 10^{-2}$ and $\theta = 3$. This result can also be seen in our numerical results, where σ_2 only varies weakly between temperatures. However, we note that the values of σ_2 shown in Fig. 4.11a to 4.11d are only approximations due to the transition region not being sharp.

A similar effect occurs when the parallel bulk velocity is non-zero. As in Sec. 3.5.1, we calculate $\frac{\partial F(q_\perp=0)}{\partial t}$, though this time for a distribution function given by Eq. (3.23). The resulting expression is

$$\begin{aligned}\frac{\partial F(q_\perp = 0)}{\partial t} = C &\frac{\exp\left(-\theta^{-1}\gamma_b\left(\sqrt{1+q_\parallel^2} - \beta_b q_\parallel\right)\right)}{\theta\gamma_b} \\ &\times \left(I_1\left(q_\parallel + \beta_b\sqrt{1+q_\parallel}\right) - I_2\beta_b q_\parallel - I_3\sqrt{1+q_\parallel^2}\right), \end{aligned} \tag{4.2}$$

where again C contains the constants. In this scenario, $\frac{\partial F(q_\perp=0)}{\partial t}$ becomes positive for $q_\parallel < \gamma\beta_b$ when $\beta_b > I_1/I_2$. This results in a spread of the distribution

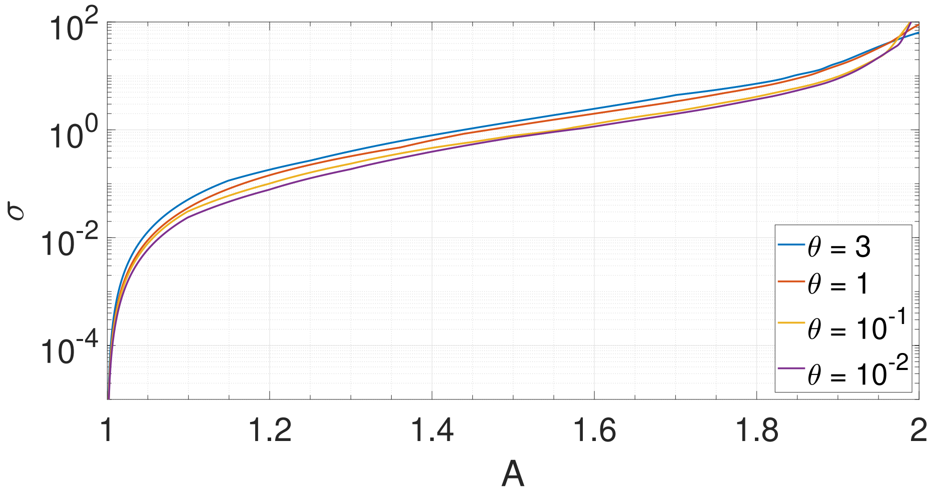

Figure 4.13: The maximum value of σ for which a positive $\frac{\partial F}{\partial t}$ in the $q_{\parallel} < 0$ region will appear, plotted as a function of the temperature anisotropy A. A value of $\sigma \sim 10^2$ corresponds to $I_2/I_1 = 1$. It can be seen that as the magnetisation increases, the required anisotropy A for the cut-off effect to occur also increases from a value of $A \sim 1$ for $\sigma \lesssim 10^{-4}$ to $A \sim 2$ for $\sigma \sim 10^2$. The relationship depends only weakly on the temperature, with the effect becoming relevant for very small temperature anisotropies of close to 1 at low magnetisations in all cases.

to lower parallel momenta, as in the temperature anisotropy case. Similarly, this effect happens for lower bulk velocities at lower magnetisations. Furthermore, as the non-resonant interaction always imparts a parallel bulk velocity, such effects will always occur for high enough turbulence level.

To examine the temperature dependence of the interaction, we plot all the results from Fig. 4.11a to 4.11d together in Fig. 4.14, which shows f_{inv} at $\eta = 1$ for every parameter set examined. There is a clear increase in f_{inv} as the temperature decreases from relativistic values to $\theta = 10^{-2}$. The dependence is most pronounced in the intermediate magnetisation, as can be seen by examining the region $\sigma \lesssim 1$ in Fig. 4.14. For a given σ, f_{inv} increases as the temperature decreases, with a typical difference of over an order of magnitude between results for $\theta = 3$ and $\theta = 10^{-2}$. This indicates that the mechanism becomes less efficient in the relativistic regime at low magnetisations. As discussed in Sec. 4.2.2, this is due to the decrease in relative strength of the pitch-angle diffusion at higher temperatures. The weaker contribution from the mixed term at higher temperatures can be seen in Fig. 4.9 and 4.10, as the relative strength of the mixed term for a given magnetisation decreases as the temperature increases.

In the high magnetisation regime, the difference in f_{inv} for different temperatures is less significant. This is due to the fact that the strength of the mixed term reaches its maximum value at $\sigma \sim 1$ rather than σ_0 for lower temperatures, as shown in Fig. 4.10. The precise values of f_{inv} cannot be compared directly to the values of $\left(\frac{\partial F_0}{\partial t}\right)_{mix,\max} / \left(\frac{\partial F_0}{\partial t}\right)_{\perp,\max}$ as a turbulence level of $\eta > 1$ is required to obtain the maximum population inversion in the majority of cases. However, in all cases values of $f_{inv} > 10^{-2}$ are achieved in the high magnetisation regime for both $\eta = 0.3$ and $\eta = 1$, showing that the non-resonant interaction is capable of producing a substantial population inversion across a wide range of both relativistic and non-relativistic temperatures.

The turbulence level required to reach a given f_{inv} is also temperature dependent, with lower temperatures requiring lower turbulence levels, as can be seen by the smaller differences between the values of f_{inv} for $\eta = 1$ and $\eta = 0.3$ at lower temperatures in Fig. 4.11. At higher temperatures the particles have more kinetic energy, and thus higher turbulence levels are needed to efficiently diffuse them. At lower magnetisations, the interaction is more sensitive to the turbulence level of the Alfvén waves, as can be seen by the $\eta = 0.3$ values dropping more rapidly than those for $\eta = 1$. In order for any significant distortion of the population distribution from a bi-Maxwellian in this part of the parameter space, turbulence levels close to $\eta = 1$ are needed due to the inefficiency of pitch-angle scattering in the low magnetisation regime, as discussed above.

The combination of the general decrease in f_{inv} for lower magnetisations as well as the higher turbulence levels required to reach even these lower levels leads us to conclude that the parameter space $\sigma > \sigma_1$ is the one of most relevance to SME, as here $f_{inv} \gtrsim 10^{-2}$ for all temperatures and a clear crescent

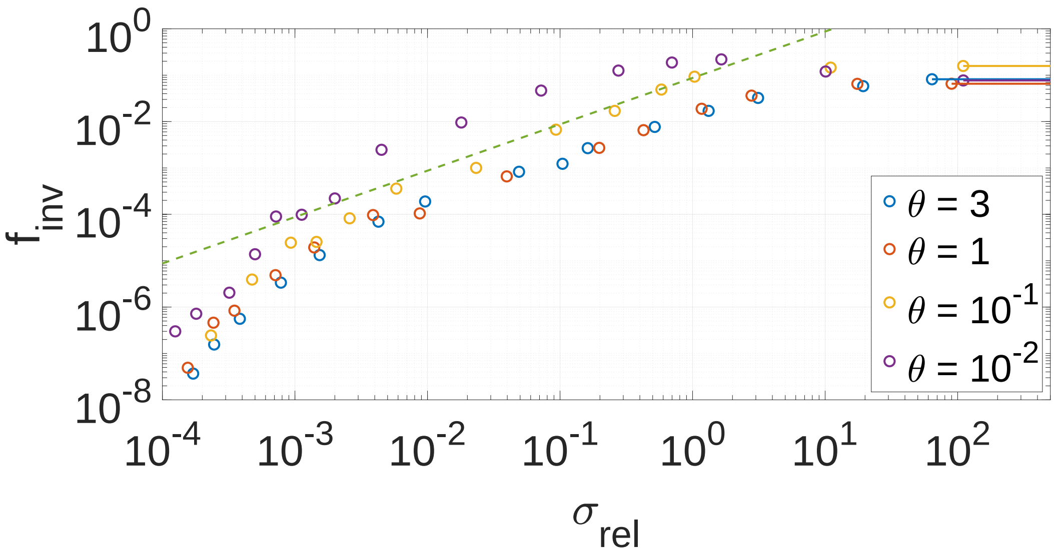

Figure 4.14: The energy in the inversion at $\eta = 1$ versus magnetisation for $\theta = 10^{-2}$ to $\theta = 3$. The green dashed line shows a fit of $f_{inv} \propto \sigma$ in the intermediate magnetisation regime for $\theta = 1$. The value of f_{inv} generally decreases as the temperature increases to relativistic values.

shape is always formed as $\alpha > 0$.

4.3.2 Time-scales

The time taken for the population inversion to form is another important result as the mechanism must operate on a time-scale shorter than the characteristic dynamical time-scale to provide a valid explanation for FRBs. For an exponentially growing η, the time to reach a particular turbulence level is $t(\eta) = (2\Gamma)^{-1} \log(\eta/\eta_0)$. The time-scale therefore depends linearly on the growth rate. Due to the weak dependence on η/η_0, this time-scale is always on the order of $t\Gamma \sim$ a few seconds. We note that as the turbulence approaches its maximum value, $\frac{\partial \eta}{\partial t}$ will naturally decrease, increasing the time taken for the final part of the evolution. Assuming that the Alfvén wave turbulence emerges from the central magnetar rather than the plasma in the emission region, the value of $\frac{\partial \eta}{\partial t}$ is independent of the plasma temperature. As a result the time-scale only depends on temperature through the lower turbulence levels required at lower temperatures. This therefore results in only a minor difference in time-scales between the results for $\theta = 3$ and $\theta = 10^{-2}$. While the turbulence level is independent of the Alfvén wave spectrum, the time-scale will be affected by the value of Γ_k and whether Γ_k is constant or varies with wave-number. The time-scale for a specific spectrum can be retrieved using the details described in Sec. 3.2.2. To explore the validity of these time-scales in the context of FRBs we compare the time-scales described here to those expected from magnetars in Sec. 4.4.2 below.

4.4 Discussion

4.4.1 SME efficiency and other plasma instabilities

The numerical results presented in Sec. 4.3 above demonstrate that energy fractions of up to $f_{inv} \gtrsim 10^{-2}$ are attainable at high magnetisations through the non-resonant interaction between Alfvén waves and relativistic plasma. The energy fraction decreases linearly with σ in the intermediate regime $\sigma_2 < \sigma < \sigma_1$ before dropping sharply below the cut-off σ_2. The time-scale in all cases is $t \sim (2\Gamma_9)^{-1} \log(\eta/\eta_0) 10^{-9}$ s. The above results are dependent on the temperature, with approximately an order of magnitude difference in f_{inv} between $\theta = 10^{-2}$ and $\theta = 3$ in the low and intermediate magnetisation regimes for $\eta = 1$. The energy in the inversion depends strongly on the energy density of the Alfvén waves, with values of $\eta \gtrsim 0.1$ required to produce significant effects. We discuss the applicability of these parameters to magnetars and other neutron stars in Sec. 4.4.3, as these are the leading candidates for FRB progenitors, with one FRB directly observed to have originated from the Galactic magnetar SGR 1935+2154 (CHIME/FRB Collaboration et al., 2020b).

The results for f_{inv} summarised above and presented in detail in Sec. 4.3.1 can be contrasted with the efficiency results obtained from PIC simulations of relativistic shocks, another important candidate in explaining SME in relativistic environments (e.g. Gallant et al., 1992; Amato & Arons, 2006; Plotnikov & Sironi, 2019). In the relativistic shock model, the population inversion is not formed through non-resonant interactions with Alfvén wave. Instead, a soliton-like structure forms at the front of a shock with high magnetisation. In this structure, the particles gyrating around the enhanced magnetic field near the shock front form a semi-coherent ring-like distribution in momentum space which can support SME (e.g. Alsop & Arons, 1988; Gallant et al., 1992; Amato & Arons, 2006; Plotnikov & Sironi, 2019).

Comparing the results obtained for f_{inv} from the non-resonant interaction to the efficiency values from the relativistic shock model shows several differences in the viable parameter spaces. In the high magnetisation regime, the results presented above in Sec. 4.3 produce considerably higher f_{inv} than in the case of relativistic shocks, where an efficiency of $\sim 10^{-3}\sigma^{-1}$ for $\sigma \gg 1$ has been found (Sironi et al., 2021). On the other hand, in the intermediate magnetisation regime, for a magnetisation of $\sigma \sim 0.1$ the shock efficiency was found to be ~ 0.1 (Plotnikov & Sironi, 2019), comparable to the values found in this work for $\theta > 10^{-2}$. These are approximately $f_{inv} \sim 2 \times 10^{-2}\sigma$ for $\sigma_2 < \sigma < 1$ for $\theta = 1$ and $\theta = 3$, increasing to $f_{inv} \sim 0.5\sigma$ for $\sigma_2 < \sigma \lesssim 0.3$ at the lower temperature of $\theta = 10^{-2}$. These values are obtained assuming $\eta = 1$, and decrease at lower values of η. These results suggest that non-resonant interactions with Alfvén waves may be the more viable mechanism at high magnetisations, while relativistic shocks, if they exist, may be more relevant at lower magnetisations.

We emphasise that the efficiency in the relativistic shock scenario and f_{inv} are not the same quantity. Although the efficiency values above describe the fraction of energy actually emitted by SME, f_{inv} provides an upper limit on the total energy fraction available from the deformed distribution. Not all of this energy will necessarily be extracted due to the influence of other plasma processes. However, this may not affect the overall efficiency, provided that all other plasma instabilities have a slower growth rate. Furthermore, as will be shown in Chapter 5, the growth rate at higher temperatures will reduce to 0, as occurs in other maser scenarios (Amato & Arons, 2006; Iwamoto et al., 2017; Babul & Sironi, 2020).

The impact of plasma instabilities is most relevant for the high temperature and low magnetisation regions of the parameter space. As noted above, the particle distribution can be roughly approximated as a bi-Maxwellian, especially in the low magnetisation regime where the fraction of energy in the inversion is small. In such distributions both the firehose and mirror instabilities are important. The firehose instability occurs when the parallel pressure is very large. When the pressure is stronger than the magnetic tension, it forces the tightening of any kinks in the magnetic field lines, similar to the situation with a water hose. In contrast, the mirror instability forms when the perpendicular pressure is larger than the parallel pressure. Particles can get trapped in the resulting region of lower magnetic field, further increasing the perpendicular pressure and causing the instability to grow. These two instabilities have stability criteria of $A > 1 - 1/\beta_{\parallel}$ for the firehose instability and $A < 1 + 1/\beta_{\parallel}$ for the mirror instability (Gary, 1993). Here $\beta_{\parallel} = 2\theta_{\parallel}/\sigma$ is the parallel plasma beta.

When $\sigma \gg 1$, $\beta_{\parallel} \ll 1$ for all temperatures, resulting in a distribution that is not susceptible to either of the instabilities. However, when $\sigma \ll 1$ and the temperature is relativistic, even a small temperature anisotropy will result in the stability criteria no longer being satisfied. In the case of the low magnetisation regime, the temperature anisotropy is typically in the range $1 \lesssim A \lesssim 1.2$, and so the distribution will be potentially affected by the mirror instability at high temperatures. This means that plasmas in the low and intermediate magnetisation regimes have both lower energy fractions and are more susceptible to instabilities. On the other hand, this issue does not affect the most efficient parameters, namely those in the high magnetisation regime, strengthening the conclusion that this is the regime of most relevance for SME in astrophysical scenarios. The plasma may also be susceptible to turbulent cascades when Alfvén wave spectra with perpendicular components are considered (Nättilä & Beloborodov, 2022).

4.4.2 Magnetar time-scales

As magnetars are the primary candidate for FRB progenitors(CHIME/FRB Collaboration et al., 2020b), we consider the typical time-scales of such objects. Magnetars have two time-scales of interest, namely the radius and period of the star, either of which could potentially provide the crucial time variability in the Alfvén wave field which is a requirement for a non-resonant interaction. Firstly, the magnetar radius R_* corresponds to a time-scale of $\sim R_*/c = 3.3\times10^{-5} R_{*,6}$ s. The time-scale of the magnetar rotational period is significantly longer, typically $\sim 1 - 10$ s (Mereghetti, 2008; Olausen & Kaspi, 2014), [1], though young magnetars may have millisecond periods (Dall'Osso & Stella, 2022).

Considering the Alfvén wave turbulence grows on a time-scale which is some fraction χ of these magnetar time-scales, the time to reach a turbulence value of η is $t \sim 1.7 \times 10^{-5} \chi^{-1} R_{*,6} \log(\eta/\eta_0)$ s for the magnetar radius time-scale. The period scale produces longer times of $t \sim 0.5\chi^{-1} P \log(\eta/\eta_0)$. While the period time-scale is considerably longer, it naturally has a wider range of possible values due to the variation in neutron star periods. In both cases the constraint that $\Gamma \ll \Omega$ is comfortably satisfied in the FRB emission regions for a wide range of χ. These time-scales are applicable across the whole temperature and magnetisation parameter space, with only a weak dependence on temperature in the form of the increased turbulence levels required when the initial temperature is higher.

The time-scale of the mechanism is especially important to FRBs as it is unclear if all sources repeat or not. While some studies show observational differences between apparent one-off bursts and repeaters (Pleunis et al., 2021b; Petroff et al., 2022), these one-off bursts may also be rarer, brighter events than other undetected signals from the same object (Kirsten et al., 2024). For potential one-off bursts, the time taken for the inversion to form is not a limiting factor. On the other hand, if most or all FRBs repeat, the inversion must form with times shorter than the typical time between bursts. While

[1] https://www.physics.mcgill.ca/ pulsar/magnetar/main.html

this model cannot intrinsically produce time-scales as short as the ~ 60 ns observed from the fastest repeaters (Nimmo et al., 2022), the vast majority of FRBs repeat on much longer time-scales, typically on the order of seconds or longer (Lanman et al., 2022; Hu & Huang, 2023). Variability on a very short time-scale ($< \mu$s) may also be induced by the propagation of the FRB signal through a highly magnetised plasma, rather than as a result of the emission process itself (Sobacchi et al., 2024a). These factors ensure that the mechanism is not limited to scenarios with extremely high values of Γ as shorter time-scales would, suggesting that magnetars are viable sources for this mechanism to produce the majority of FRBs.

4.4.3 Physical scenarios for FRBs

As mentioned above, magnetars are the most likely progenitors of FRBs as they naturally provide the large energies and small size and time-scales necessary to produce the high brightness temperatures observed from FRBs (e.g. Zhang, 2020a). FRB 20200428 has also been observed to originate from the Galactic magnetar SGR 1935+2154 (CHIME/FRB Collaboration et al., 2020b). In this section we briefly discuss the necessary conditions for FRB emission in a magnetar wind, with the full parameter space and details explored in Chapter 5. In our model, we assume that the required Alfvén waves for the non-resonant interaction are produced by a quake or similar instability of the central magnetar (e.g Blaes et al., 1989; Beloborodov, 2023). As the magnetic field of the Alfvén wave decreases more slowly than the magnetospheric field, the relative strength of the turbulence grows as $\eta = \eta_*(R/R_*)^{3/2}$ (e.g. Yuan et al., 2020). Here, η_* is the turbulence level at the magnetar surface. To reach values of $\eta > 0.1$ at the light cylinder therefore requires only small initial values of $\eta_* > 3 \times 10^{-7} P^{-3/2} R_{*,6}^{3/2}$, suggesting that the turbulence levels needed to form a population inversion are achievable in this scenario.

The Alfvén waves propagate outwards before interacting with a relativistic plasma, with the resulting non-resonant interaction producing a population inversion and SME. In order for this to produce an FRB signal, the interaction must occur in a region of parameter space where a high value of f_{inv} can be achieved on a time-scale compatible with the dynamical time-scales discussed in Sec. 4.4.2. The plasma parameters must also allow a peak SME frequency appropriate for FRBs, whose signals have primarily been detected in the GHz band with frequencies ranging from 110 MHz (Fedorova & Rodin, 2019; Pleunis et al., 2021a; Pastor-Marazuela et al., 2021) to 8 GHz (Gajjar et al., 2018).

The plasma parameters required to achieve such SME frequencies depend on the magnetisation of the plasma. At higher magnetisations of $\sigma > 1$, the maser's peak frequency is $\omega_m \sim \Omega\gamma_{av}^{-1}$ (Lyubarsky, 2021). If the plasma where the emission occurs is moving towards the observer with Lorentz factor γ_w, this results in a required magnetic field of $B_0 \sim 180\nu_9\gamma_{av}$ G (Long & Pe'er, 2025b). Here ν is the FRB frequency in Hz. In order to satisfy $\sigma > 1$, the upper limit on the number density in this regime is $n_{\max} \sim 3.1 \times 10^9\nu_9^2 w^{-1}\gamma_{av}^2\gamma_w^{-2}$ cm^{-3}. On the other hand, when $\sigma < 1$, the peak frequency for SME occurs at $\omega_m \approx \gamma_{av}^{-1/2}\omega_p \min\left\{\gamma_{av}, \sigma^{-1/4}\right\}$ (Sagiv & Waxman, 2002). As ω_m depends only very weakly on the magnetisation, the peak frequency will never be much higher than a few times $\gamma_{av}^{-1/2}\omega_p$. The number density required to produce emission at FRB frequencies is therefore $n \sim 3.1 \times 10^9\nu_9^2\gamma_{av}\gamma_w^{-2}\max\left\{\gamma_{av}^{-2}, \sigma^{1/2}\right\}$ cm^{-3}, with a corresponding upper limit on the magnetic field of $B_{0,\max} \sim 180\nu_9\gamma_{av}\max\left\{\gamma_{av}^{-1}, \sigma^{1/4}\right\}$ G to satisfy $\sigma < 1$. As the values for the magnetic field in the $\sigma < 1$ case and the number density in the $\sigma > 1$ case are both upper limits, a large parameter space is viable for SME.

As the high magnetisation regime produces the largest values of f_{inv} and is less susceptible to plasma instabilities, we first examine a model in this regime by considering Alfvén waves propagating through a relativistic magnetar wind. These winds have typical magnetisations of $\sigma_{wind} \sim 280B_{*,15}^{8/9}R_{*,6}^{24/9}M_3^{-2/3}P^{-2}$ outside the light cylinder radius $R_{LC} = cP/2\pi = 4.8 \times 10^9 P$ cm (Lyubarsky, 2021). Here B_* is the surface magnetic field and M is the pair multiplicity. This magnetisation value is well above σ_1 for all temperatures, and so is in the high magnetisation regime with a correspondingly high $f_{inv} \gtrsim 10^{-2}$

at all temperatures examined. Furthermore as f_{inv} is close to constant for all σ in this regime, the precise magnetisation value of the wind does not affect the validity of the mechanism provided that $\sigma_{wind} > \sigma_1$. The required magnetic fields are found outside the light cylinder at typical radii of $R \sim 10^{13-15}$ cm, depending on the parameters involved (Long & Pe'er, 2025b). However, emission radii can occur at much smaller radii for weaker FRBs. The particle number density at these distances is significantly below the upper limits for $n_{\max}$ discussed above, so SME at the appropriate frequencies is viable in this scenario assuming the population inversion has successfully formed.

This model also implies that SME may occur at smaller radii and thus higher frequencies than those observed from FRBs, as the background magnetic field is larger closer to the magnetar. Inside the magnetosphere at $R < R_{LC}$, $\sigma \gg 1$ and so a population inversion with a large energy fraction could possibly be formed. However in this region η will be much smaller than at larger radii outside the light cylinder due to the extremely high $B_0 = 10^{15} B_{*,15} R_{*,6}^3 / R_6^3$ G inside the magnetosphere. These low turbulence levels will not be sufficient to produce any significant change in the particle distribution through this mechanism.

SME at much lower frequencies than FRBs is also not feasible in this model as the Alfvén wave frequency becomes comparable to Ω at larger radii, violating the conditions required for the non-resonant interaction to be dominant as described in Sec. 3.2. The combination of these constraints leads us to conclude that non-resonant interaction between Alfvén waves and a relativistic magnetar wind leads to the appropriate conditions to produce FRBs at R_{FRB}. These limits may also provide information on the magnetar properties (such as period and magnetic field) based on the frequency and luminosity of observed FRB signals.

4.5 Conclusion

In this work, we showed that non-resonant interaction of Alfvén waves with a relativistic plasma can significantly alter the particle distribution for temperatures in the range $10^{-2} \leq \theta \leq 3$ and for magnetisations greater than $\sigma \sim 10^{-4}$. We report that a significant fraction of the energy in the particle distribution is contained in the crescent-shaped population inversion, with peak values of $f_{inv} \sim 0.1$ reached at magnetisations of $\sigma \gtrsim 10$ for temperatures of $\theta \geq 10^{-1}$. At the lower temperature of $\theta = 10^{-2}$, the peak magnetisation is lower at a value of $\sigma \sim 0.1 - 1$, but similar energy fractions are obtained. In the intermediate magnetisation regime with lower magnetisations of $\sigma < \sigma_1 \sim 10^{-1}$ the energy fraction decreases as the magnetisation decreases, with $f_{inv} \propto \sigma$, before dropping sharply at a cut-off magnetisation of $\sigma = \sigma_2 \sim 10^{-4}$. The higher fractions of energy in the population inversion at high magnetisations across all temperatures, as well as reduced susceptibility to other instabilities and the clear formation of the crescent, leads us to suggest that this regime is the most relevant for astrophysical scenarios such as FRBs.

Significant turbulence levels of $\eta \gtrsim 0.1$ are required to sufficiently distort the initial distribution, with the value of η needed increasing with temperature and at reduced magnetisations. The time-scale for the formation of the population inversion depends linearly on Γ^{-1}, but only weakly on the final turbulence level. In all cases the time-scale is therefore approximately $t \sim \Gamma^{-1}$ s. These values are compatible with the magnetar period and the light-crossing time-scale for all parameters. We have also demonstrated that the parameters at which the population inversion can form through non-resonant interactions are achievable in the magnetar wind, and can lead to SME at the appropriate frequencies for FRBs

Chapter 5

Fast radio bursts from synchrotron maser emission in the magnetar wind

5.1 Introduction

In the previous chapters, it has been shown that non-resonant interactions between Alfvén waves and a plasma can result in pitch-angle scattering that produces a crescent-shaped population inversion over a wide range of temperatures $\theta = \frac{k_B T}{m_e c^2} \leq 3$. The population inversion forms more efficiently at higher magnetisations of $\sigma = \frac{B'^2}{4\pi w m_e c^2} \gtrsim 1$ for temperatures greater than $\theta \sim 10^{-2}$ (Long & Pe'er, 2025a), where B' denotes the magnetic field in the plasma rest frame and w is the proper specific enthalpy density.

While the works on which these chapters are based (Long & Pe'er, 2023, 2025a) establish the physical basis for associating FRBs with non-resonant interaction between Alfvén waves and plasma, a complete physical scenario that could link FRBs with known objects such as magnetars is still lacking. In this chapter we therefore propose such a model and examine the conditions needed for producing the detected FRB signal. As we show below, FRBs can be produced through non-resonant interactions between Alfvén waves and the relativistic magnetar wind. These interactions produce a crescent-shaped population inversion capable of supporting SME.

To recap the overall framework of the model, there are four main stages:

1. A starquake occurs, generating Alfvén waves that are emitted from the surface of a magnetar.
2. These waves propagate into the magnetar wind.
3. In the wind, non-resonant interactions occur between the Alfvén waves and the wind plasma, resulting in a crescent-shaped population inversion.
4. This population inversion is capable of supporting SME, which amplifies EM waves and produces the FRB.

While the previous chapters have focused on stage 3, i.e. the formation of the population inversion, in this chapter we investigate in more detail the other stages of the process. Therefore, this chapter is organised as follows. In Sec. 5.2 we describe the FRB model, detailing the parameters of the magnetar wind and establishing the parameter space where SME can occur. These results are used to constrain the magnetar and wind properties in Sec. 5.3. Sec. 5.4 describes how the model can explain FRB 20200428, the only FRB with a confirmed magnetar origin. Sec. 5.5 contains the discussion, and finally the results are summarised in the conclusion in Sec. 5.6.

5.2 Model

Magnetars are widely considered the leading progenitors of FRBs due to their large reserves of magnetic and rotational energy and compact scales (e.g. Zhang, 2020a). This link has been strengthened by FRB 20200428, which originates from the Galactic magnetar SGR 1935+2154 (CHIME/FRB Collaboration et al., 2020b; Bochenek et al., 2020). The surface magnetic field B_* of magnetars is extremely high, with typical values of $B_* \sim 10^{14-15}$ G (e.g. Kaspi & Beloborodov, 2017). The magnetar is surrounded by a highly magnetised magnetosphere in which $B \propto R^{-3}$. This closed magnetosphere extends to the light cylinder radius $R_{LC} = cP/(2\pi) = 4.8 \times 10^9 P$ cm, where P is the rotational period of the magnetar (Goldreich & Julian, 1969). The magnetic field at this radius is therefore $B_{LC} = B_* R_*^3 R_{LC}^{-3} = 9 \times 10^3 \mu_{33} P^{-3}$ G. Here, R_* is the magnetar radius, $\mu \sim B_* R_*^3$ is the magnetic moment of the neutron star. We have assumed typical values of $B_* = 10^{15}$ G and $R_* = 10^6$ cm. Beyond the light cylinder, the magnetic field lines open and electron-positron pairs are ejected from the magnetosphere to form a magnetar wind. The magnetic field in the wind is dominated by the azimuthal component $B_\phi \propto R^{-1}$ (e.g. Cerutti & Beloborodov, 2017), so that the field at a radius $R > R_{LC}$ is given by $B(R) = 44 \mu_{33} P^{-2} R_{12}^{-1}$ G. This wind is the region where SME is instigated either by the non-resonant interaction of Alfvén waves with the wind plasma (Long & Pe'er, 2025a) or by the presence of plasma ejected in a flaring event, as we show in detail below. Such SME can result in the production of an FRB.

The wind is launched at the light cylinder, where the magnetisation is $\sigma_{LC} = B_{LC}^2/(4\pi n m_e c^2) = B_{LC}^2 R_{LC}^2/(\dot{N} m_e c)$ in the case of a cold plasma, with n denoting the total particle density and $\dot{N}$ denoting the particle flux. This flux can be estimated as $\dot{N} \sim 3 \times 10^{39} \mathcal{M}_3 \mu_{33}^{2/3} P^{-1}$ s^{-1} (Beloborodov, 2020), resulting in a magnetisation of $\sigma_{LC} \sim 3 \times 10^4 \mu_{33}^{4/3} \mathcal{M}_3^{-1} P^{-3}$. Here, $\mathcal{M}$ is the pair multiplicity. The wind is initially accelerated linearly with radius by fast magnetosonic waves until the flow reaches the fast magnetosonic surface, at which its bulk Lorentz factor is $\gamma_{fms} \sim \sigma_{LC}^{1/3}$. Acceleration beyond this point is slower, with the wind reaching an asymptotic Lorentz factor of $\gamma_w \sim 3\sigma_{LC}^{1/3}$ (Michel, 1969; Beskin et al., 1998).

The wind far from the equator is expected to be relatively cold ($\Delta\gamma_w/\gamma_w \ll 1$) (Beloborodov, 2020). Closer to the equator reconnection in the striped wind may result in more efficient acceleration and heating, with Lorentz factors of up to $\gamma_w \sim \sigma_{LC}$ possibly being achieved (Lyubarsky & Kirk, 2001). Although the details of the wind parameters are only estimates due to the uncertainties in the efficiencies of the various dissipation processes and in the value of the pair multiplicity, magnetar winds of this type have magnetisations of $\sigma \geq 1$ and are highly relativistic ($\gamma_w \gg 1$) at large radii $R \gg R_{LC}$. It is also likely that an enhanced pre-flare wind (Beloborodov, 2020) or the impact of the starquake (e.g. Sharma et al., 2023) will perturb the magnetic field configuration in the magnetosphere, which may result in enhanced magnetic fields in the wind region itself.

In order for a population inversion to form in such a wind through non-resonant interactions, Alfvén waves from the central magnetar must propagate through the magnetosphere to the emission region. Results from Long & Pe'er (2025a), which are discussed in Chapter 4, show that the ratio of the energy density of the Alfvén waves to the background magnetic field, $\eta = B_W^2/B^2$, must have a magnitude of $\eta \gtrsim 0.1$ at the emission site for a significant population inversion to form. Starquakes, which occur due to shear oscillations of the magnetar crust, can launch the required Alfvén waves into the inner magnetosphere (Blaes et al., 1989; Thompson & Duncan, 1996). A small fraction of the starquake energy is transmitted to the waves, which have an initial relative energy density of $\eta \ll 1$. However, as discussed in Sec. 4.4.3, the magnetic field of the Alfvén wave decreases more slowly than the background field in the magnetosphere. Therefore, the relative strength of the turbulence grows with radius as $\eta(R) = \eta_*(R/R_*)^{3/2}$ (e.g. Yuan et al., 2020). To reach values of $\eta > 0.1$ at the light cylinder therefore requires only small initial values of $\eta_* > 3 \times 10^{-7} P^{3/2} R_{*,6}^{3/2}$.

The most natural growth rate of the Alfvén waves from the starquake is $\sim \chi c/R_*$, as discussed in Sec. 4.4.2. This corresponds to a time-scale of $t_A \sim \chi R_*/c \sim 10^{-5}\chi^{-1} R_{*,6}$ s, though the period of the star is another important physical time-scale in the system. In other words, the turbulence level η reaches its asymptotic value at $t \sim t_A$. This is also the time-scale for the formation of the population inversion, as it has been shown for both the non-relativistic (Wu & Yoon, 2007; Yoon et al., 2009) and relativistic (Long

& Pe'er, 2025a) cases that the asymptotic distribution depends only on the turbulence level for a given set of parameters. This scale is much smaller than the typical length scales of the magnetar wind, in which $B \propto R^{-1}$ for $R \gg R_{LC}$.

5.2.1 Parameter space for SME

Growth rate calculation - general considerations

In the presence of a population inversion, electromagnetic waves can resonate with these particles and become amplified, resulting in maser emission. The modes in question are typically either the ordinary or extraordinary electromagnetic wave modes, as discussed in Sec. 2.3.1. An example of a dispersion relation for these modes in a magnetised plasma is shown in Fig. 2.1b for propagation perpendicular to the magnetic field. To briefly summarise the analysis in Chapter 2, the ordinary mode has a cut-off at $\omega = \omega_p$, while the extraordinary mode has a cut-off at $\omega = \left(\omega_p^2 + \Omega^2\right)^{1/2}$ and a resonance at $\omega = \Omega$ (e.g. Iwamoto, 1993), where $\omega_p = \sqrt{4\pi n e^2/m_e}$ is the plasma frequency and $\Omega = eB/m_e c$ is the cyclotron frequency. The extraordinary mode has upper and lower branches, which we refer to as the fast and slow branches respectively. The wave frequency has real and imaginary components such that $\omega = \omega_r + i\omega_i$. SME occurs when the imaginary part of the frequency, the growth rate ω_i, is positive. As masing is a resonant process, the non-resonant Alfvén waves will not be amplified. That is, the Alfvén waves will create the population inversion, which in turn will provide the energy to amplify EM waves and produce the FRB signal. We analyse the conditions required for successful maser emission below.

To simplify the calculation of the growth rate we follow the method described in Sec. 5.2.1. We assume that the emitted waves propagate through a thermal plasma (denoted by the subscript 0), and that the inverse population of energetic electrons (subscript e) only affects the growth rate of the waves. We do not expect the peak frequency to be significantly altered by this assumption, although the precise values of the growth rate will change. The growth rate is calculated using the expression (see e.g. Wu, 1985; Stix, 1992),

$$\omega_i = -\frac{\mathrm{Im}(\Lambda)}{\frac{\partial}{\partial\omega}(\mathrm{Re}(\Lambda_0))}. \tag{5.1}$$

Here $\Lambda = \det \mathbf{\Lambda}$, and Λ_0 refers to the thermal plasma, while Λ contains the contributions from both the thermal and energetic particles. The components of the dispersion relation $\mathbf{\Lambda}$ are given by

$$\Lambda_{ij} = N_r^2\left(\frac{k_i k_j}{k^2} - \delta_{ij}\right) + \varepsilon_{ij}, \tag{5.2}$$

with N_r denoting the refractive index, k the wavenumber, δ_{ij} the Kronecker delta function and ε the dielectric tensor. The full details of this calculation and the terms involved are provided in Sec. 2.3 of Chapter 2. In general, positive growth will be achieved for a range of wavenumbers, as shown in Fig. 5.1, which displays the first 10 harmonics of both the ordinary and slow extraordinary modes for $\theta = 10^{-2}$ and $\sigma = 10$. For this set of parameters there is no overall positive growth for the fast extraordinary mode. As the signal grows exponentially, the fastest growing mode will dominate the process. We designate the real part of the frequency of this mode as the emission frequency ω_m and the growth rate of the mode as Γ_i. All calculations are carried out in the rest frame of the plasma.

We calculate Γ_i as well as the peak emission frequency ω_m for temperatures in the range $10^{-3} \leq \theta \leq 3$ and magnetisations $\sigma > 1$. The peak emission frequency is typically $\omega'_m \sim \zeta\Omega'$, where ζ is a temperature and magnetisation dependent numerical factor whose value is determined by the dominant mode of emission [1] and Ω' is the cyclotron frequency as measured in the plasma rest frame, given by $\Omega' = eB'/m_e c$. Throughout this chapter, primed quantities are measured in the plasma rest frame, while unprimed quantities are measured in the observer's frame.

[1] Due to the overlap of modes and relativistic effects ζ does not have integer values.

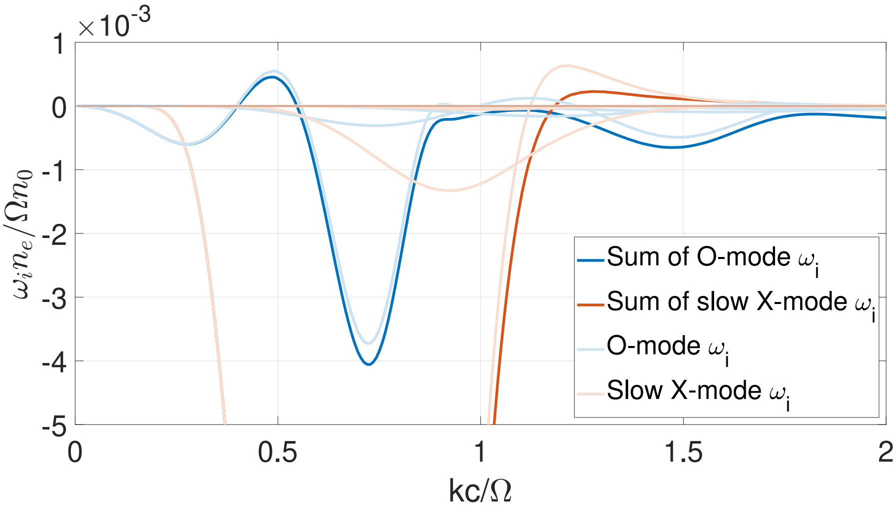

Figure 5.1: The growth rate ω_i normalised to the cyclotron frequency and density ratio for the first 10 harmonics of the O- and slow X-modes, with the majority of the contribution coming from the first 3 harmonics in both cases. The results are for a crescent-shaped distribution with initial temperature $\theta = 10^{-2}$, $\sigma = 10$ and turbulence level $\eta = 1$. The individual ordinary mode harmonics are shown as faint blue lines, with the sum over all harmonics shown as the solid blue line. The same is the case for the extraordinary mode harmonics which are shown in orange. The fastest growing wavenumber for the O-mode occurs at $k \sim 0.48\Omega/c$, while for the slow X-mode it is found at the higher wavenumber of $k \sim 1.27\Omega/c$. The range of wavenumbers where the growth rate is positive is broadened due to the temperature of the distribution in comparison to a cold scenario. The overlap of harmonics due to this broadening acts to reduce the growth rate, especially for higher harmonics.

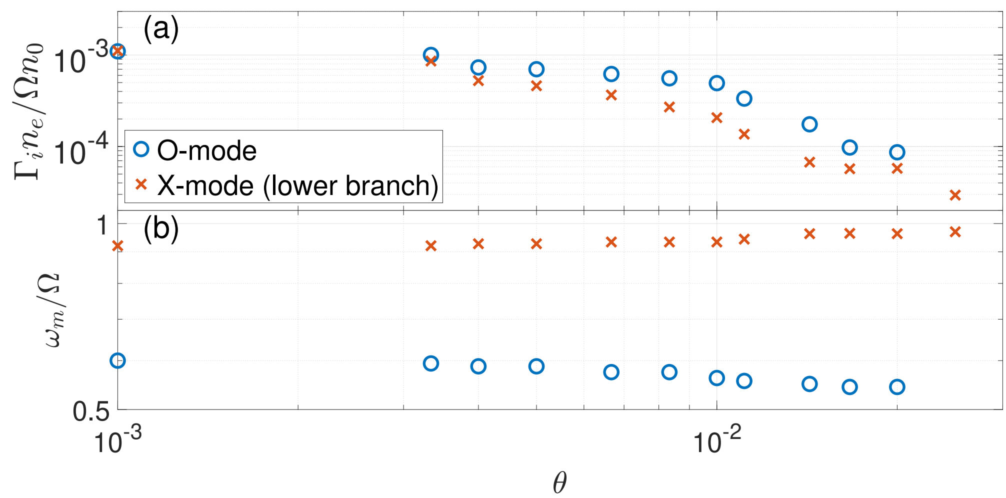

Figure 5.2: Growth rate and emission frequency as a function of temperature: **Panel (a)** shows the growth rate Γ_i normalised to the cyclotron frequency and density ratio for $\sigma = 10$ and $\eta = 1$, while **panel (b)** shows the peak emission frequency ω_m, also normalised to the cyclotron frequency. The ordinary mode is shown by blue 'o's and the slow extraordinary mode (lower branch) by orange 'x's. The decrease in growth rate with increasing temperature is clearly visible. For temperatures of $\theta > 0.02$ no maser emission occurs for the O-mode, while the emission in the X-mode continues to slightly higher temperatures of $\theta \sim 0.025$. Above these temperatures no growth was found. At this magnetisation the O-mode is dominant at temperatures of $\theta \gtrsim 10^{-3}$, at which point the growth rates become comparable. In all cases the maximum growth rate is found at a propagation angle of $\pi/2$.

Formation of the population inversion and resulting growth rates

In our model, the Alfvén waves interact with the particles in the wind, which are assumed to have an initial Maxwell-Jüttner distribution with temperature θ. This thermal distribution does not result in any maser emission as it lacks a population inversion. The non-resonant interaction deforms the initial distribution into a crescent-shaped distribution with enhanced kinetic energy and a population inversion for $p_\parallel > 0$ as shown in Chapters 3 and 4 (Long & Pe'er, 2023, 2025a). Examples of the evolution of the distribution from no turbulence to a turbulence level of $\eta = 1$ can be seen in Figs. 3.2 and 4.1. As described above, this occurs on a time-scale of $t \sim 3.3 \times 10^{-5} \chi R_{*,6}$ s.

The normalised growth rates for the crescent distribution at a turbulence level of $\eta = 1$ are shown for varying temperatures and a magnetisation of $\sigma = 10$ in Fig. 5.2a, with the emission frequencies also shown in Fig. 5.2b. These growth rate calculations show that the maser emission is only possible for initial temperatures of $\theta \lesssim 0.02$ in this model, as can be seen in Fig. 5.2a. At higher temperatures, no positive growth rate was obtained for any mode. This temperature restriction is compatible with typical descriptions of the magnetar wind, which, as described above, is modelled as a cold pair plasma moving relativistically (Beloborodov, 2020). In order for a given wave mode to have a positive growth rate, the mode must primarily resonate with particles in the population inversion, i.e. those located in the region of momentum space where $\partial F/\partial p_\perp > 0$. If the wave mode is also in resonance with particles where $\partial F/\partial p_\perp < 0$, absorption rather than growth will occur, resulting in damping of the waves. At higher temperatures, the width of the particle distribution results in the resonance ellipses for a given wave mode interacting with regions of $\partial F/\partial p_\perp < 0$ that outweigh any growth from the population inversion. This means that even though there is still an inverse population of energetic particles, the contribution to wave growth from these particles is insufficient to overcome the damping effects of the rest of the distribution. Some example resonance ellipses are presented in Appendix C.

The dominant mode of emission depends on both the magnetisation and temperature. We show the normalised growth rates and emission frequencies as a function of σ for $\theta = 10^{-2}$ in Fig. 5.3a and 5.3b. At lower magnetisations of $\sigma \lesssim 3 - 30$ the lower branch of the extraordinary mode (the 'slow' mode) dominates, as shown in Fig. 5.3a. The slow extraordinary mode is a trapped mode, and thus cannot be observed unless mode conversion occurs, as has been proposed for various phenomena such as solar coronal emission (e.g. Khomenko & Cally, 2012). At higher magnetisations the ordinary mode dominates, with the crossover magnetisation increasing as the temperature decreases. Emission from the upper branch of the extraordinary mode is never favoured for the parameters examined because its frequency is always higher than the cyclotron frequency. Particles in the population inversion

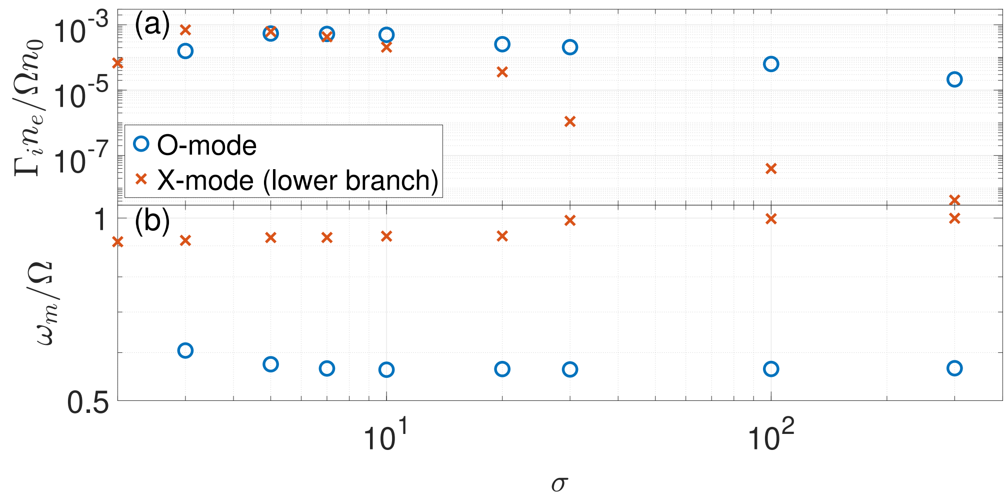

Figure 5.3: Growth rate and emission frequency as a function of magnetisation: **Panel (a)** shows the growth rate Γ_i normalised to the cyclotron frequency and density ratio for $\theta = 10^{-2}$ and $\eta = 1$, while **panel (b)** shows the peak emission frequency ω_m, also normalised to the cyclotron frequency. The ordinary mode is shown by blue 'o's and the slow extraordinary mode (lower branch) by orange 'x's. The decrease in growth rate with increasing magnetisation due to the reduced number density is clearly visible. The O-mode is dominant at magnetisations of $\sigma \gtrsim 5$ for this temperature, with no O-mode growth present for $\sigma < 2$. The crossover value increases with decreasing initial temperatures. In all cases the maximum growth rate is found at a propagation angle of $\pi/2$.

have relativistic momenta and hence lower gyration frequencies, which results in less efficient interactions with the upper branch of the X-mode.

As can be seen in Fig. 5.1, the slow extraordinary mode has positive growth in regions of $k \gtrsim \Omega/c$, corresponding to emission frequencies of $\omega_m > 0.9\Omega$ (see the dispersion relation presented in Fig. 2.1b and the results for ω_m in Fig. 5.2b and 5.3b). In contrast, the O-mode favours growth at lower frequencies of $\omega_m \sim 0.55 - 0.6\Omega$, which corresponds to resonance ellipses of greater radii in momentum space (see the factors of $\frac{n\Omega}{\omega_r}$ in Eq. (2.52)). This implies that O-mode growth is most efficient when the waves resonate with particles of higher momenta. As the ordinary mode has a lower cut-off at $\omega/\Omega = \omega_p/\Omega \sim \sigma^{-1/2}$, the growth rate of the O-mode is reduced at lower magnetisations of $\sigma \lesssim 5$, resulting in the mode becoming less dominant in this region of the parameter space, as can be seen in Fig. 5.3a. For both the O and X-modes, the normalised growth rate (Γ_i/Ω) decreases with increasing magnetisation for $\sigma \gtrsim 10$ due to the decreasing number density, as can be seen in Fig. 5.3a. The growth rate also decreases as the temperature increases due to the increased width of the distribution (and resulting overlap of modes), as well as the lower gradients. In all cases, modes propagating perpendicularly to the background magnetic field show the highest growth rates, as seen in similar non-relativistic scenarios (Zhao et al., 2013).

For perpendicular propagation, the electric field of an ordinary mode wave is parallel to $\mathbf{B}$. As such, its behaviour only depends on the parallel element of the dispersion relation (i.e. the χ_{zz} terms in Λ_{zz} in Eq. (2.49)). This term is proportional to $p_{\parallel}^2$. As a result, the O-mode primarily extracts energy from the 'arms' of the crescent distribution because of the larger parallel momentum in this region, leading to lower emission frequencies due to relativistic effects. Furthermore, as the magnitude of this term depends on the spread of the distribution in the parallel direction, it becomes relatively weaker at low temperatures. As can be seen in Fig. 3.2, the width of the population distribution does not change substantially in the parallel direction due to the non-resonant interaction. In contrast, the perpendicular momentum increases dramatically. The perpendicular momentum of the particles at $\eta = 1$ is dominated by the energy gained from the Alfvén waves rather than the initial thermal energy. As the X-mode waves have an electric field perpendicular to $\mathbf{B}$, they depend only on the χ_{yy} term in Eq. (2.49)[2]. As this term is proportional to $p_\perp^2$, this results in a relative strengthening of the X-mode relative to the O-mode at lower temperatures. This can be seen in Fig. 5.3a, where the growth rates become comparable at $\theta \sim 10^{-3}$.

To examine the effect of the turbulence level on SME, in Fig. 5.4a we plot the normalised growth rate as a function of η for an initial temperature of $\theta = 10^{-3}$ and magnetisations of $\sigma = 10$ and $\sigma = 100$. Fig. 5.4b shows the corresponding normalised emission frequencies. For both the O-mode and lower branch of the X-mode the growth rate decreases as the turbulence level decreases. This is primarily due to the less pronounced population inversion as η decreases, as can be seen in Fig. 3.2. However, the growth rate only shows a very slight reduction for the O-mode at a turbulence level of $\eta \gtrsim 0.2$. The emission frequency is also affected by the value of η. As the distribution spreads to higher momenta as the turbulence level increases, the emission frequency decreases due to the reduced gyration frequency $\propto \gamma^{-1}$. This can clearly be seen in both the O-mode and slow X-mode results.

[2] The convention $k_y = 0$ has been used throughout Sec. 2.3, hence why the X-mode wave depends only on Λ_{yy} and not Λ_{xx}.

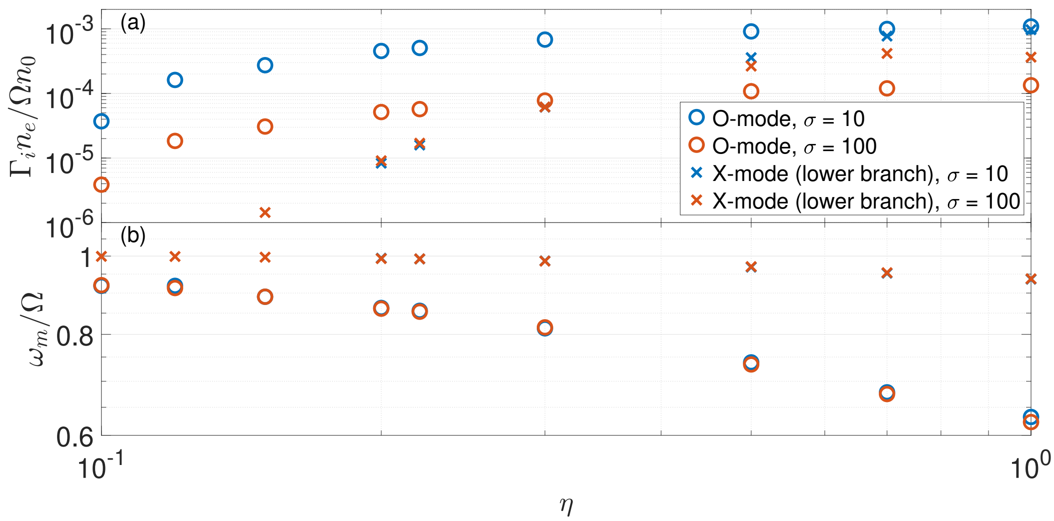

Figure 5.4: Growth rate and emission frequency as a function of η: **Panel (a)** shows the growth rate Γ_i normalised to the cyclotron frequency and density ratio for $\theta = 10^{-3}$ and at magnetisations of $\sigma = 10$ (in blue) and $\sigma = 100$ (in orange), while **panel (b)** shows the peak emission frequency ω_m at the same magnetisations. ω_m is also normalised to the cyclotron frequency. The ordinary mode is shown by 'o's and the slow extraordinary mode (lower branch) by 'x's. The growth rate steadily decreases with decreasing turbulence due to the less pronounced population inversion. The O-mode is dominant at lower turbulence levels. In all cases the maximum growth rate is found at a propagation angle of $\pi/2$.

5.3 Constraints

To examine the emission region, we combine the constraints on the allowed parameter space for SME determined above with three further constraints derived from observed FRB parameters and physical considerations. These are (i) the observed FRB frequency; (ii) the FRB time-scale; and (iii) the requirement that the emission occurs in a region smaller than the coherence length scale of the magnetic field. This is necessary to ensure that the background field and emission frequency do not change substantially across the masing region.

5.3.1 Frequency

FRBs are primarily detected in the GHz band, with individual signals observed from as low as 110 MHz (Fedorova & Rodin, 2019; Pleunis et al., 2021a; Pastor-Marazuela et al., 2021) up to 8 GHz (Gajjar et al., 2018). These observations can be used to constrain the required magnetic field for SME and hence the radius from the magnetar. As shown in Sec. 5.2.1, the peak frequency for SME is $\omega'_m = \zeta\Omega'$ in the wind frame. Presuming the relativistic wind and emission are oriented towards the observer, this corresponds to a required magnetic field of

$$B = \frac{\pi\nu}{b\zeta}\frac{m_e c}{e} \sim 179 b^{-1}\zeta^{-1}\nu_9 \text{ G}, \tag{5.3}$$

for GHz frequencies. The term

$$b = \gamma_w B'/B = \sqrt{\frac{\gamma_w^2\xi^2 + 1}{\xi^2 + 1}} \geq 1, \tag{5.4}$$

is a factor that accounts for the orientation of the magnetic field, where $\xi = B_r/B_\phi$. In the far wind ($R \gg R_{LC}$), the magnetic field is perpendicular to the bulk velocity of the wind and $b = 1$ as $B'_\perp = B_\perp/\gamma_w$. However, closer to the light cylinder the radial component can still be a sizeable fraction of the total field as $B_r/B_\phi \sim R^{-1}$. This is especially the case at higher latitudes, or where the magnetosphere has been opened and the magnetic field distorted by flaring activity, in which case the radial magnetic field can be significantly increased (Beloborodov, 2020; Sharma et al., 2023).

The required magnetic field is found at radii of

$$R_{FRB} = R_0 \sim 2.46 \times 10^{11} b\zeta\nu_9^{-1}\mu_{33}P^{-2} \text{ cm}, \tag{5.5}$$

providing a direct value for the emission radius. Here, R_0 denotes the emission radius assuming an unperturbed magnetosphere and wind. In the case of a change to the magnetic configuration of the magnetar, R_{FRB} will increase to values larger than R_0 as B will decrease more slowly with radius due to the opened field lines.

5.3.2 Time-scale

The second constraint can be derived by examining the time-scale δt of observed FRBs, which is typically on the order of a few milliseconds (e.g. Zhang, 2020a). For a spherical or conical shell moving relativistically towards the observer, the intrinsic time-scale is

$$\delta t \approx \frac{R_{FRB}}{2c\gamma_w^2}. \tag{5.6}$$

This condition imposes an upper limit on the emission radius of the FRB, given by $R_{FRB} \lesssim 6 \times 10^7 \gamma_w^2 \delta t_{-3}$ cm. Therefore, in order for FRB emission to occur in the magnetar wind ($R_{FRB} > R_{LC} = 4.8 \times 10^9 P$ cm), the emitting region must be moving relativistically towards the observer.

5.3.3 Shell size

The final constraint is derived from the condition that the SME must occur over a distance d that is small compared to the coherence length of the magnetic field. This is required so that the background field and hence the emission frequency do not substantially change in the masing region. As $B \propto R^{-1}$ in the magnetar wind, we impose the constraint $d < R$ as an upper limit on the width of the shell where SME occurs.

To estimate the required size of the emitting region, consider that the isotropic equivalent FRB energy, E_{FRB}, is emitted from a spherical shell with width d and inner radius R_{FRB}. The volume of this region is $V' = N/n' = \frac{4\pi}{3}((R_{FRB}+d)^3 - R_{FRB}^3)$, with the total number of particles given by $N = 6.1 \times 10^{44} E_{FRB,39} \gamma_w^{-1} (\gamma_{av}-1)^{-1} f_{inv}^{-1}$. Here f_{inv} is the fraction of the total particle energy that contributes to the SME (Long & Pe'er, 2025a), and γ_{av} is the average Lorentz factor of the particles. The number density at R_{FRB} in the wind frame is $n' \sim 3.1 \times 10^9 w^{-1} \nu_9^2 \gamma_w^{-2} \zeta^{-2} \sigma^{-1}$ cm^{-3}. The volume of the emitting region is therefore

$$V' = 1.97 \times 10^{35} \frac{E_{FRB,39} \gamma_w \sigma l^2 w}{\nu_9^2 (\gamma_{av}-1) f_{inv}} \text{ cm}^3. \tag{5.7}$$

Using the expression for R_{FRB}, the fractional shell width d/R_{FRB} is given by

$$\frac{d}{R_{FRB}} = \left(3.15 \frac{E_{FRB,39} \gamma_w \sigma \nu_9 P^6 w}{\zeta b^3 \mu_{33}^3 (\gamma_{av}-1) f_{inv}} + 1\right)^{1/3} - 1. \tag{5.8}$$

It can be seen that the constraint $d/R_{FRB} < 1$ is satisfied most easily for low periods and high magnetic fields, as both of these result in larger values of R_{FRB}. In particular, the shell width is so sensitive to the period due to its impact on the light cylinder radius.

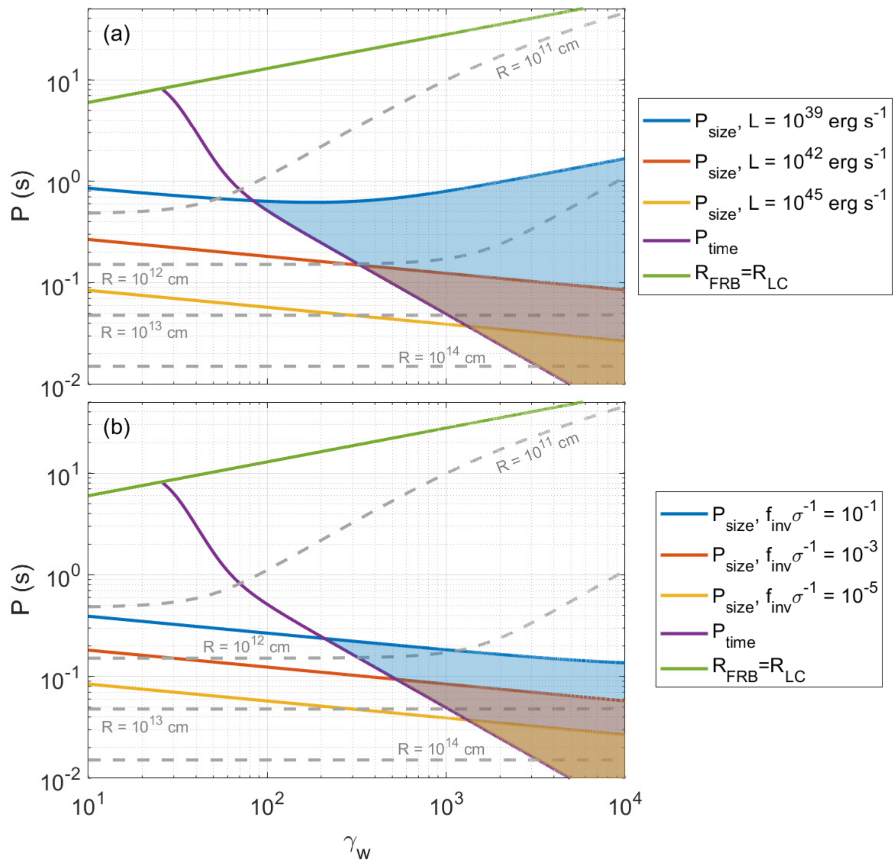

Figure 5.5: The $P - \gamma_w$ parameter space for the range of FRB luminosities. **Panel (a)** shows the parameter space for varying luminosities, with the solid blue, orange and yellow lines showing the upper limits from P_{size} for $L_{FRB} = 10^{39}$ erg s^{-1}, $L_{FRB} = 10^{42}$ erg s^{-1} and $L_{FRB} = 10^{45}$ erg s^{-1} respectively. **Panel (b)** displays parameter space for varying values of $f_{inv}\sigma^{-1}$. In this case, the solid blue, orange and yellow lines show the upper limits from P_{size} for $f_{inv}\sigma^{-1} = 10^{-1}$, $f_{inv}\sigma^{-1} = 10^{-3}$ and $f_{inv}\sigma^{-1} = 10^{-5}$ respectively. As P_{time} is independent of L_{FRB} in both panels, it is shown as a purple line which is valid for all parameters. The shaded region corresponds to the allowed parameter space where an FRB can be produced, with the colours corresponding to the different luminosity values in panel (a), and the different values of $f_{inv}\sigma^{-1}$ in panel (b). Constant emission radii R are shown as dashed grey lines, and the upper limit from the condition $R_{FRB} > R_{LC}$ is shown in green. In all cases $\theta = 10^{-2}$, $\nu = 1$ GHz, $\delta t = 1$ ms, $\mu = 10^{33}$ G cm^3 and $\zeta = 0.6$. In panel (a), $f_{inv}\sigma^{-1} = 10^{-2}$, while in panel (b) the luminosity is $L_{FRB} = 10^{42}$ erg s^{-1}.

5.3.4 Examining the parameter space

To investigate the allowed physical conditions for this model using the above constraints, we examine the $P - \gamma_w$ parameter space. Expressing the constraints as limits on the magnetar period results in

$$P_{size} \lesssim 0.53(b\mu_{33})^{1/2} \left(\frac{f_{inv,-2}\zeta(\gamma_{av}-1)}{E_{FRB,39}\gamma_w \sigma \nu_9 w} \right)^{1/6} \text{ s,} \tag{5.9}$$

$$P_{time} \gtrsim \frac{63.6}{\gamma_w} \left(\frac{b\zeta\mu_{33}}{\nu_9 \delta t_{-3}} \right)^{1/2} \text{ s,} \tag{5.10}$$

where P_{size} is the maximum period allowed by the shell size constraint, and P_{time} is the minimum period allowed by the time-scale constraint. As expected due to the time-scale requirements, FRB emission outside the light cylinder requires quite high Lorentz factors. The minimum Lorentz factor which satisfies both conditions is $\gamma_w \gtrsim 313\zeta^{2/5}E_{FRB,39}^{1/5}w^{1/5}\sigma^{1/5}f_{inv,-2}^{-1/5}(\gamma_{av}-1)^{-1/5}\delta t_{-3}^{-3/5}\nu_9^{-2/5}$, emphasising the need for a relativistic magnetar wind.

Quantities affecting the required number of particles only have an impact on the upper limit P_{size}. Increasing E_{FRB} (or the equivalent luminosity $L_{FRB} \sim E_{FRB}/\delta t$) and σ, or decreasing f_{inv} and γ_{av} all result in a more restrictive limit due to the need for more particles to produce the FRB. However, the dependence on all of these quantities except γ_{av} (and hence the temperature) is very weak. The value of γ_{av} is calculated by integrating over the distribution function, $\gamma_{av} = \int d^3\mathbf{p}\gamma(\mathbf{p})F(\mathbf{p},\eta=1)/\int d^3\mathbf{p}F(\mathbf{p},\eta=1)$. Although the value of γ_{av} for the initial thermal distribution is very low for the temperatures in question (e.g. $\gamma_{av} \sim 1.025$ for $\theta = 10^{-2}$), the non-resonant interactions dramatically increase the average kinetic energy, resulting in values of $\gamma_{av} \gtrsim 1.3$ even for initial temperatures of $\theta = 10^{-3}$. This increase is clear by comparing the initial and final distributions in Figs. 3.2a and 3.2d, or by examining the results presented in Fig. 3.4. It should be noted that l also has a temperature and magnetisation dependence, though the range of allowed values is much smaller than that of other terms, as shown in Sec. 5.2.1. As a

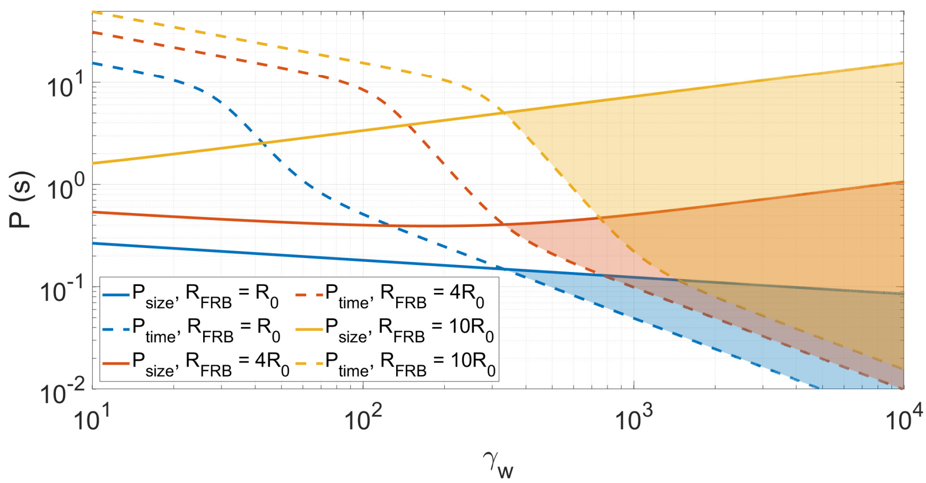

Figure 5.6: The $P - \gamma_w$ parameter space for different magnetic field configurations, showing how the allowed period depends strongly on the neutron star magnetic field. The solid blue, orange and yellow lines show the upper limits from P_{size} for $R_{FRB} = R_0$, $R_{FRB} = 4R_0$ and $R_{FRB} = 10R_0$ respectively. The equivalent lower limits for P_{time} are shown as dashed lines of the same colours. The shaded region corresponds to the allowed parameter space where an FRB can be produced, with the colours corresponding to the different values of R_{FRB}. In all cases $\theta = 10^{-2}$, $\nu = 1$ GHz, $\delta t = 1$ ms, $\mu = 10^{33}$ G cm^3, $L_{FRB} = 10^{42}$ erg s^{-1}, $f_{inv}\sigma^{-1} = 10^{-2}$ and $\zeta = 0.6$.

result, we keep $\zeta = 0.6$ (appropriate for O-mode emission) as an approximate value throughout.

Both limits are proportional to $(b\mu)^{1/2}$, implying that magnetars with higher magnetic fields also need correspondingly higher periods to allow a similarly sized region of parameter space for FRB emission. As the period increases, the light cylinder radius expands, resulting in a lower value of B in the wind, counteracting the influence of the increased surface field. Varying these parameters does not change the minimum γ_w required. The time-scale constraint is naturally more sensitive to both frequency and burst duration, with the limit becoming more constraining as both parameters decrease. As the time-scale is independent of the energetics of the burst, it does not depend on the luminosity or efficiency. The impact of temperature and magnetisation is only through the effect of these factors on the value of ω_m and hence on R_{FRB}.

In general, P_{time} is much more sensitive to variations in the parameters due to the difference in exponent between the two limits.

The allowed parameter space is shown for various scenarios in Figs. 5.5 and 5.6. In all cases b is calculated assuming that $\xi = R_0/R_{LC}$, i.e. that $B_\phi = B_r$ at the light cylinder. This is an approximation, as the true value will depend on both the latitude and the exact configuration of the magnetic field. In Fig. 5.5a the parameter space is displayed for a range of luminosities based on FRB observations (Ravi et al., 2019; Bochenek et al., 2020; Ryder et al., 2023) for $\theta = 10^{-2}$, $f_{inv} = 10^{-2}$ (taken as a typical value based on results in Long & Pe'er (2025a)), $\sigma = 1$, $\zeta = 0.6$, $\delta t = 1$ ms and $\nu = 1$ GHz. Fig. 5.5b uses the same parameters with the FRB luminosity fixed at $L_{FRB} = 10^{42}$ erg s^{-1}. In both these figures $R_{FRB} = R_0$, i.e. an unperturbed magnetosphere is assumed. Also shown is the upper limit imposed by the condition $R_{FRB} > R_{LC}$, though this is less constraining than P_{size} for all the parameters displayed. The regions of the parameter space where $b \neq 1$ can be seen where the lines of constant radii (dashed grey lines) deviate from the horizontal. As expected, this occurs at high Lorentz factors and smaller radii.

From Fig. 5.5a it is clear that weaker bursts have a larger allowed parameter space, extending to both lower Lorentz factors and longer periods. The lower limit is not affected by the change in luminosity as the time-scale is independent of L_{FRB}. Emission radii of $R_{FRB} \sim 10^{13-14}$ cm are favoured for typical FRB luminosities of $L_{FRB} = 10^{42}$ erg s^{-1}, with the radius increasing as the luminosity increases due to the need for more particles to provide the free energy. Fig. 5.5b shows the impact of changing the efficiency of the SME or the magnetisation of the wind. The quantities have been combined for the purposes of presentation, as increasing f_{inv} has the same effect as decreasing σ, with both changing the required volume of particles in the emission region. As expected, decreased efficiency or equivalently increased magnetisation reduces the allowed parameter space by imposing a more constraining upper limit from P_{size}. As in the case of varying L_{FRB}, only the upper limit is affected by the change in $f_{inv}\sigma^{-1}$.

Both cases demonstrate that periods of $P \lesssim 0.1$ s are favoured except for all but the weakest of FRBs, provided that the magnetosphere is unperturbed. In contrast, Fig. 5.6 shows the impact of a distortion to the magnetosphere resulting in increased magnetic field outside the light cylinder, as may be expected both before and after large flares (Beloborodov, 2020; Sharma et al., 2023). To demonstrate this, the allowed parameter space is shown for $R_{FRB} = R_0$, $R_{FRB} = 4R_0$ and $R_{FRB} = 10R_0$. All other parameters are the same as in Fig. 5.5b with $f_{inv}\sigma^{-1} = 10^{-2}$. As both limits contain a factor of $b^{1/2}$ the minimum Lorentz factor is not affected by the change in radius. However, the range of allowed periods shifts to higher values at larger radii, with even moderate increases bringing the preferred period range to the order of seconds.

5.3.5 Emission escape

A further crucial factor when considering FRBs is whether the signal can escape the emission environment without significant damping. Due to the extreme brightness of the FRB signal, the wave strength parameter $a_0 = eE_0/(m_e\omega c)$ may be large ($a_0 > 1$), depending on the distance of the emission region from the magnetar (Luan & Goldreich, 2014). Here, E_0 is the electric field of the wave. In this regime, non-linear effects may result in compression of the wind plasma, taking significant amounts of energy from the radio waves (e.g. Beloborodov, 2021; Golbraikh & Lyubarsky, 2023; Sobacchi et al., 2024b). However, the details of this mechanism are still uncertain, so we do not impose a hard limit on the allowed parameter space. We note that different authors derive different lower limits on the value of R beyond which FRB emission can escape, in the range $R_{damp} \gtrsim 10^{11-12}$ cm, depending on the parameters of the FRB (Sobacchi et al., 2024b; Beloborodov, 2025). In general, these values will not tighten the constraints presented in Sec. 5.3.4 except to lower the upper limits on some of the weaker FRB cases with the largest allowed parameter spaces.

5.4 Application to FRB 20200428

The limits obtained in Sec. 5.3 can be applied to FRB 20200428 since the properties of its associated progenitor, the Galactic magnetar SGR 1935+2154, are known (CHIME/FRB Collaboration et al., 2020b; Bochenek et al., 2020; Mereghetti et al., 2020; Li et al., 2021a). This FRB is extremely weak by typical standards, with a luminosity of $L_{FRB} \sim 3.6 \times 10^{38}$erg s^{-1} (CHIME/FRB Collaboration et al., 2020b; Bochenek et al., 2020). Here, we have taken the inferred luminosity of the STARE2 detection as it was the more luminous burst (Bochenek et al., 2020).

Using the magnetar properties of $P = 3.25$ s and $B_* = 2.2 \times 10^{14}$ G (Olausen & Kaspi, 2014; Israel et al., 2016), we calculate the lower limits imposed on γ_w by the shell size and time-scale constraints. These lower limits are plotted in Fig. 5.7 as a function of $f_{inv}\sigma^{-1}$ for $R_{FRB} = R_0$, $R_{FRB} = 4R_0$ and $R_{FRB} = 10R_0$ with $\theta = 10^{-2}$ and $\zeta = 0.6$. For the unperturbed magnetosphere case (shown by the blue lines in Fig. 5.7), the shell size constraint is more restrictive for all magnetisations and efficiencies. For the majority of the parameter space the lower limit is extremely high, with $\gamma_w > 10^4$ even for $f_{inv}\sigma^{-1} = 0.05$. This likely rules out a completely unperturbed scenario. As R_{FRB}/R_0 increases the allowed parameter space extends to lower values of γ_w and $f_{inv}\sigma^{-1}$, with the crossover point where $\gamma_{w,size} = \gamma_{w,time}$ decreasing such that the time-scale constraint becomes the dominant limit for $R_{FRB} = 10R_0$ even for low values of $f_{inv}\sigma^{-1} \gtrsim 10^{-5}$. These results suggest two possibilities for FRB 20200428 in the context of the model presented in this chapter. In the first case, if the magnetosphere is unperturbed, the emission must originate from an extremely relativistic wind with $\gamma_w > 10^4$ and relatively low magnetisation. On the other hand, if the magnetic field configuration has been altered, emission is possible for a wind across a much more achievable range of efficiencies, magnetisations and γ_w.

This model does not intrinsically produce the observed X-ray emission associated with FRB 20200428 (e.g Mereghetti et al., 2020; Li et al., 2021a). However, the majority of X-ray bursts from SGR 1935+2154 have been ob-

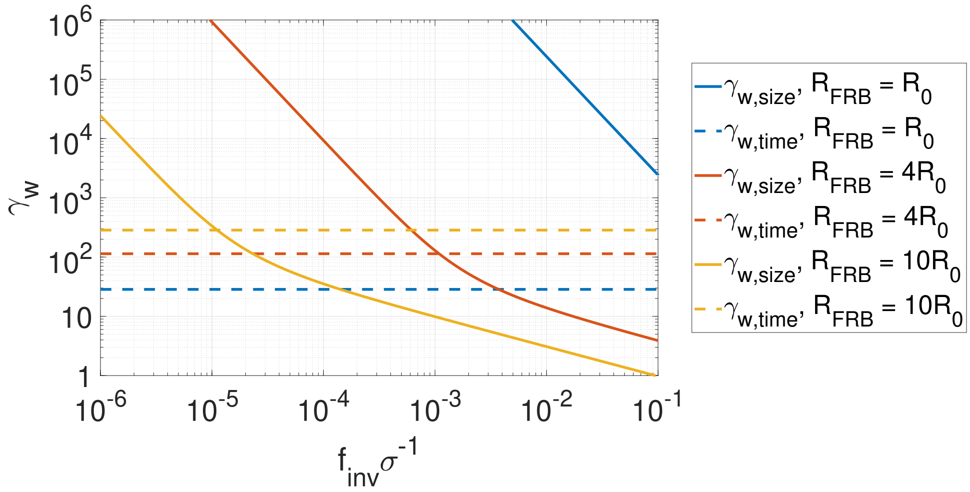

Figure 5.7: The $\theta - \gamma_w$ parameter space for FRB 20200428. The solid blue, orange and yellow lines show the lower limits $\gamma_{w,size}$ for $R_{FRB} = R_0$, $R_{FRB} = 4R_0$ and $R_{FRB} = 10R_0$ respectively. The equivalent lower limits for $\gamma_{w,time}$ are shown as dashed lines of the same colours. In all cases $\theta = 10^{-2}$ and $\zeta = 0.6$.

served not to have associated radio emission (e.g Lin et al., 2020), suggesting the emission mechanism may not be shared. Furthermore, the slight timing differences between the X-ray and radio imply that the emission may occur in different locations, even if the initial source of the energy is the same perturbation of the magnetar (Ge et al., 2023). Previous theoretical works have also demonstrated that the X-ray burst may be emitted within the magnetosphere while the FRB itself is produced in the wind (e.g. Wu et al., 2020; Yu et al., 2021). For these reasons we do not consider the lack of X-ray emission from the non-resonant Alfvén wave interaction to be a serious issue in this case.

5.5 Discussion

5.5.1 FRB and magnetar populations

The allowed parameter space determined in Sec. 5.3 can be compared with the known properties of the magnetar population. Observed magnetars have periods ranging from $P \sim 2 - 12$ s, with a mean value of $P = 6.3$ s. Their surface magnetic fields are $B_* \sim 10^{14} - 2 \times 10^{15}$ G, with a mean value of $B_* = 3.4 \times 10^{14}$ G (Olausen & Kaspi, 2014). Magnetars may also be born with much shorter periods on the order of milliseconds and even larger magnetic fields (e.g. Beniamini et al., 2019; Dall'Osso & Stella, 2022). As can be seen in Figs. 5.5a and 5.5b, the optimal periods found for an unperturbed magnetosphere are at least an order of magnitude lower than the observed magnetar periods. This suggests that either this mechanism may produce FRBs in the environment of younger magnetars with shorter periods, or that flaring activity results in larger emission radii, as shown in Fig. 5.6. These younger magnetars may be necessary to support the energy budget required for very active repeaters (Zhang, 2024). However, as young magnetars spin down very rapidly due to their huge magnetic fields (Beniamini et al., 2019), they may struggle to reproduce repeating FRBs over longer time-scales.

The fraction $\mathcal{F}$ of the observed magnetar population that satisfies the conditions to support FRB emission for various γ_w is shown in Fig. 5.8 below for different R_{FRB}/R_0, assuming the same parameters as used in Fig. 5.6. Here, only magnetars with estimates of both P and B_* in the McGill Online Magnetar Catalog[3] (Olausen & Kaspi, 2014) have been used. The impact of different luminosities is demonstrated by the dashed, solid and dotted blue lines, which show $L_{FRB} = 10^{40}$ erg s^{-1}, $L_{FRB} = 10^{42}$ erg s^{-1} and $L_{FRB} = 10^{44}$ erg s^{-1} respectively. As the allowed parameter space increases with γ_w (see e.g. Fig. 5.5a), so does $\mathcal{F}$, although significant fractions of $\mathcal{F} \gtrsim 0.1$ are available close to the minimum γ_w for both $R_{FRB}/R_0 = 6$ and $R_{FRB}/R_0 = 10$. It is apparent that significant changes to the initial unperturbed magnetic field are necessary for the current observed magnetar population to explain FRBs through this model. However, such changes are expected both in the form of enhanced pre-flare winds (Beloborodov, 2020) and from the impact of the flares themselves (e.g. Sharma et al., 2023). We note that these values of $\mathcal{F}$ are determined for optimal parameters (except for L_{FRB} and θ), and will decrease for less efficient maser emission or higher magnetisations.

[3] `http://www.physics.mcgill.ca/~pulsar/magnetar/main.html`

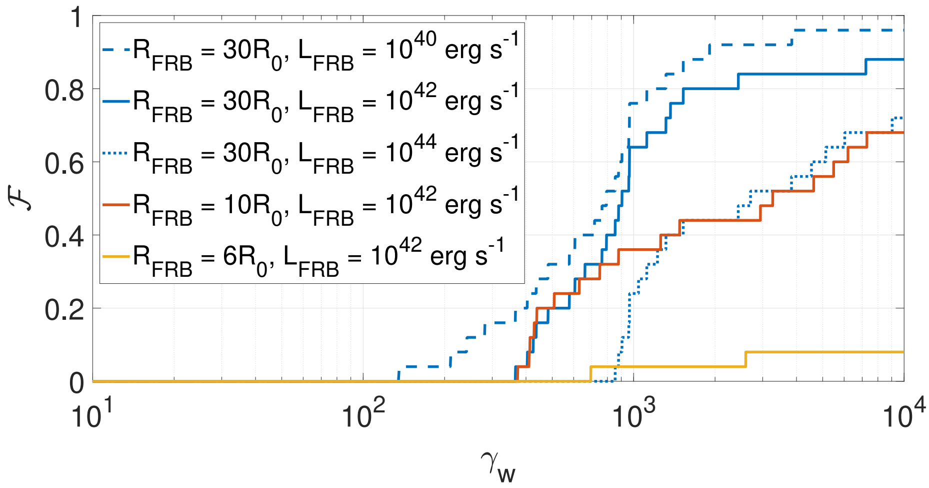

Figure 5.8: The fraction $\mathcal{F}$ of the observed magnetar population that can support FRB emission for a given wind Lorentz factor γ_w. The blue lines denote $R_{FRB} = 30R_0$, with the dashed line denoting a luminosity of $L_{FRB} = 10^{40}$ erg s^{-1}, the solid line showing $L_{FRB} = 10^{42}$ erg s^{-1} and the dotted line showing $L_{FRB} = 10^{44}$ erg s^{-1}. The orange and yellow lines show $\mathcal{F}$ for $R_{FRB} = 10R_0$ and $R_{FRB} = 6R_0$ respectively, in both cases with $L_{FRB} = 10^{42}$ erg s^{-1}. All other quantities have their fiducial values as in Fig. 5.5a.

These results can be compared to the FRB rate, which is $\mathcal{R}_{FRB} \sim 8 \times 10^4$ Gpc^{-3}yr^{-1} for $E_{FRB} > 10^{39}$ erg, with the rate at lower energies poorly constrained (James et al., 2022; Shin et al., 2023). This is $\sim 1\%$ of the magnetar rate, where we have taken a core-collapse supernova rate of $\mathcal{O}(10^4)$ Gpc^{-3}yr^{-1} (Oguri, 2019; Shin et al., 2023) and a typical magnetar lifetime estimate of $\sim 10^4$ yr (Kaspi & Beloborodov, 2017; Oguri, 2019). Furthermore, we have assumed that magnetars make up $\sim 10\%$ of the neutron star population (e.g. Gill & Heyl, 2007; Oguri, 2019). Therefore, in this scenario the values of $\mathcal{F}$ obtained in Fig. 5.8 are sufficiently high to explain the observed FRB population. We note that both the typical magnetar lifetime and the fraction of neutron stars that are magnetars are uncertain.

The difficulty of obtaining very high luminosity bursts ($L_{FRB} \gtrsim 10^{44}$ erg s^{-1}) which require very high γ_w is tempered by their relative rarity. Models of the FRB energy distribution show an upper cut-off on the energy of $E_{FRB} \sim 10^{41-42}$ erg, with rates of $\mathcal{R}_{FRB}(E_{FRB} = 10^{42}\ \mathrm{erg})/\mathcal{R}_{FRB}(E_{FRB} = 10^{39}\ \mathrm{erg}) \lesssim 10^{-4}$, suggesting only a very small fraction of FRBs have such a high energy and luminosity (Hashimoto et al., 2022; James et al., 2022; Shin et al., 2023).

5.5.2 Properties of the SME

The emission is produced by both the ordinary and extraordinary modes, depending on the plasma parameters, with the O-mode favoured at higher magnetisations and temperatures. In contrast, the slow extraordinary mode is favoured at lower magnetisations, with the growth rates of the two modes being roughly comparable at low temperatures. As the slow extraordinary mode is a trapped mode which needs to undergo mode conversion to escape, it is a less likely channel for FRB emission. Although the general conditions for mode conversion are present, namely density and magnetic field gradients, both are over large scales, and a detailed investigation of the mechanism is outside the scope of this work. However, as there is a large part of the parameter space where the ordinary mode is dominant, this does not have a major impact on the overall viability of SME producing FRBs.

Both the O and X-modes are linearly polarised, supporting observations of high degrees of linear polarisation in the majority of FRBs (Qu & Zhang, 2023; Zhang, 2023). However, the mechanism does not intrinsically produce the rapid swings of polarisation angle seen in a small fraction of FRBs (Niu et al., 2024; Mckinven et al., 2025). While this has led to arguments in favour of a magnetospheric origin of FRBs, it has been shown in the case of SME in both non-relativistic scenarios (Wu et al., 2012) and relativistic shocks (Iwamoto et al., 2024) that a change in emission mode and polarisation angle is possible outside the magnetosphere due to the impact of waves (either the pervading Alfvén waves or the SME itself) on the emission process. The impact of the pervading Alfvén waves on the maser instability has also been shown to boost the O-mode growth rate in similar (non-relativistic) scenarios (Wu et al., 2012; Zhao et al., 2013). As we have not included the impact of these waves on the maser instability, this may result in a change in peak frequency for those parameters which currently have higher extraordinary mode growth rates.

The growth rate will also decrease as the masing process continues. The excess energy in the distribution is transferred to the wave, resulting in a reduction of the value of $\frac{\partial F}{\partial p_\perp}$ in the regions of momentum space where resonance occurs. In the absence of continued pumping of the inversion by the Alfvén wave, SME will therefore eventually be quenched.

The results of the growth rate calculations shown in Sec. 5.2.1 display considerable similarities to the results for the efficiency of SME from relativistic shocks, despite the different formation mechanisms for the population inversion. In the shock model, particles that gyrate around the enhanced magnetic field near the shock front form a ring distribution and produce SME (e.g. Alsop & Arons, 1988; Gallant et al., 1992; Amato & Arons, 2006; Plotnikov & Sironi, 2019). In particle-in-cell (PIC) simulations efficiencies of $\sim 10^{-3}\sigma^{-1}$ for $\sigma \gg 1$ were found in such scenarios (Sironi et al., 2021), showing a similar dependence on σ as for the crescent-shaped distribution discussed in this work. Furthermore, the efficiency also drops significantly at temperatures of $\theta \gtrsim 10^{-1.5}$ (Babul & Sironi, 2020), similar to the maximum temperature of $\theta \sim 0.02$ found above. We note that the values of Γ_i and the efficiency values reported in the PIC simulations are not the same physical quantity, as the efficiency is the fraction of total energy emitted by the maser rather than the growth rate. However, we expect the same trends to hold for both.

5.5.3 Other observational constraints

A further observational constraint for at least one FRB (FRB 20221022A) comes in the form of scintillation measurements (Nimmo et al., 2025). The upper limit on the size of the emitting region in this case is $R_{FRB} \sim (0.8 - 5) \times 10^{11}$ cm, where we have used the upper bound on the lateral size of the emission region as obtained by Nimmo et al. (2025). For this particular FRB, this value is quite constraining, and requires very high efficiencies and low magnetisations to satisfy. However, we note that scattering may occur as a result of the signal's propagation through the relativistic magnetar wind, complicating the analysis (e.g. Sobacchi et al., 2022).

While both polarisation swings and scintillation measurements impose tighter constraints on the magnetar wind scenario in comparison with magnetospheric models, importantly wind models avoid major difficulties raised by the potential damping of the FRB (e.g. Beloborodov, 2021; Golbraikh & Lyubarsky, 2023; Beloborodov, 2024). We note that the importance and details of the damping mechanisms are still under debate (e.g. Qu et al., 2022; Lyutikov, 2024).

5.5.4 Alternative FRB scenarios

Magnetars may also be surrounded by a lower magnetisation subrelativistic wind with $\beta_w \lesssim 1$ and $\sigma \lesssim 1$ (Metzger et al., 2019). Here, $\beta_w = v_w/c$ is the normalised wind velocity. In this scenario wind densities of $n \sim 1.6 \times 10^5 \dot{M}_{21} R_{14}^{-2} \beta_{wind}^{-1}$ cm^{-3} are expected. Here, $\dot{M}$ is the mass loss rate, which is normalised to constraints obtained from FRB 20121102, where $\dot{M} \sim 10^{19} - 10^{21}$ g s^{-1} (Margalit & Metzger, 2018). This environment satisfies the constraints for maser emission at a similar radius as the relativistic magnetar wind, $R_{FRB} \sim 7.2 \times 10^{11} \nu_9^{-1} \dot{M}_{21}^{1/2} \beta_w^{-1/2} \gamma_w \gamma_{av}^{-1/2} \min\left\{\gamma_{av}, \sigma^{-1/4}\right\}$ cm. Such a scenario would require a beam of energetic particles to satisfy both the requirements for the FRB energy and for efficient maser emission, as a significant population inversion was only formed for beam distributions at lower magnetisations (see Sec. 3.5.2). In the absence of a relativistic beam, this model is also susceptible to the damping constraints discussed in Sec. 5.3.5. Due to all these caveats, this model is unlikely to produce FRBs.

5.6 Conclusions

In this chapter, we have examined the allowed parameter space for FRBs emitted by SME in relativistic magnetar winds. We consider that the necessary population inversion has been formed by non-resonant interactions between Alfvén waves produced by the central magnetar and the wind. For all parameters, a relativistic wind is required, with minimum Lorentz factors of $\gamma_w \gtrsim 310 l^{2/5} E_{FRB,39}^{1/5} w^{1/5} \sigma^{1/5} f_{inv,-2}^{-1/5} (\gamma_{av} - 1)^{-1/5} \delta t_{-3}^{-3/5} \nu_9^{-2/5}$. Provided that the magnetic field is perturbed by the flaring activity, the allowed periods align with the observed magnetar period distribution. In the case of an unperturbed magnetic field configuration, the typical period required is $P \lesssim 0.1$ s, suggesting that only young magnetars may be viable sources of FRBs in this particular scenario. The emission takes place at typical distances of $R_{FRB} \sim 10^{13-15}$ cm, outside the light cylinder and at a sufficient distance to avoid expected damping mechanisms. This model therefore presents a robust explanation for the production of FRBs in magnetar winds and can be used to probe the physical conditions in the emission region, such as the wind Lorentz factor and magnetisation.

Chapter 6

Summary

In this thesis, we investigated the effect of non-resonant interactions between shear Alfvén waves and a relativistic plasma. We showed that such interactions can produce a crescent-shaped distribution function that is capable of supporting SME and producing FRBs in a relativistic magnetar wind.

In Chapter 3, we describe how we solved the quasilinear kinetic equation governing the process. The resulting effects on the temperature, kinetic energy, and bulk motion were analysed for both Maxwellian and non-Maxwellian distributions. We investigated the behaviour across a wide range of temperatures and magnetisations. The apparent temperature increased preferentially in the perpendicular direction, with significant increases possible even at relativistic temperatures. The initial particle distribution is deformed most strongly at high magnetisations due to the relative strength of the Alfvén waves compared to the initial particle energy. In this regime, a crescent-shaped inversion was found to form, with arms extending to large values of $p_{\parallel}$.

This crescent-shaped particle distribution can provide the necessary population inversion for SME. Therefore, in Chapter 4, we determined the precise parameter space in which such an inversion can form as a result of the non-resonant interaction. We examined the properties of the resulting population inversion and determined the energy available for masing in such a scenario.

A significant fraction of the total energy ($\sim 1\%$) was found to be shifted into the arms of the particle distribution, suggesting that efficient maser emission is possible.

Finally, in Chapter 5, we applied the results from the previous chapters to a specific FRB model. This model consists of an initial starquake, which results in the emission of Alfvén waves from the central magnetar. These waves propagate into the relativistic wind, where they interact non-resonantly with the particles in the wind to form a crescent-shaped population inversion. This population inversion provides the energy to amplify ordinary or extraordinary waves which form the FRB signal. We showed that FRBs can be produced through this mechanism, and determined the necessary properties of both the central magnetar and the wind itself. We calculated the SME growth rate and determined that lower initial temperatures of $\theta \leq 0.2$ were favoured. The wind was shown to require a Lorentz factor of $\gamma_w \gtrsim 310$, and a scenario where flaring has disturbed the magnetosphere was favoured to align with the known magnetar population.

A natural continuation of this work is to extend the analysis to other wave modes, such as kinetic Alfvén waves and magnetosonic waves, both of which may be present in the environments where FRBs are produced. The primary differences in behaviour for these modes will occur due to their distinct dispersion relations and their finite $k_\perp$. The presence of the perpendicular component of the wavevector will introduce extra terms into the quasilinear kinetic equation, while the different dispersion relation will result in changes to the relationships between the I_x terms. The presence of a parallel electric field also allows for the possibility of Landau damping, which may alter the behaviour substantially in some cases.

The constraints on this model will be further refined as more FRBs are detected, particularly if any further bursts are localised to magnetars or other compact objects. Observations of shorter period magnetars, even if not in conjunction with an FRB, will also provide important information and constraints for the unperturbed magnetosphere model discussed in Chapter 5.

Further evidence for separate populations of FRBs may also reveal that some FRBs are produced in the wind, while others, such as those with rapidly varying polarisation angles, are indeed magnetospheric in origin. Regardless of their nature, improved observations will allow more accurate probes of the FRB environment using the limits described in our model.

Appendix A

Comparison to non-relativistic results

To check the accuracy of the numerical solution, we compare our results with the non-relativistic analytical solution in the low turbulence regime (Wu & Yoon, 2007). We first relate the measure of turbulence used in Wu & Yoon (2007) to η as follows. From Eq. (2.8), we have

$$\begin{aligned}\epsilon =& \frac{1}{4n_p k_B T_0}\int dk \frac{B_k^2}{8\pi} \\ =& \frac{\eta B^2}{32\pi n_p \theta m_p c^2} \\ =& \frac{\eta v_A^2}{8\theta c^2}.\end{aligned} \tag{A.1}$$

Fig. A.1a shows the solution for $F(q_\perp, q_\parallel = 0)$ for an initial Maxwellian distribution of $F_0 = \exp\left(\frac{-q_\perp^2 - q_\parallel^2}{2\theta}\right)$ with $\theta = 10^{-4}$. Results are shown as solid lines for $v_A = c/2$ and $v_A = c/10$ at a turbulence level of $\eta = 10^{-3}$. The non-relativistic analytical solutions given by Eq. (2.9) at the same turbulence levels are shown as dashed lines. The results for $F(q_\perp = 0, q_\parallel)$ with the same parameters are shown in Fig. A.1b. In all cases, the numerical and analytical solutions agree. Similar agreement can be seen in plots of the perpendicular temperature and temperature anisotropy shown in Figs. 3.4 and 3.6.

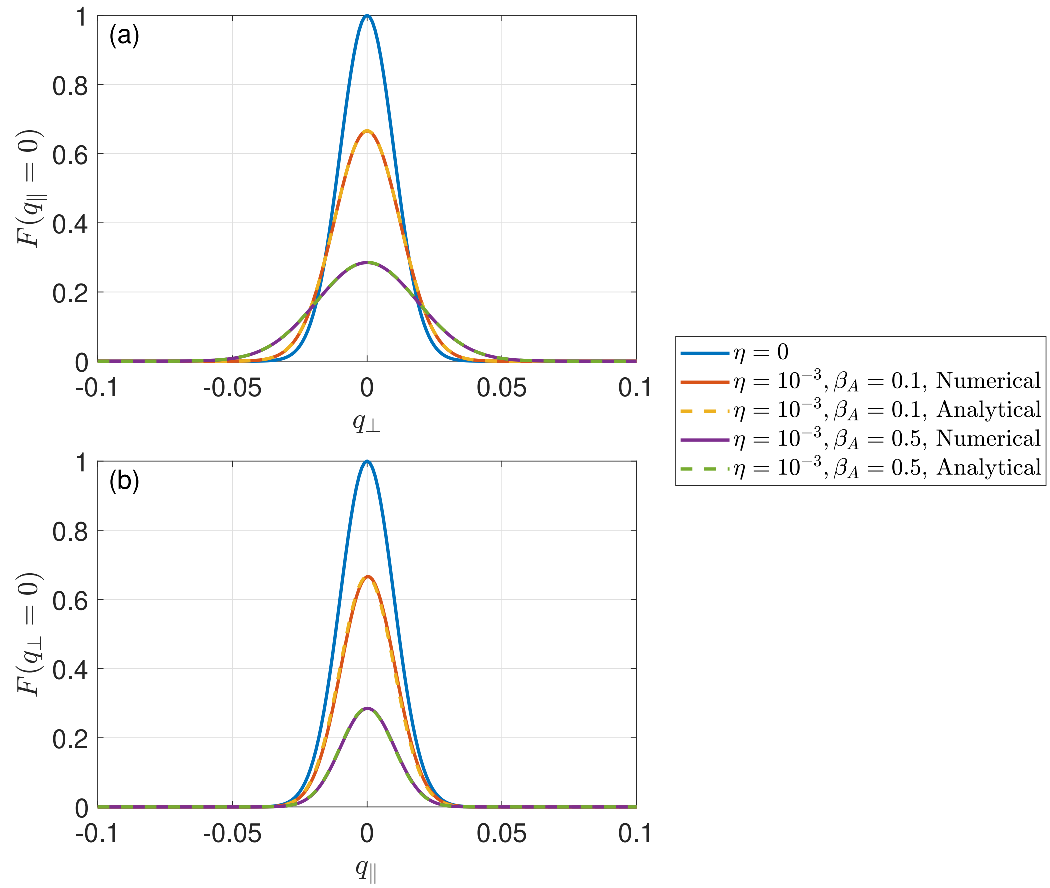

Figure A.1: Comparison between the full solution solved numerically using Eq. (3.5), and the low turbulence non-relativistic solution from Wu & Yoon (2007). **Panel (a)** shows the $F(q_{\parallel} = 0)$ while **panel (b)** shows $F(q_{\perp} = 0)$. In both cases the solid blue line shows the initial distribution with a temperature of $\theta = 10^{-4}$. The solid orange lines show the numerical result at $\eta = 10^{-3}$ for $\beta_A = 0.1$, while the dashed yellow lines show the equivalent analytical solution. The solid purple lines show the numerical result at $\eta = 10^{-3}$ for $\beta_A = 0.5$, and the dashed green lines show the equivalent analytical solution. In all cases, the solutions are in close agreement.

Appendix B

Semi-analytical examination of the terms in the quasilinear kinetic equation

In this section we retrieve some semi-analytical approximations for the ratios of the various terms in Eq. (3.5) in the low and intermediate magnetisation regimes, specifically for $\sigma < \sigma_1$, equivalent to $I_2/I_1 \gg 1$.

B.1 Mixed term

The change in the distribution due to the mixed term, $\left(\frac{\partial F}{\partial t}\right)_{mix}$, for an initial symmetric Maxwell-Jüttner distribution is given by

$$\left(\frac{\partial F}{\partial t}\right)_{mix} = \frac{Ce^{-\theta^{-1}\sqrt{1+q_\parallel^2+q_\perp^2}}q_\parallel q_\perp^2}{\theta\left(1+q_\parallel^2+q_\perp^2\right)^2}\left(1+\theta^{-1}\sqrt{1+q_\parallel^2+q_\perp^2}\right) \times\left(I_1\left(1+q_\parallel^2+q_\perp^2\right)-I_2 q_\parallel\sqrt{1+q_\parallel^2+q_\perp^2}\right), \qquad \text{(B.1)}$$

where C contains all the constants omitted for clarity. Fig. B.1 shows the values of $|q_{\parallel,\max}|$ and $|q_{\perp,\max}|$ as a function of I_2/I_1 for various temperatures, showing that $|q_{\perp,\max}|$ is close to constant, while $|q_{\parallel,\max}| \propto (I_2/I_1)^{-1}$ for large $I_2/I_1 \gg 1$ for all temperatures. It can also be seen that $|q_{\parallel,\max}| \ll 1$ and $|q_{\parallel,\max}| \ll |q_{\perp,\max}|$ in this I_2/I_1 range. Therefore comparing $\left(\frac{\partial F}{\partial t}\right)_{mix,\max}$ at two different values of (I_2/I_1) and $(I_2/I_1)'$ gives

$$\begin{aligned}\frac{\left(\frac{\partial F}{\partial t}\right)_{mix,\max}}{\left(\frac{\partial F}{\partial t}\right)'_{mix,\max}} \approx & \left(\frac{q_{\parallel,\max}}{q'_{\parallel,\max}}\right) \\ & \times \left(\frac{1+q^2_{\perp,\max}-(I_2/I_1)q_{\parallel,\max}\sqrt{1+q^2_{\perp,\max}}}{1+q^2_{\perp,\max}-(I_2/I_1)'q'_{\parallel,\max}\sqrt{1+q^2_{\perp,\max}}}\right). \end{aligned} \tag{B.2}$$

Defining $C_\parallel$ as a constant of proportionality such that $q_{\parallel,\max} = C_\parallel (I_2/I_1)^{-1}$, this expression can be simplified to

$$\begin{aligned}\frac{\left(\frac{\partial F}{\partial t}\right)_{mix,\max}}{\left(\frac{\partial F}{\partial t}\right)'_{mix,\max}} &\approx \frac{C_\parallel (I_2/I_1)'\left(1+q^2_{\perp,\max}-C_\parallel\sqrt{1+q^2_{\perp,\max}}\right)}{C_\parallel (I_2/I_1)\left(1+q^2_{\perp,\max}-C_\parallel\sqrt{1+q^2_{\perp,\max}}\right)} \\ &\approx \frac{(I_2/I_1)'}{(I_2/I_1)}, \end{aligned} \tag{B.3}$$

showing that $\left(\frac{\partial F}{\partial t}\right)_{mix,\max} \propto (I_2/I_1)^{-1}$ for large $I_2/I_1 \gg 1$.

B.2 Parallel terms

In the case of the parallel terms, the maximum value of the parallel advection term $\left(\frac{\partial F}{\partial t}\right)_{\parallel,1}$ is significantly higher than the diffusion term, as is shown in

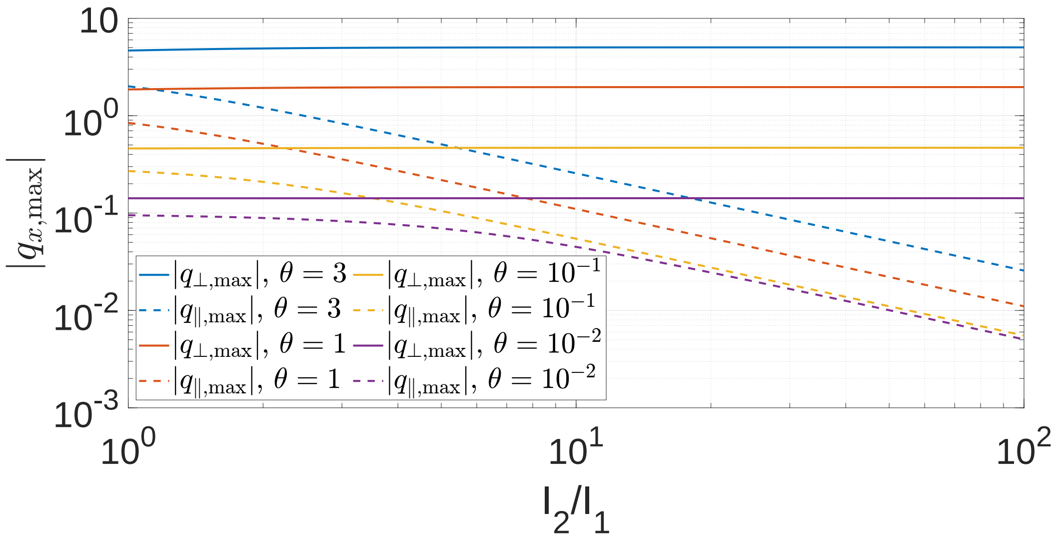

Figure B.1: The values of $|q_{\parallel,\max}|$ and $|q_{\perp,\max}|$ as a function of I_2/I_1 for the mixed term, $\left(\frac{\partial F}{\partial t}\right)_{mix}$. Dashed lines indicate $|q_{\parallel,\max}|$ at different temperatures while solid lines show $|q_{\perp,\max}|$. For large $I_2/I_1 \gg 1$, $|q_{\parallel,\max}| \propto (I_2/I_1)^{-1}$ and $|q_{\perp,\max}|$ is constant.

Fig. 4.7. For an initial symmetric Maxwell-Jüttner distribution, the term is

$$\left(\frac{\partial F}{\partial t}\right)_{\parallel,1} = \frac{Ce^{-\theta^{-1}\sqrt{1+q_\parallel^2+q_\perp^2}}\theta^{-1}q_\parallel}{\left(1+q_\parallel^2+q_\perp^2\right)} \times \left(I_1(2+2q_\parallel^2+3q_\perp^2) - 2I_2 q_\parallel\sqrt{1+q_\parallel^2+q_\perp^2}\right), \tag{B.4}$$

where C contains all the constants omitted for clarity. Fig. B.2 shows the values of $|q_{\parallel,\max}|$ as a function of I_2/I_1 for various temperatures, while $|q_{\perp,\max}| = 0$ for all cases. This allows us to discard all terms containing $q_{\perp,\max}$, resulting in

$$\left(\frac{\partial F}{\partial t}\right)_{\parallel,\max} = \frac{Ce^{-\theta^{-1}\sqrt{1+q_{\parallel,\max}^2}}\theta^{-1}q_{\parallel,\max}}{\left(1+q_{\parallel,\max}^2\right)} \times \left(2I_1(1+q_{\parallel,\max}^2)^2 - 2I_2 q_{\parallel,\max}\sqrt{1+q_{\parallel,\max}^2}\right). \tag{B.5}$$

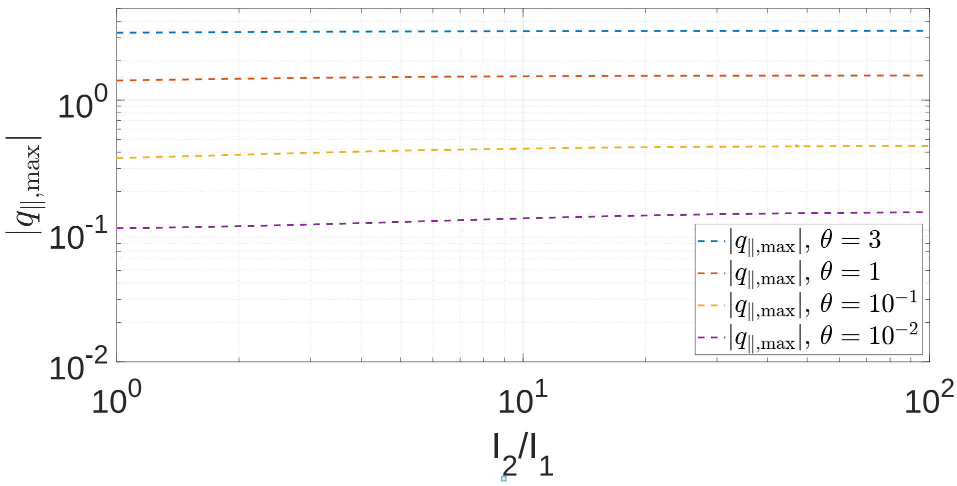

Figure B.2: The values of $|q_{\parallel,\max}|$ as a function of I_2/I_1 for the parallel advection term, $\left(\frac{\partial F}{\partial t}\right)_{\parallel,1}$. $|q_{\perp,\max}| = 0$ for all temperatures displayed. For large $I_2/I_1 \gg 1$, $|q_{\parallel,\max}|$ is approximately constant.

From Fig. B.2, it is clear that $|q_{\parallel,\max}|$ is close to constant for a given temperature for large I_2/I_1. Therefore comparing $\left(\frac{\partial F}{\partial t}\right)_{\parallel,\max}$ at two different values of (I_2/I_1) and $(I_2/I_1)'$ gives

$$\frac{\left(\frac{\partial F}{\partial t}\right)_{\parallel,\max}}{\left(\frac{\partial F}{\partial t}\right)'_{\parallel,\max}} = \frac{(1+q_{\parallel,\max}^2)^2 - (I_2/I_1)q_{\parallel,\max}\sqrt{1+q_{\parallel,\max}^2}}{(1+q_{\parallel,\max}^2)^2 - (I_2/I_1)'q_{\parallel,\max}\sqrt{1+q_{\parallel,\max}^2}}. \tag{B.6}$$

As the ratio $\left|\frac{(1+q_{\parallel,\max}^2)^2}{q_{\parallel,\max}\sqrt{1+q_{\parallel,\max}^2}}\right| = \gamma(q_{\parallel,\max},0)^2/|\beta_{\parallel,\max}| < 15$ for $\theta \leq 3$, the second term is always larger than the first for large values of I_2/I_1 and thus $\left(\frac{\partial F}{\partial t}\right)_{\parallel,\max} \propto I_2/I_1$ for $I_2/I_1 \gg 1$.

B.3 Perpendicular terms

In the case of the perpendicular terms, both the advection and diffusion terms are significant, depending on the magnetisation. For an initial symmetric

Maxwell-Jüttner distribution, the sum of these terms is given by

$$\begin{aligned}\left(\frac{\partial F}{\partial t}\right)_{\perp} = \frac{Ce^{-\theta^{-1}\sqrt{1+q_{\parallel}^2+q_{\perp}^2}}}{\theta^2\gamma^4} & \Big\{ I_1 q_{\parallel}\gamma^2\left(-2q_{\perp}^2\gamma + 4\theta(\gamma^2 - q_{\perp}^2)\right) \\ & + I_2[\theta\gamma q_{\perp}^2(1+q_{\perp}^2) + q_{\parallel}^4(q_{\perp}^2 - 2\theta\gamma) \\ & + q_{\parallel}^2(q_{\perp}^2 + q_{\perp}^4 - 2\theta\gamma)] \\ & + I_3\gamma^2\left(q_{\perp}^4 - 2\theta\gamma(1+q_{\parallel}^2) + q_{\perp}^2(1+q_{\parallel}^2 - 3\theta\gamma)\right)\Big\}. \end{aligned} \tag{B.7}$$

Fig. B.3 shows the values of $|q_{\parallel,\max}|$ and $|q_{\perp,\max}|$ as a function of I_2/I_1 for various temperatures, showing that $|q_{\perp,\max}|$ is close to constant and $|q_{\parallel,\max}| \ll 1$ and $|q_{\parallel,\max}| \ll |q_{\perp,\max}|$ for large I_2/I_1. We can therefore approximate $\left(\frac{\partial F}{\partial t}\right)_{\perp,\max}$ as

$$\begin{aligned}\left(\frac{\partial F}{\partial t}\right)_{\perp,\max} \approx & \frac{Ce^{-\theta^{-1}\sqrt{1+q_{\perp,\max}^2}}}{\theta^2(1+q_{\perp,\max}^2)} \\ & \times \left\{I_2\theta q_{\perp,\max}^2\right. \\ & \left. + I_3(q_{\perp,\max}^2\sqrt{1+q_{\perp,\max}^2} - \theta(2+3q_{\perp,\max}^2)\right\}. \end{aligned} \tag{B.8}$$

Now using the relation $I_3/I_1 = I_1/I_2$, which is true in the linear regime, comparing the value of $\left(\frac{\partial F}{\partial t}\right)_{\perp,\max}$ at two different values of $(I_2/I_1)'$ and (I_2/I_1) gives

$$\begin{aligned}\frac{\left(\frac{\partial F}{\partial t}\right)_{\perp,\max}}{\left(\frac{\partial F}{\partial t}\right)'_{\perp,\max}} \approx & \frac{(I_2/I_1)'}{(I_2/I_1)} \\ & \times \left(\frac{q_{\perp,\max}^2\sqrt{1+q_{\perp,\max}^2} + \theta(q_{\perp,\max}^2((I_2/I_1)^2 - 3) - 2)}{q_{\perp,\max}^2\sqrt{1+q_{\perp,\max}^2} + \theta(q_{\perp,\max}^2((I_2/I_1)'^2 - 3) - 2)}\right) \\ \approx & \frac{(I_2/I_1)'}{(I_2/I_1)}\frac{q_{\perp,\max}^2\sqrt{1+q_{\perp,\max}^2} + \theta q_{\perp,\max}^2(I_2/I_1)^2}{q_{\perp,\max}^2\sqrt{1+q_{\perp,\max}^2} + \theta q_{\perp,\max}^2(I_2/I_1)'^2}, \end{aligned} \tag{B.9}$$

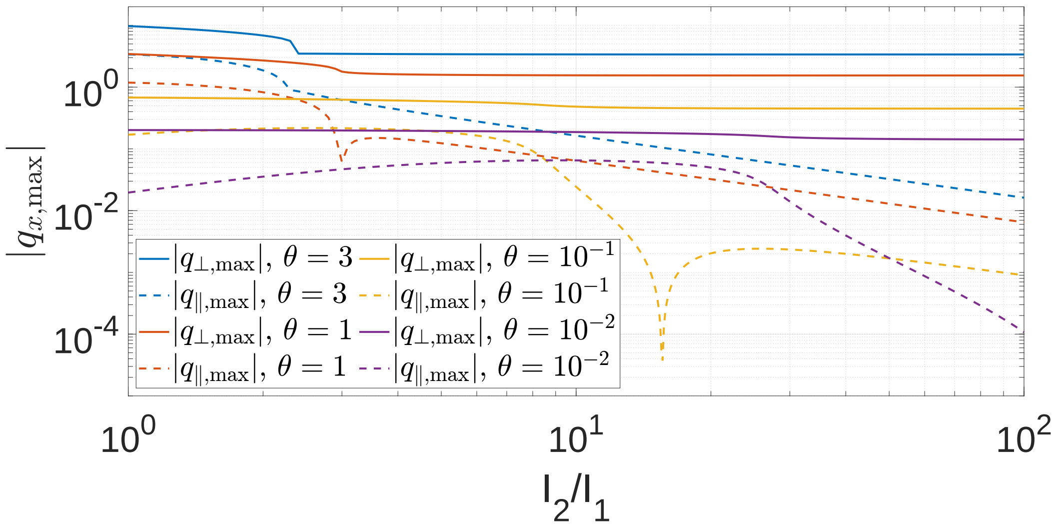

Figure B.3: The values of $|q_{\parallel,\max}|$ and $|q_{\perp,\max}|$ as a function of I_2/I_1 for the combined perpendicular terms $\left(\frac{\partial F}{\partial t}\right)_\perp$. Dashed lines indicate $|q_{\parallel,\max}|$ at different temperatures while solid lines show $|q_{\perp,\max}|$. For large $I_2/I_1 \gg 1$, $|q_{\parallel,\max}| \ll 1$ and $|q_{\perp,\max}|$ is approximately constant. The sharp dips in $|q_{\parallel,\max}|$ are due to a change in sign.

which is valid for $I_2/I_1 \gg 1$. This ratio becomes

$$\frac{\left(\frac{\partial F}{\partial t}\right)_{\perp,\max}}{\left(\frac{\partial F}{\partial t}\right)'_{\perp,\max}} \approx \frac{(I_2/I_1)}{(I_2/I_1)'}, \tag{B.10}$$

when $\theta(I_2/I_1)^2 \gg \sqrt{1+q_{\perp,\max}^2} = \gamma(0, q_{\perp,\max})$. As $|q_{\perp,\max}|$ increases monotonically with temperature from $|q_{\perp,\max}| \sim 0.14$ for $\theta = 10^{-2}$ to $|q_{\perp,\max}| \sim 3.4$ for $\theta = 3$, this condition is satisfied in the $I_2/I_1 \gg 1$ regime, confirming that $\left(\frac{\partial F}{\partial t}\right)_{\perp,\max} \propto I_2/I_1$ for low magnetisations.

Appendix C

Resonance ellipses

Sample resonance ellipses are shown on contour plots of $\partial F/\partial q_\perp$ for $\theta = 1/300$ in Fig. C.1 and $\theta = 0.1$ in Fig. C.2, showing how the regions of negative gradient in the perpendicular direction cannot be avoided at higher temperatures due to their increased width. Although the growth rate calculation does not solely depend on $\partial F/\partial p_\perp$ (as shown in Eq. (2.49)), it is a useful proxy for visualisation purposes.

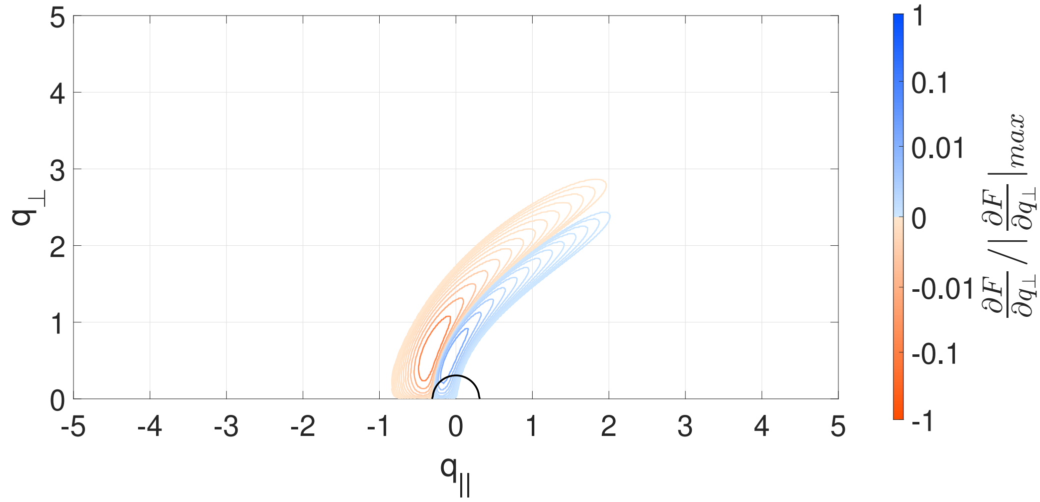

Figure C.1: Contour plot showing $\frac{\partial F}{\partial q_{\perp}}$ for $\eta = 1$ and $\theta = 1/300$. The plot is normalised to $|\frac{\partial F}{\partial q_{\perp}}|_{max}$ for presentation purposes. Positive regions of the derivative are shown in blue, with negative regions in red. The black line shows the resonance ellipse for the slow X-mode with $\omega_r = 0.95\Omega$ and perpendicular propagation. This ellipse produces a positive growth rate at lower temperatures as it crosses more areas of F$\frac{\partial F}{\partial q_{\perp}} > 0$. Note that this is not the only wavenumber that can produce positive growth, and has been chosen for visualisation purposes.

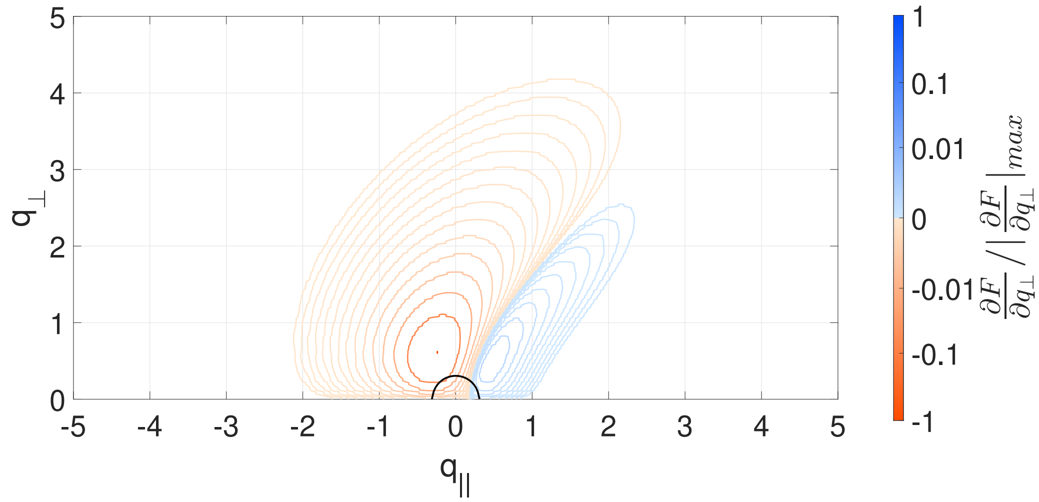

Figure C.2: Contour plot showing $\frac{\partial F}{\partial q_\perp}$ for $\eta = 1$ and $\theta = 0.1$. The plot is normalised to $|\frac{\partial F}{\partial q_\perp}|_{max}$ for presentation purposes. Positive regions of the derivative are shown in blue, with negative regions in red. The black line shows the resonance ellipse for the slow X-mode with $\omega_r = 0.95\Omega$ and perpendicular propagation.FThis ellipse produces a positive growth rate at lower temperatures but overlaps with too much of the $\frac{\partial F}{\partial q_\perp} < 0$ area at higher temperatures such as this one.

Bibliography

Abbott R., et al., 2023a, Physical Review X, 13, 011048

Abbott R., et al., 2023b, The Astrophysical Journal, 955, 155

Alsop D., Arons J., 1988, Physics of Fluids, 31, 839

Amato E., Arons J., 2006, The Astrophysical Journal, 653, 325

Anna-Thomas R., et al., 2023, Science, 380, 599

Asenjo F. A., Muoz V., Valdivia J. A., Hada T., 2009, Physics of Plasmas, 16

Babul A.-N., Sironi L., 2020, Monthly Notices of the Royal Astronomical Society, 499, 2884

Bagchi M., 2017, The Astrophysical Journal Letters, 838, L16

Baldwin D. E., Bernstein I. B., Weenink M. P. H., 1969, Advances in Plasma Physics, 3, 1

Bannister K. W., et al., 2019, Science, 365, 565

Bassa C. G., et al., 2017, The Astrophysical Journal Letters, 843, L8

Baumjohann W., Treumann R. A., 2023, Frontiers in Physics, 11, 1174557

Begelman M. C., Ergun R. E., Rees M. J., 2005, The Astrophysical Journal, 625, 51

Beloborodov A. M., 2017, The Astrophysical Journal Letters, 843, L26

Beloborodov A. M., 2020, The Astrophysical Journal, 896, 142

Beloborodov A. M., 2021, The Astrophysical Journal Letters, 922, L7

Beloborodov A. M., 2023, The Astrophysical Journal, 959, 34

Beloborodov A. M., 2024, The Astrophysical Journal, 975, 223

Beloborodov A. M., 2025, arXiv e-prints, p. arXiv:2503.16054

Beniamini P., Hotokezaka K., van der Horst A., Kouveliotou C., 2019, Monthly Notices of the Royal Astronomical Society, 487, 1426

Beskin V. S., Kuznetsova I. V., Rafikov R. R., 1998, Monthly Notices of the Royal Astronomical Society, 299, 341

Bilbao P. J., Silva L. O., 2023, Physical Review Letters, 130, 165101

Bilbao P. J., Ewart R. J., Assunçao F., Silva T., Silva L. O., 2024, Physics of Plasmas, 31, 052112

Bilbao P., Silva T., Silva L. O., 2025, Science Advances, 11, eadt8912

Bingham R., Cairns R. A., 2000, Physics of Plasmas, 7, 3089

Blaes O., Blandford R., Goldreich P., Madau P., 1989, The Astrophysical Journal, 343, 839

Bochenek C. D., Ravi V., Belov K. V., Hallinan G., Kocz J., Kulkarni S. R., McKenna D. L., 2020, Nature, 587, 59

Bochenek C. D., Ravi V., Dong D., 2021, The Astrophysical Journal Letters, 907, L31

Bret A., Gremillet L., Dieckmann M. E., 2010, Physics of Plasmas, 17, 120501

Bruni G., et al., 2024, Nature, 632, 1014

CHIME/FRB Collaboration et al., 2019, The Astrophysical Journal Letters, 885, L24

CHIME/FRB Collaboration et al., 2020a, Nature, 582, 351

CHIME/FRB Collaboration et al., 2020b, Nature, 587, 54

CHIME/FRB Collaboration et al., 2021, The Astrophysical Journal Supplement, 257, 59

CHIME/FRB Collaboration et al., 2022, Nature, 607, 256

Caleb M., Stappers B. W., Rajwade K., Flynn C., 2019, Monthly Notices of the Royal Astronomical Society, 484, 5500

Cerutti B., Beloborodov A. M., 2017, Space Science Reviews, 207, 111

Champion D. J., et al., 2016, Monthly Notices of the Royal Astronomical Society, 460, L30

Cho H., et al., 2020, The Astrophysical Journal Letters, 891, L38

Connor L., Sievers J., Pen U.-L., 2016, Monthly Notices of the Royal Astronomical Society, 458, L19

Cordes J. M., Lazio T. J. W., 2002, arXiv e-prints, pp astro–ph/0207156

Cordes J. M., Wasserman I., 2016, Monthly Notices of the Royal Astronomical Society, 457, 232

Cordes J. M., Ocker S. K., Chatterjee S., 2022, The Astrophysical Journal, 931, 88

Crawford F., Hisano S., Golden M., Kikunaga T., Laity A., Zoeller D., 2022, Monthly Notices of the Royal Astronomical Society, 515, 3698

Dall'Osso S., Stella L., 2022, in Bhattacharyya S., Papitto A., Bhattacharya D., eds, Astrophysics and Space Science Library Vol. 465, Astrophysics and Space Science Library. pp 245–280 (arXiv:2103.10878), doi:10.1007/978-3-030-85198-9_8

Day C. K., et al., 2020, Monthly Notices of the Royal Astronomical Society, 497, 3335

Deng C.-M., Cai Y., Wu X.-F., Liang E.-W., 2018, Physical Review D, 98, 123016

Drummond W. E., Rosenbluth M. N., 1962, The Physics of Fluids, 5, 1507

Ergun R. E., Carlson C. W., McFadden J. P., Delory G. T., Strangeway R. J., Pritchett P. L., 2000, The Astrophysical Journal, 538, 456

Falcke H., Rezzolla L., 2014, Astronomy & Astrophysics, 562, A137

Fedorova V. A., Rodin A. E., 2019, Astronomy Reports, 63, 39

Fleishman G. D., Mel'nikov V. F., 1998, Physics Uspekhi, 41, 1157

Fong W.-f., et al., 2021, The Astrophysical Journal Letters, 919, L23

Freund H. P., Wu C. S., 1976, Physics of Fluids, 19, 299

Gajjar V., et al., 2018, The Astrophysical Journal, 863, 2

Gallant Y. A., Hoshino M., Langdon A. B., Arons J., Max C. E., 1992, The Astrophysical Journal, 391, 73

Gary S. P., 1993, Theory of Space Plasma Microinstabilities. Cambridge University Press

Gary S. P., Skoug R. M., Steinberg J. T., Smith C. W., 2001, Geophysical Research Letters, 28, 2759

Ge M. Y., et al., 2023, The Astrophysical Journal, 953, 67

Geng J. J., Huang Y. F., 2015, The Astrophysical Journal, 809, 24

Gill R., Heyl J., 2007, Monthly Notices of the Royal Astronomical Society, 381, 52

Golbraikh E., Lyubarsky Y., 2023, The Astrophysical Journal, 957, 102

Goldreich P., Julian W. H., 1969, The Astrophysical Journal, 157, 869

Gourgouliatos K. N., Lynden-Bell D., 2019, Monthly Notices of the Royal Astronomical Society, 482, 1942

Gu W.-M., Dong Y.-Z., Liu T., Ma R., Wang J., 2016, The Astrophysical Journal Letters, 823, L28

Gu W.-M., Yi T., Liu T., 2020, Monthly Notices of the Royal Astronomical Society, 497, 1543

Hashimoto T., et al., 2022, Monthly Notices of the Royal Astronomical Society, 511, 1961

Hessels J. W. T., et al., 2019, The Astrophysical Journal Letters, 876, L23

Hewitt R. G., Melrose D. B., Ronnmark K. G., 1982, Australian Journal of Physics, 35, 447

Hiramatsu D., et al., 2023, The Astrophysical Journal Letters, 947, L28

Hirshfield J. L., 1963, Nature, 198, 20

Hu C.-R., Huang Y.-F., 2023, The Astrophysical Journal Supplement, 269, 17

Ioka K., Zhang B., 2020, The Astrophysical Journal Letters, 893, L26

Israel G. L., et al., 2016, Monthly Notices of the Royal Astronomical Society, 457, 3448

Iwamoto N., 1993, Physical Review E, 47, 604

Iwamoto M., Amano T., Hoshino M., Matsumoto Y., 2017, The Astrophysical Journal, 840, 52

Iwamoto M., Matsumoto Y., Amano T., Matsukiyo S., Hoshino M., 2024, Physical Review Letters, 132, 035201

Iwazaki A., 2015, Physical Review D, 91, 023008

James C. W., Prochaska J. X., Macquart J. P., North-Hickey F. O., Bannister K. W., Dunning A., 2022, Monthly Notices of the Royal Astronomical Society, 509, 4775

Kashiyama K., Ioka K., Mészáros P., 2013, The Astrophysical Journal Letters, 776, L39

Kaspi V. M., Beloborodov A. M., 2017, Annual Review of Astronomy and Astrophysics, 55, 261

Katz J. I., 2016a, Modern Physics Letters A, 31, 1630013

Katz J. I., 2016b, The Astrophysical Journal, 826, 226

Katz J. I., 2017, Monthly Notices of the Royal Astronomical Society, 471, L92

Kellermann K. I., Pauliny-Toth I. I. K., 1969, The Astrophysical Journal Letters, 155, L71

Khomenko E., Cally P. S., 2012, The Astrophysical Journal, 746, 68

Kirsten F., et al., 2022, Nature, 602, 585

Kirsten F., et al., 2024, Nature Astronomy, 8, 337

Kumar P., Lu W., Bhattacharya M., 2017, Monthly Notices of the Royal Astronomical Society, 468, 2726

Kumar P., et al., 2021, Monthly Notices of the Royal Astronomical Society, 500, 2525

Kumar P., Shannon R. M., Lower M. E., Bhandari S., Deller A. T., Flynn C., Keane E. F., 2022, Monthly Notices of the Royal Astronomical Society, 512, 3400

Lanman A. E., et al., 2022, The Astrophysical Journal, 927, 59

Li L.-B., Huang Y.-F., Geng J.-J., Li B., 2018, Research in Astronomy and Astrophysics, 18, 061

Li C. K., et al., 2021a, Nature Astronomy, 5, 378

Li D., et al., 2021b, Nature, 598, 267

Lin L., et al., 2020, Nature, 587, 63

Liu T., Romero G. E., Liu M.-L., Li A., 2016, The Astrophysical Journal, 826, 82

Long K., Pe'er A., 2018, The Astrophysical Journal Letters, 864, L12

Long K., Pe'er A., 2023, Physical Review D, 107, L121301

Long K., Pe'er A., 2025a, Monthly Notices of the Royal Astronomical Society, 538, 1029

Long K., Pe'er A., 2025b, Monthly Notices of the Royal Astronomical Society, 544, 2160

Lorimer D. R., Bailes M., McLaughlin M. A., Narkevic D. J., Crawford F., 2007, Science, 318, 777

Lu W., Kumar P., 2018, Monthly Notices of the Royal Astronomical Society, 477, 2470

Luan J., Goldreich P., 2014, The Astrophysical Journal Letters, 785, L26

Luo R., Men Y., Lee K., Wang W., Lorimer D. R., Zhang B., 2020a, Monthly Notices of the Royal Astronomical Society, 494, 665

Luo R., et al., 2020b, Nature, 586, 693

Lyubarsky Y., 2014, Monthly Notices of the Royal Astronomical Society, 442

Lyubarsky Y., 2020, The Astrophysical Journal, 897

Lyubarsky Y., 2021, Universe, 7

Lyubarsky Y., Kirk J. G., 2001, The Astrophysical Journal, 547, 437

Lyutikov M., 2021, The Astrophysical Journal, 922, 166

Lyutikov M., 2024, Monthly Notices of the Royal Astronomical Society, 529, 2180

Macquart J. P., Shannon R. M., Bannister K. W., James C. W., Ekers R. D., Bunton J. D., 2019, The Astrophysical Journal Letters, 872, L19

Macquart J. P., et al., 2020, Nature, 581, 391

Mannings A. G., et al., 2021, The Astrophysical Journal, 917, 75

Marcote B., et al., 2020, Nature, 577, 190

Margalit B., Metzger B. D., 2018, The Astrophysical Journal Letters, 868, L4

Margalit B., Metzger B. D., Sironi L., 2020, Monthly Notices of the Royal Astronomical Society, 494, 4627

Masui K., et al., 2015, Nature, 528, 523

Mckinven R., et al., 2025, Nature, 637, 43

Melrose D. B., 1976, The Astrophysical Journal, 207, 651

Melrose D. B., 2017, Reviews of Modern Plasma Physics, 1, 5

Mereghetti S., 2008, Astronomy and Astrophysics Review, 15, 225

Mereghetti S., et al., 2020, The Astrophysical Journal Letters, 898, L29

Metzger B. D., Berger E., Margalit B., 2017, The Astrophysical Journal, 841, 14

Metzger B. D., Margalit B., Sironi L., 2019, Monthly Notices of the Royal Astronomical Society, 485, 4091

Michel F. C., 1969, The Astrophysical Journal, 158, 727

Michilli D., et al., 2018, Nature, 553, 182

Montgomery D. C., Tidman D. A., 1964, Plasma kinetic theory. McGraw-Hill, New York

Most E. R., Nathanail A., Rezzolla L., 2018, The Astrophysical Journal, 864, 117

Mottez F., Zarka P., 2014, Astronomy & Astrophysics, 569, A86

Muñoz V., Asenjo F. A., Domínguez M., López R. A., Valdivia J. A., Viñas A., Hada T., 2014, Nonlinear Processes in Geophysics, 21

Nariyuki Y., Hada T., Tsubouchi K., 2010, Physics of Plasmas, 17, 072301

Nättilä J., Beloborodov A. M., 2022, Physical Review Letters, 128, 075101

Nimmo K., et al., 2021, Nature Astronomy, 5, 594

Nimmo K., et al., 2022, Nature Astronomy, 6, 393

Nimmo K., et al., 2025, Nature, 637, 48

Niu C. H., et al., 2022, Nature, 606, 873

Niu J. R., et al., 2024, The Astrophysical Journal Letters, 972, L20

Oguri M., 2019, Reports on Progress in Physics, 82, 126901

Olausen S. A., Kaspi V. M., 2014, The Astrophysical Journal Supplement, 212, 6

Ouyed R., Leahy D., Koning N., 2020, Research in Astronomy and Astrophysics, 20, 027

Pastor-Marazuela I., et al., 2021, Nature, 596, 505

Petroff E., et al., 2017, Monthly Notices of the Royal Astronomical Society, 469, 4465

Petroff E., Hessels J. W. T., Lorimer D. R., 2022, Astronomy and Astrophysics Reviews, 30, 2

Platts E., Weltman A., Walters A., Tendulkar S. P., Gordin J. E. B., Kandhai S., 2019, Physics Reports, 821, 1

Pleunis Z., et al., 2021a, The Astrophysical Journal Letters, 911, L3

Pleunis Z., et al., 2021b, The Astrophysical Journal, 923, 1

Plotnikov I., Sironi L., 2019, Monthly Notices of the Royal Astronomical Society, 485

Press W. H., Teukolsky S. A., Vettering W. T., Flannery B. P., 2007, NUMERICAL RECIPES The Art of Scientific Computing Third Edition. Cambridge University Press, doi:10.1017/CBO9781107415324.004

Pritchett P. L., Strangeway R. J., 1985, Journal of Geophysical Research, 90, 9650

Qu Y., Zhang B., 2023, Monthly Notices of the Royal Astronomical Society, 522, 2448

Qu Y., Kumar P., Zhang B., 2022, Monthly Notices of the Royal Astronomical Society, 515, 2020

Rajwade K. M., et al., 2020, Monthly Notices of the Royal Astronomical Society, 495, 3551

Ravi V., et al., 2019, Nature, 572, 352

Ridnaia A., et al., 2021, Nature Astronomy, 5, 372

Rybicki G. B., Lightman A. P., 1979, Radiative processes in astrophysics. Wiley, New York

Ryder S. D., et al., 2023, Science, 382, 294

Sagiv A., Waxman E., 2002, The Astrophysical Journal, 574, 861

Scholz P., et al., 2017, The Astrophysical Journal, 846, 80

Sharma P., Barkov M. V., Lyutikov M., 2023, Monthly Notices of the Royal Astronomical Society, 524, 6024

Shin K., et al., 2023, The Astrophysical Journal, 944, 105

Sironi L., Spitkovsky A., 2011, The Astrophysical Journal, 726, 75

Sironi L., Plotnikov I., Nättilä J., Beloborodov A. M., 2021, Physical Review Letters, 127, 035101

Sobacchi E., Lyubarsky Y., Beloborodov A. M., Sironi L., 2022, Monthly Notices of the Royal Astronomical Society, 511, 4766

Sobacchi E., Iwamoto M., Sironi L., Piran T., 2024a, Physical Review Research, 6, 043213

Sobacchi E., Iwamoto M., Sironi L., Piran T., 2024b, Astronomy & Astrophysics, 690, A332

Sridhar N., Zrake J., Metzger B. D., Sironi L., Giannios D., 2021, Monthly Notices of the Royal Astronomical Society, 501, 3184

Stewart G. A., Laing E. W., 1992, Journal of Plasma Physics, 47, 295

Stix T. H., 1992, Waves in plasmas. Springer Science & Business Media, New York

Tavani M., et al., 2021, Nature Astronomy, 5, 401

Tendulkar S. P., et al., 2017, The Astrophysical Journal Letters, 834, L7

Tendulkar S. P., et al., 2021, The Astrophysical Journal Letters, 908, L12

Thompson C., Duncan R. C., 1996, The Astrophysical Journal, 473, 322

Thornton D., et al., 2013, Science, 341, 53

Tong Z.-J., Wang C.-B., Zhang P.-J., Liu J., 2017, Physics of Plasmas, 24, 052902

Totani T., 2013, Publications of the Astronomical Society of Japan, 65, L12

Treumann R. A., 2006, Astronomy and Astrophysics Reviews, 13, 229

Twiss R. Q., 1958, Australian Journal of Physics, 11, 564

Vedenov A., Velikhov E., Sagdeev R., 1961, Nuclear Fusion, 1, 82

Verscharen D., Klein K. G., Maruca B. A., 2019, Living Reviews in Solar Physics, 16, 5

Wada T., Ioka K., Zhang B., 2021, The Astrophysical Journal, 920, 54

Wadiasingh Z., Timokhin A., 2019, The Astrophysical Journal, 879, 4

Wang C. B., Wu C. S., 2009, Physics of Plasmas, 16, 020703

Wang C. B., Wu C. S., Yoon P. H., 2006, Physical Review Letters, 96, 125001

Wang J.-S., Yang Y.-P., Wu X.-F., Dai Z.-G., Wang F.-Y., 2016, The Astrophysical Journal Letters, 822, L7

Waxman E., 2017, The Astrophysical Journal, 842, 34

Winglee R. M., Dulk G. A., 1986, The Astrophysical Journal, 310, 432

Wu C. S., 1985, Space Science Reviews, 41, 215

Wu D. J., 2014, Physics of Plasmas, 21, 064506

Wu C. S., Lee L. C., 1979, The Astrophysical Journal, 230, 621

Wu C. S., Yoon P. H., 2007, Physical Review Letters, 99, 075001

Wu C. S., Wang C. B., Wu D. J., Lee K. H., 2012, Physics of Plasmas, 19, 082902

Wu C. S., Yoon P. H., Wang C. B., 2014a, Physics of Plasmas, 21, 104507

Wu D. J., Chen L., Zhao G. Q., Tang J. F., 2014b, Astronomy & Astrophysics, 566

Wu Q., Zhang G. Q., Wang F. Y., Dai Z. G., 2020, The Astrophysical Journal Letters, 900, L26

Xu H., et al., 2022, Nature, 609, 685

Xu J., et al., 2023, Universe, 9, 330

Yang Y.-P., Zhang B., 2018, The Astrophysical Journal, 868, 31

Yao J. M., Manchester R. N., Wang N., 2017, The Astrophysical Journal, 835, 29

Yoon P. H., Wang C. B., Wu C. S., 2009, Physics of Plasmas, 16

Yu Y.-W., Zou Y.-C., Dai Z.-G., Yu W.-F., 2021, Monthly Notices of the Royal Astronomical Society, 500, 2704

Yuan Y., Beloborodov A. M., Chen A. Y., Levin Y., 2020, The Astrophysical Journal Letters, 900, L21

Zhang B., 2014, The Astrophysical Journal Letters, 780, L21

Zhang B., 2016, The Astrophysical Journal Letters, 827, L31

Zhang B., 2017, The Astrophysical Journal Letters, 836, L32

Zhang B., 2019, The Astrophysical Journal Letters, 873, L9

Zhang B., 2020a, Nature, 587

Zhang B., 2020b, The Astrophysical Journal Letters, 890, L24

Zhang B., 2022, The Astrophysical Journal, 925, 53

Zhang B., 2023, Reviews of Modern Physics, 95, 035005

Zhang B., 2024, Annual Review of Nuclear and Particle Science, 74, 89

Zhao G. Q., Wu C. S., 2013, Physics of Plasmas, 20, 034503

Zhao G. Q., Chen L., Yan Y. H., Wu D. J., 2013, The Astrophysical Journal, 770, 75

Zhou D. J., et al., 2022, Research in Astronomy and Astrophysics, 22, 124001